

New Integrated Waveguides Concept and Development of Substrate Integrated Antennas with Controlled Boundary Conditions

Nima Bayat-Makou

A Thesis
In the Department
of
Electrical and Computer Engineering

Presented in Partial Fulfillment of the Requirements
For the Degree of
Doctor of Philosophy (Electrical and Computer Engineering) at
Concordia University
Montreal, Québec, Canada

July 2017

© Nima Bayat-Makou, 2017

**CONCORDIA UNIVERSITY
SCHOOL OF GRADUATE STUDIES**

This is to certify that the thesis prepared

By: Nima Bayat-Makou

Entitled: New Integrated Waveguides Concept and Development of Substrate

Integrated Antennas with Controlled Boundary Conditions

and submitted in partial fulfillment of the requirements for the degree of

Doctor Of Philosophy (Electrical and Computer Engineering)

complies with the regulations of the University and meets the accepted standards with respect to originality and quality.

Signed by the final examining committee:

<u>Dr. Nizar Bouguila</u>	Chair
<u>Dr. Jean-Jacques Laurin</u>	External Examiner
<u>Dr. Amr Youssef</u>	External to Program
<u>Dr. Robert Paknys</u>	Examiner
<u>Dr. Abdel R. Sebak</u>	Examiner
<u>Dr. Ahmed A. Kishk</u>	Thesis Supervisor

Approved by

Dr. Wei-Ping Zhu, Graduate Program Director

September 7, 2017

Date of Defense

Dr. Amir Asif, Dean of Faculty of Engineering and Computer Science

Abstract

New Integrated Waveguides Concept and Development of Substrate Integrated Antennas with Controlled Boundary Conditions

Nima Bayat-Makou, Ph.D.

Concordia University, 2017

The unprecedented development of substrate integrated circuits (SICs) has made a widespread necessity for further studies and development of waveguides and antennas based on this technology. As the operating frequency is on the rise, the conventional designs of the substrate integrated components are becoming more problematic and costly. Therefore, some techniques are proposed to improve the performance of the waveguides and antennas based on the concept of substrate integrated technology.

First, the problems of the recently developed ridge gap waveguide (RGW) are resolved by introducing a new configuration of this technology which has considerable advantages over the original version of the RGW regarding its construction technology, propagation mode, characteristic impedance, and insertion loss. A basic design and modified designs of the proposed waveguide are introduced and implemented and their performances are verified experimentally.

Second, the contactless air-filled configuration of substrate integrated waveguide (SIW), which has been widely accepted for the planar and integrated microwave circuits, is also introduced. The proposed configuration enables the SIW to support propagation in the air medium with the regular connection of the covering layers at millimeter-wave frequencies without worry about leaking power from the possible loose electrical contact between the layers.

The substrate integrated antennas have a strong potential to be used in the compact wireless devices as they can be easily integrated with the baseband circuits. In the horn family, the H -plane horn antenna that can be implemented in the integrated form has received considerable attention in recent years. However, numerous problems are associated with this antenna such as limited bandwidth, tapered aperture distribution, high back radiation, and E -plane asymmetry. Several

new techniques including open parallel aperture transitions, hard boundary conditions inside and soft conditions outside, multi-layer structure with RGW configuration, and contactless multi-layer configuration are introduced to improve the performance of this antenna.

Dedication

This thesis is proudly dedicated to....

All my beloved family

To my mother the first person in my life

To my father without him I'm nothing

And to my brother

Pourya

Thank for your endless love, sacrifices,

prayers, and supports

Acknowledgment

I would like to express my sincere gratitude to my supervisor Prof. Ahmed A. Kishk for his constant support, guidance, and motivation. It would never have been possible for me to take this work to completion without his support and encouragement and it was my honor to work with such an exceptional scholar.

Furthermore, I would like to thank the committee members, Prof. Jean-Jacques Laurin, Prof. Robert Paknys, Prof. Abdel A. Sebak and Prof. Amr Youssef for their review of my thesis and their constructive comments and feedback.

Table of Contents

List of Figures	X
List of Symbols	XVII
List of Acronyms	XVIII
1. Introduction	1
1.1 Ridge Gap Waveguide.....	2
1.2 Challenges and Problems with Ridge Gap Waveguide	4
1.3 Air-Filled Substrate Integrated Waveguide	6
1.3.1 Problems Associated with the Air-Filled Integrated Waveguides	7
1.4 Substrate Integrated Horn Antenna	9
1.4.1 Problems Associated with Substrate Integrated Horn Antennas.....	12
1.5 Dissertation Outline and Contributions	14
2. TEM Printed Ridge Gap Waveguide	15
2.1 Proposed Configuration.....	15
2.2 Characteristic Impedance Extraction of TEM- and Quasi-TEM-PRGW	22
2.3 Modified Configuration of TEM-PRGW	27
2.4 Transition to Microstrip Line	32
2.5 Fabricated Prototypes	33
2.6 Conclusion	40
3. Contactless Air-Filled Substrate Integrated Waveguide	44
3.1 Proposed Configuration of Air-Filled SIW	44
3.2 Gap Estimation Between Overlapping Substrate Layers	46
3.3 Unit Cell and Waveguide Configuration of Proposed Air-Filled SIW	47

3.4	Comparison with the Corresponding Air-Filled SIW.....	52
3.5	Transition to Standard Feeding Line	55
3.6	Experimental Evaluation	58
3.7	Conclusion.....	63
4.	Partially Air-Filled Conductor-Backed Coplanar Waveguide	64
4.1	Air-Filled CBCPW Configuration.....	64
4.2	Quasi-Static Analysis of Air-Filled CBCPW Based on Conformal Mapping.....	66
4.3	Contactless Air-Filled SIW Fed by Partially Air-Filled CBCPW	69
4.4	Conclusion	72
5.	Substrate Integrated Horn Antennas with Improved Performance	73
5.1	Substrate Integrated <i>H</i> -plane Horn Antenna Loaded with Open Parallel Transitions	73
5.1.1	Motivation.....	73
5.1.2	Substrate Integrated Horn with Open Parallel Transitions.....	73
5.1.3	Simulation and Fabrication Results	76
5.2	Substrate Integrated Horn Antennas with Uniform Aperture Distribution	79
5.2.1	Soft and Hard Horns and Surfaces	79
5.2.2	Planar Strip-Via Array Soft Surface Design	80
5.2.3	Hard Conditions in the Integrated Horn.....	82
5.2.4	Air-Filled Substrate Integrated Horn with Uniform Phase and Amplitude Distribution of Aperture	86
5.2.5	Simulation and Measurement Results of the Proposed Hard Horn.....	90
5.3	Millimeter-Wave Substrate Integrated Dual Level Gap Waveguide Horn Antenna..	94
5.3.1	Motivation.....	94
5.3.2	E-SIGW Design.....	95

5.3.3	Horn Design	99
5.3.4	Antenna Results and Modifications	103
5.3.5	Millimeter-Wave Contactless Multi-Layer Air-Filled <i>H</i> -plane SIW Horn.....	111
5.4	Conclusion	116
6.	Conclusion and Future Works	119
6.1	Conclusions	119
6.2	Future works	120
REFERENCES	122

List of Figures

Fig. 1-1. Configuration of ideal ridge gap waveguide.....	3
Fig. 2-1. (a) Geometry of a single texture side (conventional) RGW (b) Proposed TEM-RGW with symmetric double texture sides.....	15
Fig. 2-2. (a) Double pin (double texture) and (b) Proposed mushroom unit cell (double texture) of TEM-RGW configuration ($W_{cell}=1.5$, $h_1= 0.508$, $gap= 0.254$, $W_{pl}=1.3$ mm).....	16
Fig. 2-3. Dispersion diagram of the AMC-AMC periodic structure with double mushroom unit cell of Fig. 2-2(b).....	17
Fig. 2-4. Electric field distribution of the different modes of double mushroom unit cell.....	18
Fig. 2-5. (a) Isometric view of the double texture TEM-PRGW, (b) Side view showing the wave port excitation definition ($P=W_{cell}$).....	19
Fig. 2-6. Dispersion diagram of the TEM-PRGW with three rows of unit cells around the guiding ridges.....	19
Fig. 2-7. Reflection and transmission coefficient of the TEM-PRGW.....	20
Fig. 2-8. Transmission coefficient comparison between the proposed double texture TEM-PRGW and single texture conventional PRGW with gap of $d=0.254$ mm with two wavelength long. ...	20
Fig. 2-9. Comparison between the normalized electric field distribution along the transverse cross section of a TEM-PRGW and Quasi-TEM-PRGW at 37 GHz with gap of $d = 0.254$ mm.....	21
Fig. 2-10. Characteristic impedance of parallel plate waveguide (Eq. (2-1)), proposed TEM-PRGW (full wave simulation and Eq. (2-7)), and regular PRGW with a gap of $d = 0.254$ mm. .	22
Fig. 2-11. Comparison between full wave simulated characteristic impedance (solid line) and those obtained from (2-6) (dashed line) of the TEM-PRGW for different widths.	23
Fig. 2-12. Characteristic impedance of the TEM-PRGW vs. ratio of width to gap height obtained from full wave simulation and (2-7).....	24
Fig. 2-13. Characteristic impedance of quasi-TEM-PRGW and the TEM-PRGW equivalent compared with those obtained in [17].....	25
Fig. 2-14. Characteristic impedance variation of the quasi-TEM-PRGW with W/d	26
Fig. 2-15. Modified unit cell with shifted upper layer by a half cell size in both directions ($W_{pl}=1.3$, $d_1=0.3$, $h_1=0.508$, $h_2=0.508$, $gap=0.254$, $W_{cell}=1.5$ mm).....	28

Fig. 2-16. Dispersion diagram of the modified unit cell in Fig. 2-15.	28
Fig. 2-17. Modified configuration of the proposed TEM-RGW.	29
Fig. 2-18. The modified unit cells for TEM-PRGW with equal thicknesses, $W_{p1}=1.3$, $d_1=0.3$, $h_1=0.508$, $h_2=0.508$, $gap=0.254$, $W_{cell}=1.5$ (a) $W_{p2}=0.8$, $d_2=0.2$ (b) $W_{p2}=1.3$, $d_2=0.79$ (all in mm).	30
Fig. 2-19. Dispersion diagram of the periodic structure made by modified cells of Fig. 2-18....	30
Fig. 2-20. The modified unit cells for the asymmetric TEM-PRGW with different thicknesses, $W_{p1}=1.3$, $d_1=0.3$, $h_1=0.508$, $h_2=0.254$, $gap=0.254$, $W_{cell}=1.5$ (a) $W_{p2}=0.7$, $d_2=0.19$ (b) $W_{p2}=1.3$, $d_2=0.79$ (all in mm).	31
Fig. 2-21. Dispersion diagram of the periodic structure made by modified cells of Fig. 2-20....	31
Fig. 2-22. Dispersion analysis of the one row of the TEM-PRGW with modified unit cells of Fig. 2-20.	32
Fig. 2-23. Separated layers of the transition from microstrip to the TEM-PRGW with $W_{mic}=0.87$, $W_2=1$, $W_3=1.75$, $h_1=0.508$, $h_2=0.254$, and $h_{mic}=0.254$	33
Fig. 2-24. Geometry of the TEM-PRGW with modified unit cell of Fig. 2-20(a), (a) Lower thin AMC layer with straight ridge, (b) Middle microstrip feeding layer, (c) Upper thick AMC layer with straight ridge, (d) 3D view of the stacked layers.	34
Fig. 2-25. Fabricated layers of the TEM-PRGW with modified cells of Fig. 2-20(a).	35
Fig. 2-26. TRL calibration kit for TEM-PRGW with modified cells of Fig. 2-20(a).	35
Fig. 2-27. Simulated and measured reflection and transmission coefficient of the TEM-PRGW with modified unit cell of Fig. 2-20(a) with four wavelengths long.	36
Fig. 2-28. Geometry and fabricated prototype of TEM-PRGW bend line with modified cells of Fig. 2-20(a), (a) Lower thin AMC layer with bend ridge, (b) Middle microstrip feeding layer, (c) Upper thick AMC layer with bend ridge, (d) Fabricated AMC layers with bend ridge, (e) Fabricated bend guide layers with feeding microstrip layers in between (f) 3D view of the stacked layers (g) Assembled layers connected to test fixture probes.	37
Fig. 2-29. Electric field distribution inside the TEM-PRGW bend line at different frequencies.	38
Fig. 2-30. Simulated and measured reflection and transmission coefficients of the TEM-PRGW bend line with modified unit cell of Fig. 2-20(a) with four wavelengths length.	38

Fig. 2-31. Geometry and fabricated prototype of the TEM-PRGW with modified unit cell of Fig. 2-20(b), (a) Lower thin AMC layer with straight ridge, (b) Middle microstrip feeding layer, (c) Upper thick AMC layer with straight ridge, (d) 3D view of the stacked layers (e) Fabricated AMC layers (f) With feeding layer (g) TLR calibration Kit.....	39
Fig. 2-32. Simulated and measured reflection and transmission coefficient of the TEM-PRGW with modified unit cell of Fig. 2-20(b).	40
Fig. 2-33. Geometry and fabricated prototype of TEM-PRGW bend line with modified cells of Fig. 2-20(b), (a) Lower thin AMC layer with bend ridge, (b) Middle microstrip feeding layer, (c) Upper thick AMC layer with bend ridge, (d) Fabricated AMC layers with bend ridge, (e) fabricated bend guide layers with feeding microstrip layers in between (f) 3D view of the stacked layers (g) Assembled layers connected to test fixture probes.	41
Fig. 2-34. Simulated and measured reflection and transmission coefficient of the bend line of TEM-PRGW with modified unit cell of Fig. 2-20(b) with length of four wavelength.	42
Fig. 3-1. The geometry of (a) Conventional air-filled substrate integrated waveguide (b) Contactless air-filled substrate integrated waveguide.....	44
Fig. 3-2. Measuring the thickness of stacked layers with regular plastic screws to identify possible gap height between them.	46
Fig. 3-3. Proposed unit cell for contactless air-filled SIW ($W_p=1.3$, $d=0.8$, $W_c=1.4$, $h_l=0.508$ mm).....	47
Fig. 3-4. Dispersion diagram of the periodic structure made by proposed cells with different gap size on the both sides.	48
Fig. 3-5. Air-filled SIW configuration with the proposed cells ($gap1=gap2$).....	49
Fig. 3-6. Electric field distribution inside the substrate and in the gap regions of the air-filled integrated waveguide (a) Small via diameter, (b) Via diameter meeting conditions in (3-1).	50
Fig. 3-7. (a) Conventional air-filled SIW, (b) Proposed contactless air-filled SIW, covered by PEC lids with the same gap heights.	52
Fig. 3-8. Simulated transmission coefficient comparison between the conventional and contactless air-filled SIW.	53

Fig. 3-9. Electric field distribution inside the substrate and the air-gap of (a) Proposed contactless air-filled SIW with textured surface off the guiding medium (b) Simple air-filled SIW with solid conductor off the guiding medium.....	53
Fig. 3-10. Geometry of air-filled SIW T-junctions (a) Conventional (b) Contactless.....	54
Fig. 3-11. Electric field distribution of air-filled SIW T-junctions (a) Conventional (b) Contactless.	54
Fig. 3-12. Simulated transmission coefficient comparison of the conventional and contactless air-filled SIW T-junctions.	55
Fig. 3-13. Transition segments from CBCPW to contactless air-filled SIW.....	56
Fig. 3-14. The whole configuration of contactless air-filled SIW with transitions.	57
Fig. 3-15. (a) Simple and contact less air-filled integrated waveguides with covering lids (b) Stacked layers fastened with plastic screws (c) TRL calibration kit and moved reference plane location of the air-filled waveguides (d) Exciting the air-filled SIWs with test fixture.	59
Fig. 3-16. Measured transmission coefficient comparison between contactless and simple air-filled SIW.	60
Fig. 3-17. Contactless air-filled SIW with the second TRL calibration kit.	61
Fig. 3-18. Measured transmission coefficient of contactless air-filled SIW with different reference planes moved by TRL kits.	62
Fig. 4-1. The geometry of air-filled CBCPW (a) Simulated model (b) Model used for quasi-static analysis.....	65
Fig. 4-2. Group delay response comparison of air-filled CBCPW with other hree lines.	66
Fig. 4-3. Characteristic impedance for partially air-filled CBCPW ($\epsilon_r = 2.94$).....	69
Fig. 4-4. Modified unit cell of the contactless air-filled SIW to be fed with air-filled CBCPW ($W_p=1.3$, $d_l=0.8$, $h_l=0.508$, $gap1=0.127$, $gap2=0.015$ all mm).	70
Fig. 4-5. Dispersion diagram of the modified cell of contactless air-filled SIW.....	70
Fig. 4-6. Geometry of the contactless air-filled SIW fed by air-filled CBCPW (b) Electric field distribution inside the covering layer (c) Electric field distribution inside the main layer.....	71
Fig. 4-7. Simulated S -parameter response of contactless air-filled SIW fed by air-filled CBCPW.	71

Fig. 5-1. (a) Basic geometry and parameters of H -plane horn (b) Geometry of simple substrate integrated H -plane horn antenna (c) Electric field distribution inside designed simple substrate integrated H -plane horn antenna.	74
Fig. 5-2. Field distribution inside the substrate of simple integrated H -plane horn (a) Without outer vias (b) With outer vias.	75
Fig. 5-3. The geometry of the substrate integrated H -plane horn antenna loaded parallel transitions by long transverse slots, and design dimensions.	75
Fig. 5-4. Simulated reflection coefficients for the horn with the transition (single or double) and without the transition.	76
Fig. 5-5. The fabricated prototypes of substrate integrated horn with parallel transitions.	77
Fig. 5-6. Measured return loss response of the fabricated H -plane horn with parallel transitions.	77
Fig. 5-7. Radiation patterns of the H -plane horn without and with the transitions, blue dashed lines, simulated without transitions; red solid lines, simulated with transitions; and black thin lines, measured with transitions. Upper patterns at 25 GHz for the 4.7 mm transitions and the lower patterns at 27 GHz for 4.2 mm transitions.	78
Fig. 5-8. Geometry of the strip-via soft surface.	81
Fig. 5-9. Transmission coefficient of soft surface with different excitations.	82
Fig. 5-10. Geometry and electric field distribution (at 25 GHz) of the substrate integrate horn antennas with realized hard boundary conditions by (a) Single step perforation (b) Five-step perforation (c) Substrate cut.	84
Fig. 5-11. Directivity comparison between simple integrated horn and perforated and air-filled hard horns.	86
Fig. 5-12. Geometry of the air-filled H -plane hard horn antenna, (a) Middle substrate (b) Top and bottom substrates (c) CBCPW to SIW transition (d) Table of dimensions (unit: mm) (e) 3D view of the stacked layers.	87
Fig. 5-13. The fabricated prototype with soft surface on the top and bottom and hard walls at the aperture.	89
Fig. 5-14. Frequency responses of the return and insertion losses for the CBCPW to SIW transition.	90

Fig. 5-15. Electric field distribution inside the air-filled hard horn at 25 GHz (a) Amplitude (b) Phase.	91
Fig. 5-16. Simulated and measured reflection coefficient of the air-filled substrate integrated hard horn.	91
Fig. 5-17. Simulated and measured radiation patterns of the air-filled substrate integrated hard horn (solid lines, simulation; dashed black lines, simulation without soft surfaces; dashed blue lines, measurement).	92
Fig. 5-18. Simulated radiation efficiency and measured gain of the proposed hard horn.	93
Fig. 5-19. (a) Substrate integrated gap waveguide (SIGW) (b) Elevated substrate integrated gap waveguide (E-SIGW) (c) E-SIGW unit cell.	96
Fig. 5-20. Dispersion diagram of a single unit cell at E-SIGW structure.	96
Fig. 5-21. Dispersion diagram of the E-SIGW line.	97
Fig. 5-22. Variation of the characteristic impedance of the E-SIGW line with the width of printed ridge.	98
Fig. 5-23. Back-to-back transition from microstrip line to E-SIGW line.	98
Fig. 5-24. Reflection and transmission coefficient responses of the back-to-back transition from microstrip line to E-SIGW line.	99
Fig. 5-25. (a) Single level horn (b) Double level horn (c) Double level horn with transition (d) geometry and design parameters of proposed double level horn (e) Magnified transition between the layers (f) 3D View of the stacked layers of the horn with the end launch connector.	100
Fig. 5-26. (a) Table of the antenna parameters (unit: mm) (b) The fabricated prototype fed by the end-launch connector.	102
Fig. 5-27. Simulated and measured reflection coefficient responses of the E-SIGW horns.	104
Fig. 5-28. Electric field distribution inside the horn at 60 GHz, (a) At upper thin layer (middle of h_1), (b) At lower layer (middle of h_2).	105
Fig. 5-29. Radiation pattern and gain measurement setup. The end launch connector of the antenna is covered with high frequency absorbing material.	105
Fig. 5-30. Simulated (red lines) and measured (with covered connector, dashed black lines) radiation patterns of the E-SIGW horn.	106
Fig. 5-31. Connector fed E-SIGW horn covered by a couple of strip-via soft surfaces.	107

Fig. 5-32. Geometry and transmission coefficient of the designed strip-via soft surface for the antenna frequency band ($W_s = 0.7$, $G_s = 0.15$, $P_s = 0.8$ mm).	107
Fig. 5-33. Electric field distribution around the connector fed E-SIGW horn at 60 GHz (a) Without soft surfaces (b) With soft surfaces.....	108
Fig. 5-34. Connector fed E-SIGW horn with soft surfaces (red solid lines, simulation) and without soft surfaces (black dashed lines, simulation; blue dotted line, measurement).	109
Fig. 5-35. Measured and simulated gain performance of the horn ($p = 0.87$ mm, periodicity of the unit cell).	110
Fig. 5-36. Geometry of the proposed air-filled contactless SIW horn.....	112
Fig. 5-37. Contactless SIW horn unit cell for middle thin layer with dispersion diagram.	113
Fig. 5-38. Contactless SIW horn unit cell for around thick layers with dispersion diagram.	113
Fig. 5-39. Simulated reflection coefficient of the multi-layer contactless air-filled SIW horn with 15 μ m gap between the layers.....	114
Fig. 5-40. Simulated radiation patterns of the contactless air-filled SIW horn with soft surfaces (red line) and without soft surfaces (blue line).	115

List of Symbols

λ	Wavelength
λ_g	Guide wavelength
λ_o	Wavelength in free space
ϵ_o	Permittivity of free space, 8.854×10^{-12} F/m
ϵ_r	Relative permittivity of medium
$\epsilon_{r(eff)}$	Effective relative permittivity of medium
c	Speed of electromagnetic waves in vacuum ($2.99792458E8$ m/s)
dB	Decibels
f_o	Resonant frequency
GHz	Gigahertz, 10^9 hertz
S	S-parameter
$\tan \delta$	Loss tangent
THz	Terahertz, 10^{12} Hertz
η_o	Intrinsic impedance of free space
Ω	Ohms
Z_o	Characteristic impedance

List of Acronyms

3D	Three Dimensional
AMC	Artificial Magnetic Conductor
BW	Bandwidth
CBCPW	Conductor-Backed Coplanar Waveguide
CPW	Coplanar Waveguide
CST MWS	Computer Simulation Technology Microwave Studio
EBG	Electromagnetic Band Gap
EM	Electro-Magnetic
E-SIGW	Elevated Substrate Integrated Gap Waveguide
GaAs	Gallium Arsenide
H-TEM	Horizontally Polarized Transverse Electromagnetic
LTCC	Low Temperature Co-Fired Ceramic
MMIC	Monolithic Microwave Integrated Circuit
MM-Wave	Millimeter Wave
PCB	Printed Circuit Board
PMC	Perfect Magnetic Conductor
PRGW	Printed Ridge Gap Waveguide
RGW	Ridge Gap Waveguide
SIW	Substrate Integrated Waveguide
SIGW	Substrate Integrated Gap Waveguide
TE	Transverse Electric
TEM	Transverse Electromagnetic
TEM-RGW	Transverse Electromagnetic Ridge Gap Waveguide
TEM-PRGW	Transverse Electromagnetic Printed Ridge Gap Waveguide
TM	Transverse Magnetic
TRL	Through-Reflect-Line
V-TEM	Vertically Polarized Transverse Electromagnetic

Chapter 1

INTRODUCTION

The massive and extensive congestion at the available radio frequency spectrum has resulted in severe spectrum scarcity which has become as a primary problem when trying to launch new wireless services. This spectrum scarcity has accelerated the research works in millimeter wave frequencies or even higher frequency band where the wide unallocated spectrum is available for the variety of wireless applications. Accordingly, different problems and technical factors have been realized in designing high-frequency RF components such as the necessity to have lower cost, smaller size, perfect packaging, and low power dissipation.

The RF front-end of the wireless devices includes active and passive sections. The active components usually composed of monolithic microwave integrated circuit (MMIC) technology that enables the active section to occupy a compact space of the module area. However, the passive components which are composed of antennas and filters have not been advanced to be fit some compact size as active devices because of fabrication tolerances and geometrical scaling determined by the frequency of operation.

The conventional well-characterized transmission lines such as rectangular waveguides, microstrip line, and coplanar waveguide (CPW) have been widely utilized in the variety of complex RF components. However, at millimeter frequencies or above, there are some issues regarding these conventional technologies.

The rectangular and cylindrical waveguides demonstrate a quite low loss at high frequencies; but, they should be manufactured in split blocks. These blocks are usually connected by screwing, diffusion bonding or deep-brazing techniques, which are costly, complicated, and sometimes not scalable to the higher frequencies. This is because of the considerable reduction in physical dimensions of the rectangular and cylindrical waveguide components by approaching the operation frequency of the waveguide to the millimeter waves that require a high level of precision for manufacturing and assembling the waveguide split-blocks. Besides, excellent electrical contact, as

well as the perfect alignment of the blocks, are needed to avoid tiny gaps between the waveguide segments. These mechanical requirements besides protection from corrosion and oxidation of the contacting layers over the life cycle increase manufacturing cost and effectively prevent the mass production of the components for commercial purposes.

The conventional microstrip and coplanar lines are the most typical planar transmission lines, which present a robust and low-cost solution as well as being suitable to integrate active microwave components on the printed circuit boards (PCB). However, the transmission properties of these lines closely depend on the substrate parameters. As the result, they suffer from a high insertion loss at millimeter frequencies because of the presence of the lossy dielectric material. The power leakage due to surface waves in the dielectric substrate causes serious crosstalk and interference problems on various printed circuit transmission lines [1]-[3]. Moreover, the spurious radiations in the form of surface waves especially from the discontinuities in the feeding network of the microstrip antennas can dramatically influence the antenna radiation patterns, which are difficult to handle [4].

To fill the existing performance gap between the planar transmission line and non-planar metal waveguide, researchers have tried to establish the technologies that are as low cost and flexible as microstrip and as low loss as the metal waveguide. Accordingly, low loss thin film microstrip lines [5], [6], substrate integrated waveguide (SIW) [7]-[9], and low temperature co-fired ceramic (LTCC) [10], [11] have been introduced. Although these technologies have somehow filled the gap between planar transmission lines and the conventional metal waveguides, they are all based on propagation inside the dielectric, which is not efficient in millimeter-wave and terahertz frequency bands. Therefore, at high frequencies, there is a necessity for re-thinking in RF design techniques in order to reach a technology with the improved electrical performances, flexible manufacturing and self-packaging capabilities, and affordable cost.

1.1 Ridge Gap Waveguide

As mentioned, the increasing demand for the high data rate communication necessitates the utilization of higher frequencies. Therefore, designing the efficient and cost-effective microwave

components at higher frequency has become of great importance. In recent years, a new metamaterial-based guiding structure supporting propagation in a gap between two parallel metallic plates has been introduced by Kildal that is known as ridge gap waveguide (RGW) [12]-[14]. In fact, the RGW technology appeared as an extension of the research on the hard and soft surfaces [15] and is a new type of waveguide that supports propagation on a ridge which is surrounded by a textured surface on the both sides. The soft surface is capable of suppressing wave propagation with any polarization along the surface while the hard surface enhances the propagation along the surface.

In 2009, the existence of local waves following the ridges of a hard corrugated surface had been discovered [16], and later it was further developed as gap waveguide by keeping only one ridge and replacing the rest of them with metal pins [17]. The ideal RGW utilizes the basic cutoff band related to PEC-PMC parallel plate waveguide configuration as long as the air gap separation between the plates is less than a quarter of a wavelength to suppress all wave propagation in the other directions. Therefore, the electromagnetic wave would be controlled to propagate in the gap between the middle ridge and the upper conducting plate. In Fig. 1-1, the PEC-PMC cutoff concept and the ideal configuration of the RGW are illustrated.

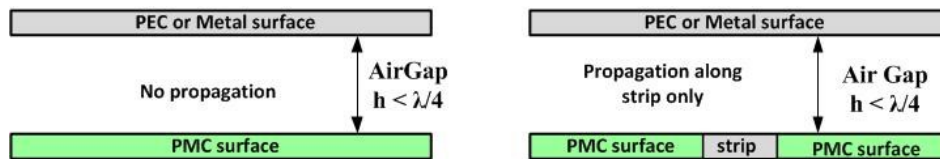


Fig. 1-1. Configuration of ideal ridge gap waveguide.

Therefore, the main performance of the gap waveguide is defined by its ability to make parallel-plate stopband around the ridge allowing the EM wave to be confined within a region or propagate towards the desired direction instead of spreading out in all other directions. However, since the perfect magnetic conductor (PMC) is not available in nature, it is realized by the artificial magnetic conductor (AMC) over a specific bandwidth. The first AMC in the RGW is realized by the periodic pins known as ‘fakir’s bed of nails’ [18]-[19].

The bed of nail structure around the ridge is divided into unit cells, including a single pin with a gap on its top to the PEC covering. For the bed of nails lattice, the unit cell dimensions, including

its height, width, and top gap distance determine the stop band provided by the periodic structure. The defined stop band is the difference between the start frequency when the parallel mode propagation stops around the ridge and the end frequency when the parallel-plate modes propagate again. The stop band provided by the periodic structure can be understood by analyzing a single unit cell by extracting its dispersion relation with frequency. The single dispersive-less mode propagation at the available stop band can also be extracted by the dispersion analysis of the cells in the existence of the ridge. The groove gap waveguide that is the other configuration of the RGW without having the propagating ridge in the same level of the periodic nails also offers a low insertion loss at high frequencies, which is very similar to that of conventional rectangular waveguide [20], [21].

The low loss feed network, which is needed for the high gain array antennas are built in [22], [23] with slots placed on the top metal plate making a slot array design without having strict requirements of good electrical contacts between the slotted metal plate and the bottom feed structure. The slot array design based on groove gap waveguide is introduced in [24]-[26]. A resonant 8-element array was given in [27], [28] in which the slots are in the narrow wall of the groove gap waveguide, but they were not inclined to avoid the high cross-polar problem. Instead, they are excited by tilting parasitic dipoles.

The printed version of the RGW also known as the printed ridge gap waveguide (PRGW) is introduced in [29], [30] and developed in [31]-[32]. In this type, the ridge is printed on a dielectric substrate, which is surrounded by the mushroom shape lattice including patch and metallic vias on a grounded substrate realizing a high impedance surface (ideally a perfect magnetic conductor). The PRGW is usually fed by the microstrip line with a thickness equal to the gap height of the waveguide [32]. The PRGW upper conductor that is supported by another substrate layer is attached to the microstrip ground plane.

1.2 Challenges and Problems with Ridge Gap Waveguide

The RGW structure is well-known as a low loss guiding medium, especially at high frequencies because of supporting the quasi-TEM mode of propagation in an air medium. However, the

propagating mode is relatively dispersive in comparison with the pure TEM, which can propagate in the air medium. In fact, the entire ground plane in the RGW results in quasi-TEM propagation because the ridge and the extended ground plane operate like an air-filled microstrip line. In other words, despite having a stop-band structure in the area around the ridge, the propagation is not entirely confined to the ridge, and the solid upper plane causes lots of fringing fields outside the ridge boundary. This is mostly because the entire top plane is not intended to cut the continuity of the waves outside the ridge borders. As a result, the first unit cell after the ridge suffers from strong fringing fields continued by the upper plane and cannot operate adequately to suppress the whole power around the ridge and the rest of the suppression is left to the second and third rows of the cells. In fact, the medium around the ridge, which is equipped with the bed of nails or lattice of mushroom unit cells, functions as a high impedance surface (HIS) for the propagating mode; however, the upper conductor does not follow the same feature, and it supports leakage of the wave outside the ridge borders. Consequently, because of this horizontal asymmetry on the propagation medium, the TEM propagation only happens in the middle area of the ridge and the whole propagation is characterized as the quasi-TEM.

As the gap size and the distance between the cells are very small, having a considerable power on the first row of the cells may decrease the peak power-handling capability (PPHC) of the structure. Moreover, it obliges us to consider more rows of the cell around the ridge to provide better propagation suppression or to weaken the coupling between adjacent RGW lines. This enlarges the components and devices made with this technology.

One of the significant challenges in designing the RGW components is determining the characteristic impedance of the RGW lines. Since there is no accurate close form and exact formulation for the RGW characteristic impedance, putting a transmission line with arbitrary impedance in the middle of the circuit where there is no direct contact with the standard transmission line is not easily possible. So far, microstrip or stripline impedance relations have been utilized to approximate the RGW characteristic impedance. However, the most reliable method to realize the characteristic impedance of the RGW is to connect it to the impedance-known standard transmission line, such as microstrip line, through a transition and finding its right

width by reaching the best return loss response. Repeating this procedure to all impedances makes the design process tediously long and increases the chance of mistakes.

In Chapter 2, a new configuration of the RGW is introduced, which supports the TEM propagation instead of the quasi-TEM mode of the traditional type. Therefore, as the line is supporting pure TEM mode, the impedance of the line can be easily extracted using the characteristic impedance of the parallel plate waveguide. In addition, the TEM-RGW shows better isolation than the conventional one.

1.3 Air-Filled Substrate Integrated Waveguide

The conventional hollow waveguides are the desired guiding structures at millimeter frequencies because of their known low loss and high power handling. However, in order to integrate with a system, it should be machined as a groove within the metal and then covered with a metal sheet that should be screwed around the groove to assure good electrical contact which finally end up with the hollow waveguide. The machining procedure may be accepted up to certain frequency bands, but at millimeter frequencies, high accuracy is required, and the electrical contacts between two metals may not be warranted. The invention of substrate integrated waveguide (SIW) technology was a promising start to satisfy these demands, which have caught considerable attention over the last decade [33]-[36]. The waveguide is formed from the double side grounded substrates by making the waveguide sidewalls with the metal-plated via holes. This waveguide supports transverse electric waves, unlike the rectangular waveguide with the solid side walls that supports the transverse electric and transverse magnetic waves.

Recently, the SIW has shown spread use because of its low cost, compact size, and the ability to design many microwave circuit components on the same substrate and it is considered as an integrated alternative to the conventional bulky waveguides. For this structure to be similar to the rectangular waveguide; some conditions must be met in the design of the conducting via side walls [37]. However, it should be clear that the similarity is not necessarily complete if we consider the fact that the leakage of the signal is possible through the periodic gaps between the adjacent metal

vias, which could dissipate some of the power to the dielectric out of the predetermined propagating region.

The SIW structures are usually designed and fabricated on the available standard laminates with the given characteristics that are used in the design procedure. But, the manufacture of the dielectric substrate material provides the electrical characteristics of the dielectric materials at lower frequency bands. At frequencies much higher than the given frequency band in the laminate data sheet, such as millimeter wave frequency bands, their characteristics are unknown and cause some ambiguity and uncertainty at the design procedure since they demonstrate somehow different behavior than the lower frequencies. In addition, as the frequency of the operation is on rising, the existence of the dielectric material inside the propagating medium results in undesirable dielectric losses, which become severe at millimeter frequencies; besides of the possible anisotropic nature of the dielectric material. In fact, as a guiding structure filled with dielectric material, transmission loss along the line has always been to the higher end in the SIW-based circuits [38], [39]. Also, the dielectric filling inside the waveguide reduces the average power handling capability (APHC) of the conventional SIW in comparison with the corresponding air-filled waveguides.

To reduce the SIW dielectric losses, air-filled SIW is more desirable for high-frequency applications. To create an air-filled SIW, the dielectric material between the via-holes must be depleted, which we cannot find any technology that can do that. A simple method to realize the air-filled SIW is to cut the dielectric material and cover the top and the bottom with metal plates. In light of this, multilayer PCB based SIW structure containing an air-cut in the middle sections has been introduced in [40] with only computational analysis of the attenuation constant and a cutoff frequency of the air-filled SIW. Recently in [41] -[44], the air-filled SIWs made of a multilayer printed circuit board which are connected to a transition from a dielectric-filled SIW and microstrip line have been presented, and their superiority over conventional dielectric-filled SIW has been demonstrated in terms of loss, Q-factor, and power handling capabilities.

1.3.1 Problems Associated with the Air-Filled Integrated Waveguides

All of the PCB based multi-layer air-filled integrated waveguides introduced so far require a complete and flawless smooth connection on the top and bottom layers to the intermediate

substrate. Because it is possible to have leakage of the waves from the possible infeasible air gaps that might exist between the top and the bottom conductors and the intermediate substrate holding the via-holes. In other words, the performance of such an air-filled integrated waveguide is closely correlated to the quality and the perfection of the top and bottom metal plates' connection to the intermediate layer since these multilayer waveguides have a great potential of leakage from any discontinuity or bad connection of the layers. The tight connections in the given prototypes in [45] and [46] are realized by many closely located screws that tight the whole layers around the guiding medium. This mechanism of tight connection around the waveguide impedes its utilization for the designs where the SIW lines are closely located and have to be sealed to protect any leakage between the lines.

This can be overcome by two alternative methods. The first method is to connect the upper and lower conductors with a conducting adhesive and press firmly to assure the electric contacts; the second possible method is to glue the top and bottom conductors to the intermediate substrate before making the via-holes. After that, the via-holes can be done. The second method seems more realistic and assures the electrical contacts. However, if the dielectric substrates are thick, restrictions are applied to the via-hole diameter that might make the design impossible. In addition, utilizing glue between the layers that are partially depleted is not a reliable solution, especially for the wide circuits because there is a possibility of leaking adhesive glue inside the air-filled region, which is sometimes completely out of control and demands expensive fabrication procedure with high precision.

To tackle these problems, an innovative solution is recommended in Chapter 3 which is very promising for higher frequency applications. In fact, it will open a new area of the substrate integrated technologies in order to reach a new type of substrate integrated waveguide, which is completely isolated and has lower losses at the millimeter wave frequencies with the cheap connection of the layers. To solve the issues regarding excitation of the proposed air-filled SIW, a new configuration of coplanar waveguide is introduced in Chapter 4. Utilizing this coplanar line eliminates the discontinuity problem of the air-filled SIW when it is being excited by conventional transmission lines. Quasi-static analysis of this line based on conformal mapping is also given in

this chapter to extract an approximate relation for the line characteristic impedance for its different dimensions.

1.4 Substrate Integrated Horn Antenna

The horn antennas are probably the simplest and the greatly used microwave antennas. They are basically a device which provides a transition between waves propagating in a transmission line and wave disseminating in an unbounded medium such as free space. Horn antennas have been designed and constructed in different kinds of shapes to control one or more of their fundamental properties such as gain, radiation pattern, and impedance [47]. The bulky geometry of the traditional horns limits their use in a compact size at high frequencies.

The invention of SIW technology has revolutionized the employment of planar horn antennas into the microwave and millimeter-wave circuits. From the family of horn antennas, the *H*-plane sectoral horn that is formed by flaring a waveguide in the plane normal to the electric field can be accomplished by using SIW technology which is firstly introduced in [48]. In fact, after Vivaldi antenna, the substrate integrated *H*-plane horn is the second integrated traveling wave antenna. This antenna which is the simplest and lightest version of horn antennas has transformed most of his ancestors' behaviors into the integrated format.

The antenna has got considerable attention, because of its compact size and potential of being integrated with the baseband circuits, to introduce new designs or improve its performance and characteristics. In [49], etching elongated transverse slot on the top end of the horn while closing the horn aperture has provided the antenna with a broadside radiation. In this structure, the primary horn aperture was completely closed by continuous vias to force the waves to propagate through the slot which is etched on the top end of the substrate. The authors called the antenna as broad side radiating horn. However, the antenna is not operating like horn antenna, and it is a flared waveguide exciting a wide slot without any sign of traveling wave behavior. An on-chip integrated *H*-plane horn antenna was studied and fabricated with a standard GaAs 0.5- μm MMICs process in [50]. This antenna which has a very compact size of $1.8 \times 1.8 \text{ mm}^2$ and exhibits 4.36 GHz input - 6 dB bandwidth at the center frequency of 91.09 GHz is mainly designed to be integrated into W-band GaAs MMICs single-chip RF transceiver. The gain of the *H*-plane substrate integrated horn

is improved by adding tapered vertical slots to the antenna aperture at millimeter frequencies in [51], [52]. In fact, the H -plane horn at this design operates as a feed for the array of vertical slots that are mounted at the aperture of the horn. The pattern of the antenna is improved in both principle planes at millimeter frequency range; however, adding the tapered slots resulted in the 3D structure of the antenna with the somehow complicated fabrication process.

Furthermore, many studies and investigations have been conducted to make improvement in the performance of simple substrate integrated H -plane horn antenna. Generally, the ideal design for a horn is to have more uniform amplitude and phase distribution in the aperture so that higher directivity and narrower beam width can be achieved. One of the ideas that has been vastly used to improve the performance of a simple H -plane horn is the extension of horn substrate in front of the aperture. In [53], [54] the dielectric substrate inside of the H -plane horn has been extended and formed in different shapes to be considered as a lens in front of the horn. The dielectric loading may serve as the phase corrector in the H -plane; however, extended dielectric enlarges the antenna length. The extended dielectric can also improve the antenna matching to some extent, but it is restricted to the thicker substrates (typically larger than $\lambda_0/6$) with lower dielectric constant. In other words, the extended dielectric could function as a transition from the aperture to the air medium, but since it continued with the same dielectric constant, the dielectric-air discontinuity did not improve considerably. In light of this, in [55], the extended dielectric of the horn is perforated using air-via holes in different steps to make a smooth transition from the antenna aperture to air medium. Perforating the extended substrate decreases its effective permittivity to the lower values, and with a higher number of perforations with a larger diameter of the air via holes it goes toward the values close to unity. Smoothing the aperture-air discontinuity of the integrated H -plane horn by perforating its extended dielectric improves the antenna matching performance through decreasing standing wave intensity inside the horn medium. But, in order to obtain a considerable improvement in the antenna matching several steps of perforations have to be applied to the extended dielectric of the antenna which needs more extension of the dielectric depending on the dielectric constant of the substrate. For the proposed horn the enhanced impedance bandwidth of 40% from 16 to 24 GHz with a return loss better than 10dB was obtained by drilling the dielectric slab with three different diameters. The method is only effective for the

integrated horn antenna with the electrically thick substrate. However, for thinner substrates, the antenna performance does not improve. It should be clear that the impedance matching bandwidth is closely related to the substrate thickness and not to the horn design parameters. For the horn antennas made with thin substrates (a thickness of less than $\lambda_0/10$), a new type of transition was introduced in [56]-[59] with their circuit model to improve the horn impedance bandwidth. This transition is composed of a couple of printed strips on the both sides of the extended dielectric from the horn aperture. The results show that applying one printed step transition adds a single band of matching while increasing the number of transition steps results in multiple matching bandwidths. This solution is more efficient with the integrated H -plane horns with thin substrates, but it does not modify the radiation characteristics of the conventional horn.

A new phase correcting solution of SIW H -plane horn was introduced in [60]. Three series of embedded metal-via arrays have divided the SIW horn into three sub-horns by which phase distribution across the horn aperture has become uniform. For this antenna, the uniform phase front was shown with the simulation results due to the division of the aperture to three sections. However, the proposed method could not be useful at all because the metallic via assigned to the aperture are destroying the aperture field distribution by changing the boundary conditions at the aperture area. In other words, instead of having a tapered electric field amplitude across the horn aperture, multiple maximums and minimums of field distribution appear at the radiating aperture which demolishes the radiation pattern. Besides, a very thick substrate is used for the horn at the operating frequency with wide feeding line which makes lots of contributions in the antenna main radiation pattern that is completely evident from the 60 degrees of tilt in the E-plane pattern.

The ridge substrate integrated waveguide (RSIW) was also applied inside the substrate integrated horn with tapered ridges along the horn to reach a wider reflection response from a coaxial fed substrate integrated horn in [61]. The illustrated simulation results show a wide band impedance matching for this antenna; however, the fabrication procedure seems to be very complicated since tapered ridge should be applied along the integrated horn. Also, in the case of microstrip feeding, which is preferable for the antennas of this type, the RSIW would not be able to operate adequately.

1.4.1 Problems Associated with Substrate Integrated Horn Antennas

The substrate integrated horn antenna has been struggling with a variety of challenges since its invention. This antenna which is an H -plane horn antenna is the only one from the horn antenna family that can be fabricated in the integrated with the substrate. Since the SIW is actualized by densely arraying of metalized posts inside a two-sided grounded substrate, the only freedom in flaring waveguide walls is the E-walls, which are formed by the via-holes connecting the upper and lower plates of the substrate. Unlike conventional horn antennas, the aperture of this antenna includes a dielectric-air discontinuity at the substrate edge where the metalized posts of the horn walls are stopped continuing to deliver the guided wave inside the horn to the free space. In other words, as a traveling wave antenna integrated into a substrate, the inside propagating waves see a major discontinuity when they reach to the antenna aperture, which causes a significant standing wave inside the horn. The integrated antennas are more inclined to be integrated with other supporting circuits, which are mostly mounted on high dielectric constant substrates (such as GaAs or LTCC); therefore, the aperture discontinuity is becoming more critical. As a result, the standing waves inside horn cause poor return loss response of the antenna at the feeding point. The severity of the high reflection is intensified when the antenna is integrated into a thinner substrate. In fact, most of the available standard thickness substrates are not providing the required height of the aperture for the integrated horn, especially at lower frequencies when the thickness of the substrate is less than $\lambda_0/10$. Therefore, the dielectric-air discontinuity and the thin thickness of the aperture are coming together to provide the integrated H -plane horn with a high reflection response that makes the antenna practically useless.

Also, since the edges of the two-side grounded substrate form the aperture of this antenna, it operates like a suspended slot in the free space with lateral ground planes. Therefore, the radiated waves from the aperture are easily supported by the solid ground planes of the substrate on the both sides, that is, the surrounding conductors help the aperture to contribute and intensify the antenna back radiations easily.

Because the configuration of this antenna takes advantage of the planar structure, the antenna is mostly preferred to be fed with planar feeding transmission lines such as microstrip line or

coplanar waveguide line. Since the geometry of these lines is not symmetric in both planes, using them as an excitation causes an asymmetry in the E -plane radiation pattern of the horn. Besides, because of the radiating nature of the microstrip line width and the thick substrates, it adds more limitations to the substrate thickness of the horn. Consequently, selecting the right substrate thickness for the integrated horn, which is fed by a planar transmission line, is another design challenge.

As a member of the horn antenna family, the metallic walls surround the antenna aperture. In H -plane horn, the H -walls are supporting the dominant propagating mode of the antenna. However, the E -walls are suppressing this mode, which makes the tapered aperture distribution with maximum intensity in the middle and minimum close to the walls. Since the substrate integrated antennas are desired to occupy minimum space with the surrounding circuits, benefiting from maximum aperture efficiency is more advantageous for these antennas. The four-corner PEC wall of the regular H -plane horn limits the aperture efficiency by tapering the aperture distribution. For a horn integrated into a substrate, the only parameter that can improve the efficiency is the aperture width since the thickness is fixed. However, widening the aperture does not considerably affect the efficiency if the horn length is fixed, due to the increase of the aperture phase error. Therefore, for a particular geometry, the antenna efficiency cannot increase beyond a certain level. This constrains the application of the single integrated horn antenna and necessitates utilizing an array of this horn to increase the antenna gain by a few dB. Besides, the feeding network that should be included with the array adds more losses and limits the antenna frequency band with a mandatory extension in the whole antenna size. As a result, improving the aperture efficiency of a single element of this antenna would have a beneficial effect on its applications with the integrated circuits.

In Chapter 5, new designs of the substrate integrated horn antenna are introduced, which solve the aforementioned problems and enable the integrated horn to overcome its difficulties making it a strong candidate for millimeter wave applications of compact size devices.

1.5 Dissertation Outline and Contributions

This thesis is organized into six chapters, including the introduction. In Chapter 2, a new configuration of ridge gap waveguide (RGW) is proposed. This setting provides a guiding medium very similar to the ideal parallel plate waveguide that enables the ridge gap waveguide to support TEM waves propagating instead of the quasi-TEM waves of the conventional type. The TEM propagation enables us to easily extract the characteristic impedance of the waveguide from the ideal parallel plate characteristic impedance expression with minor modifications. The TEM based RGW provides a lower insertion loss and higher isolation in comparison with the conventional gap waveguide.

In Chapter 3, the configuration of the air-filled SIW has been developed to overcome the problem of possible electrical misconnection between the waveguide layers. This is realized by introducing the double sided AMC slab around the air-filled propagation medium. The AMC surfaces around the air-filled guiding medium provide PEC-AMC parallel plate stop band region when the PEC lids are covering the waveguide, which is very advantageous at millimeter wave frequencies because it considerably reduces the cost of layers connection.

Also, the partially air-filled conductor-backed coplanar waveguide (CBCPW) is introduced in Chapter 4 to propose an efficient and reliable feed line for the contactless air-filled SIW. The quasi-static analysis of this new transmission line is accomplished to obtain an approximate relation for its characteristic impedance with different line parameters.

The innovative configurations of the substrate integrated horn antenna, which has a wide potential to be integrated with the RF circuits, are introduced in Chapter 5. The new configurations have resolved the intrinsic problems of this antenna to be easily utilized in the millimeter wave devices. Chapter 6 provides conclusions and future works.

Chapter 2

TEM PRINTED RIDGE GAP WAVEGUIDE

2.1 Proposed Configuration

As mentioned in Chapter 1, in the conventional ridge gap waveguide (RGW) configuration, the stop band region around the guiding ridge is provided by a periodic structure separated from a full ground plane functioning as PEC-AMC parallel plate with a separation of less than quarter of a wavelength. The entire upper ground plane of the conventional RGW, as shown in Fig. 2-1(a), does not provide the same boundary condition of the lower edge of the propagation medium. In the proposed configuration, as shown in Fig. 2-1(b), the complete upper conductor is replaced with another ridge surrounded by the AMC surfaces as the lower layer. In other words, the ideal structure would be a double ridge waveguide which is surrounded by the AMC surfaces on the top and bottom sides. Therefore, instead of PEC-AMC parallel plate in the conventional RGW, here the AMC-AMC parallel plate region around the double ridge providing a cutoff region of the

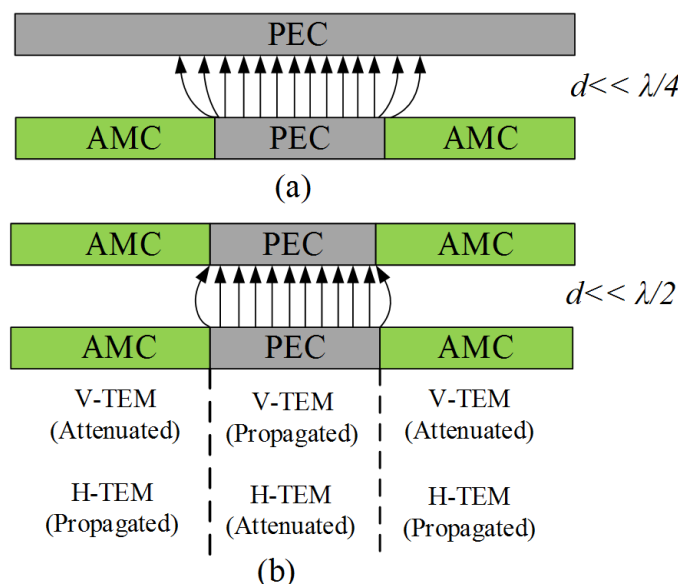


Fig. 2-1. (a) Geometry of a single texture side (conventional) RGW (b) Proposed TEM-RGW with symmetric double texture sides.

vertically polarized TEM waves (V-TEM), which are supported between the double ridges, but will allow the horizontally polarized TEM waves (H-TEM) to propagate if excited. Thus, one would consider the AMC-AMC/PEC-PEC parallel plate region with a gap separation less than a half wavelength to support H-TEM/V-TEM waves and when the gap is a half wavelength or more, both regions will support H- and/or V-TEM waves. In Fig. 2-1 (b), the structure is symmetric around a horizontal line in the middle of the gap, which will be referred to as a horizontally symmetric medium. The AMC-AMC configuration can be realized by the two sets of periodic structures that are symmetrically facing each other. Therefore, the unit cells of the complete periodic structure around the double ridge would include a couple of face-to-face nails or mushrooms that are separated by a gap distance of less than a half wavelength, as shown in Fig. 2-2.

In the RGW implemented by the bed of nails, there is almost no restriction on choosing waveguide and periodic structure dimensions such as gap height, periodic pin dimensions, and pins periodicity and they can be determined based on the required frequency band of the operation. However, for the printed version of the RGW, which is implemented with the dielectric substrates, there is much less freedom in the selection of waveguide parameters. For instance, the metal pin height of the periodic structure should be limited to the available substrate thicknesses. Therefore, the cell is taking the mushroom shape instead of a single pin, to compensate the required cell height. Even if a single pin inside the standard dielectric that satisfies the required cell height must

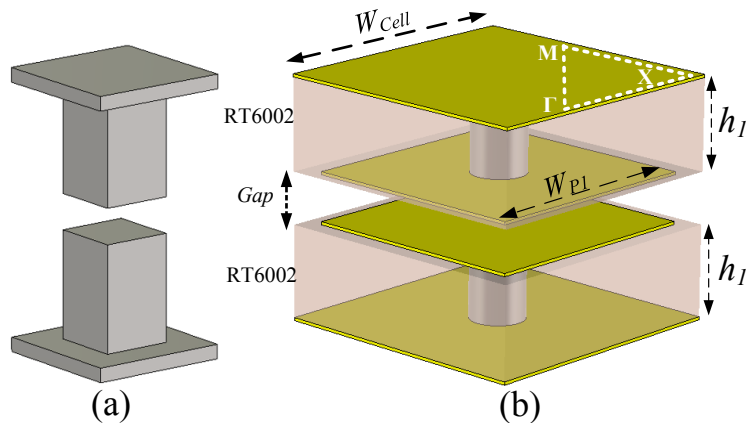


Fig. 2-2. (a) Double pin (double texture) and (b) Proposed mushroom unit cell (double texture) of TEM-RGW configuration ($W_{cell}=1.5$, $h_1= 0.508$, $gap= 0.254$, $W_{pl}=1.3$ mm).

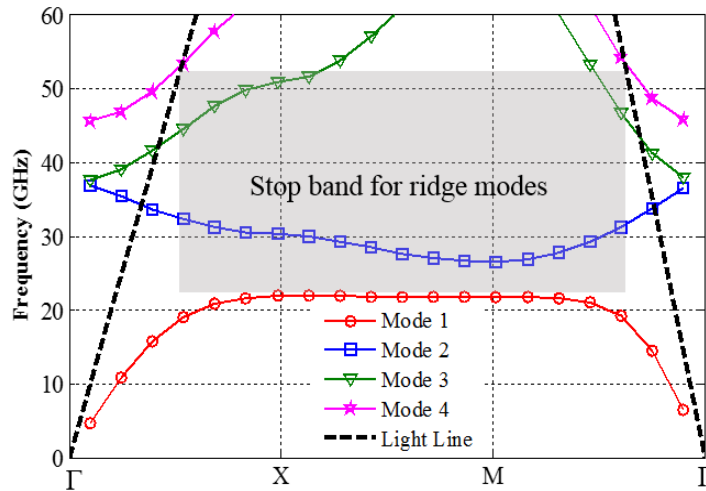


Fig. 2-3. Dispersion diagram of the AMC-AMC periodic structure with double mushroom unit cell of Fig. 2-2(b).

have a pad of a minimum size related to the substrate thickness and the via diameter as required by the manufacturer. In addition, in the case of feeding the waveguide with the planar transmission line, the gap height must be limited to the standard substrate thicknesses.

The unit cell in Fig. 2-2(b) includes two identical mushrooms separated by the middle gap, the mushroom substrates are chosen to be RO6002 of 20 mils thickness, and the middle gap height is set to be ten mils, to be equal to one of the available standard substrate thicknesses. As stated above, two high impedance surfaces are created facing each other. To realize the supporting modes of the AMC-AMC periodic structure comprising this unit cell, the dispersion analysis of the cell is accomplished by the Eigenmode solver of CST Microwave Studio as shown in Fig. 2-3. By looking to the dispersion results, it seems that the AMC-AMC setup does not offer any wide band gap to be used around guiding ridges. However, by close study of the modes polarizations in the dispersion diagram and comparing them with the ridge mode polarization, it can be concluded that all the modes appeared in the dispersion diagram of the AMC-AMC periodic structure would not be excited on the double ridge gap waveguide (DRGW) when a V-TEM mode is propagating on the ridge.

As seen from Fig. 2-4, the second and third modes of the AMC-AMC configuration, which are horizontally polarized will not be excited on the DRGW and only Mode 1 and Mode 4 have the

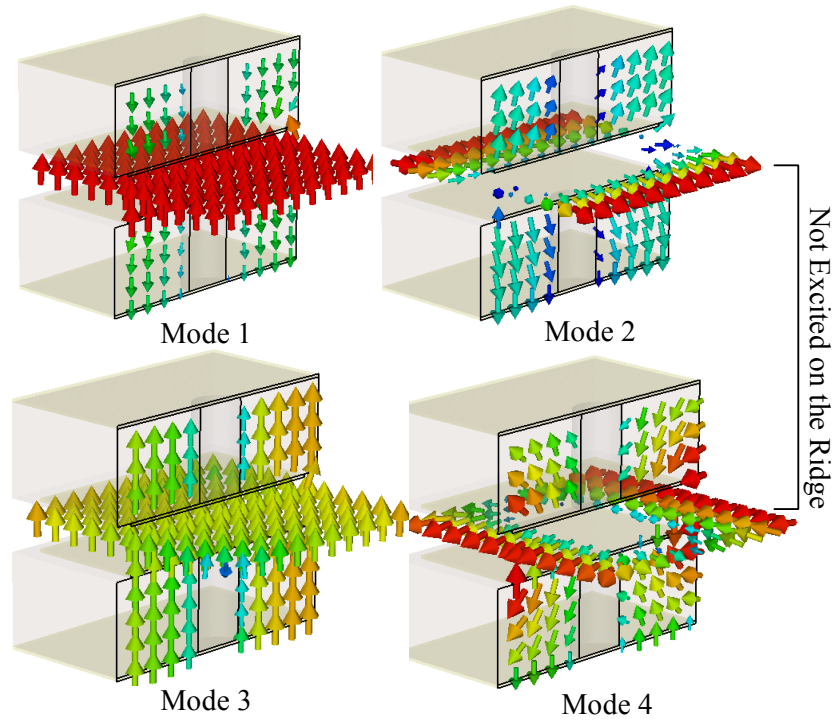


Fig. 2-4. Electric field distribution of the different modes of double mushroom unit cell.

vertical polarization that is supported by the DRGW. Therefore, the band gap of the ridge modes for this unit cell would be between Mode 1 and Mode 4, which is from 22 GHz to 52 GHz based on the light lines given in the diagram. With this understanding, the configuration of the TEM-RGW provided in Fig. 2-1(b) can be realized by the double mushroom printed unit cell as shown in Fig. 2-5(a). The waveguide is excited by ideal wave ports provided by the simulator. The definition of this port should be carefully considered to capture the whole fringing fields around the ridge. The optimum definition of the wave ports is also shown in Fig. 2-5(b). Based on this definition, the wave port width should be extended at least one period of the unit cells from the edges of the printed ridges. In Fig. 2-6, the dispersion diagram of the proposed TEM-PRGW including a couple of parallel ridges, which are surrounded by three rows of the face to face mushroom cells is plotted, with an ideal TEM propagation line known as the light line. The ridge supported TEM mode could not be detected as a single mode by the Eigenmode simulator, and its different sections are distributed among other horizontal modes in the ridge modes band gap. This band gap (V-TEM band gap) shown in Fig. 2-3 is wider than the bandgap of a single textured structure (conventional PRGW) with the same gap height. To keep the same bandgap in the double

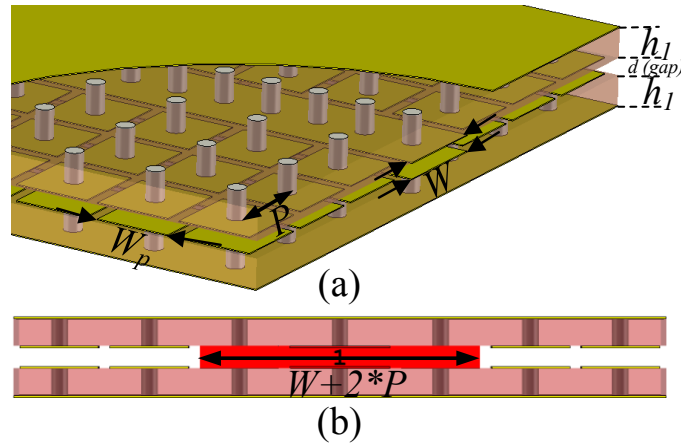


Fig. 2-5. (a) Isometric view of the double texture TEM-PRGW, (b) Side view showing the wave port excitation definition ($P=W_{cell}$).

texture as the single texture, the gap height should be double of the single texture one. That is simply because the double texture case can be considered the image of the single texture after removing the PEC plate. The reflection and transmission coefficient responses of the TEM-PRGW of Fig. 2-5(a) with the length of four wavelengths at the middle frequency of the stopband, excited by the wave ports, is shown in Fig. 2-7. As seen from this plot, from 30 GHz to 45 GHz, which is the middle frequency bandwidth of the ridge modes (V-TEM) stopband, the waveguide shows a low insertion loss performance. As mentioned, unlike the single textured ridge gap waveguide with

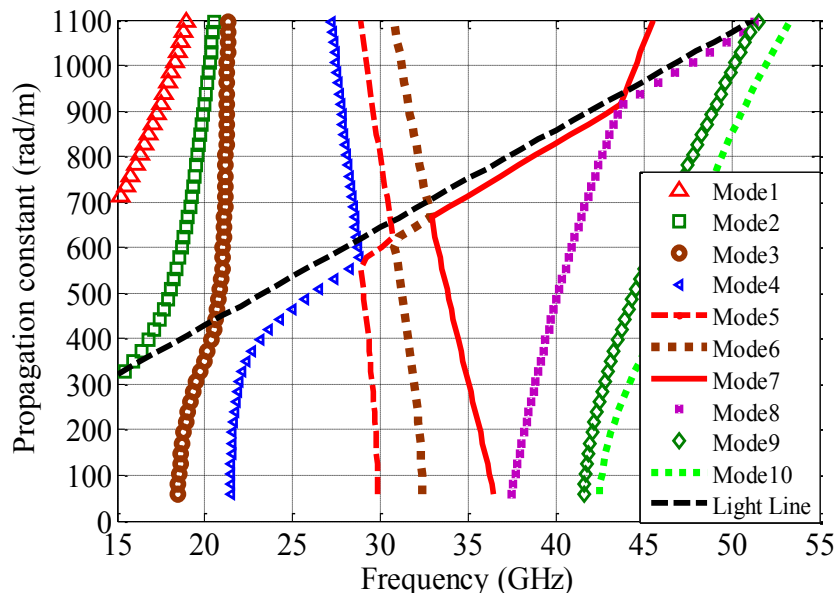


Fig. 2-6. Dispersion diagram of the TEM-PRGW with three rows of unit cells around the guiding ridges.

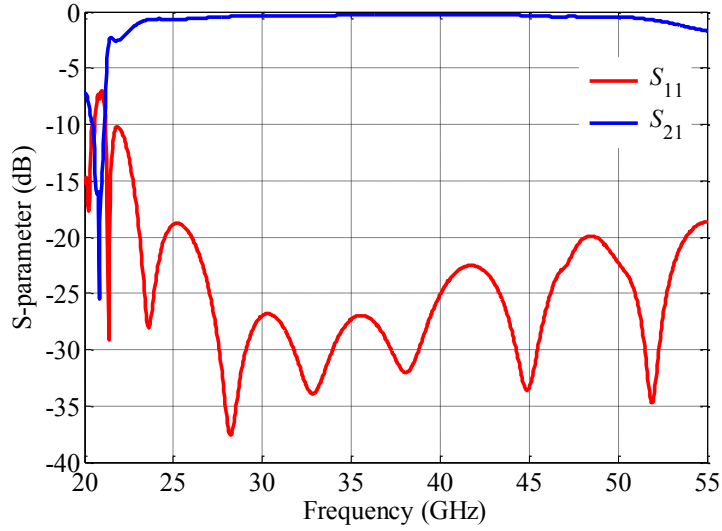


Fig. 2-7. Reflection and transmission coefficient of the TEM-PRGW.

a whole upper metal plate, the proposed double texture structure is symmetric around the horizontal middle plane. As the boundary conditions of the top and bottom edges are identically supporting the restriction of the propagation, the waves are confined between two ridges with minimum deviation from the lateral sides. Therefore, this waveguide is expected to have a lower insertion loss in comparison with single texture RGW, in which upper ground plane is not supporting the wave confinement. In Fig. 2-8, a comparison is made between transmission

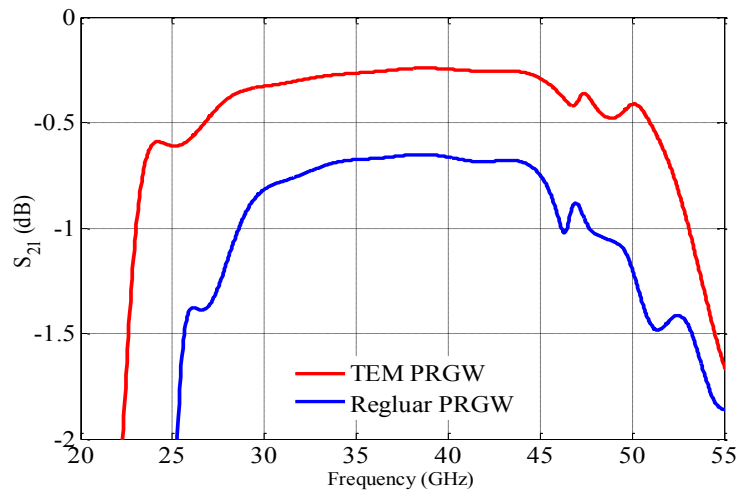


Fig. 2-8. Transmission coefficient comparison between the proposed double texture TEM-PRGW and single texture conventional PRGW with gap of $d=0.254$ mm with two wavelength long.

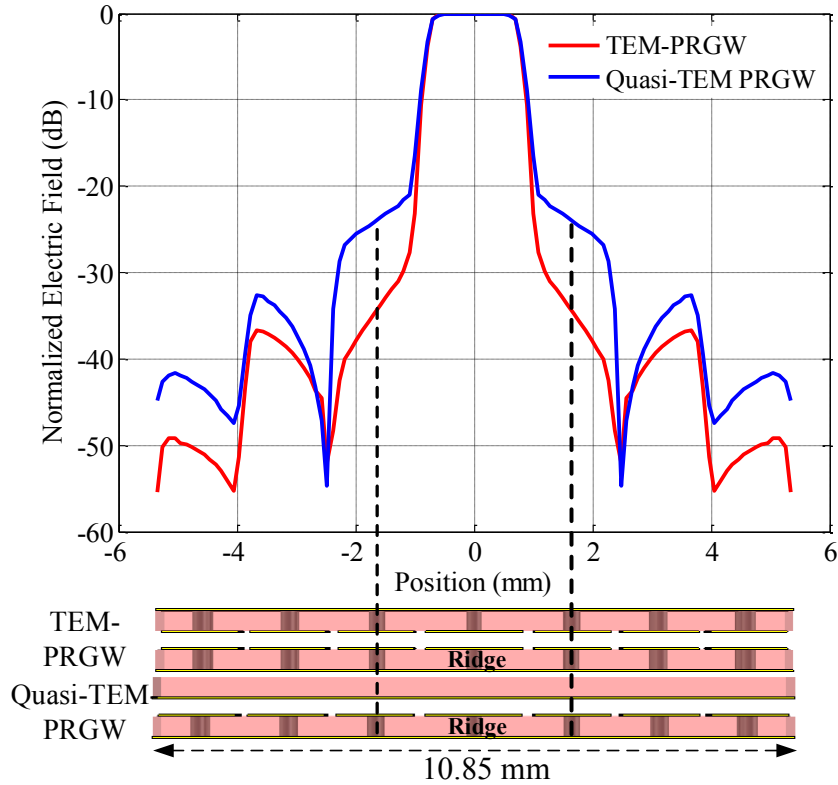


Fig. 2-9. Comparison between the normalized electric field distribution along the transverse cross section of a TEM-PRGW and Quasi-TEM-PRGW at 37 GHz with gap of $d = 0.254$ mm.

coefficient of this TEM-PRGW and the quasi-TEM-PRGW with the same length and the gap height. As expected, the TEM-PRGW shows lower insertion loss than the quasi-TEM-PRGW because the propagation is entirely confined between two identical ridges. In this comparison, the same wave port excitation is used for both waveguides, and their periodic structures are supporting the same stopband in the comparison bandwidth.

The electric field distribution of the proposed TEM-PRGW and conventional quasi-TEM-PRGW along the cross section of the waveguide are compared at 37 GHz in Fig. 2-9. As seen from this comparison, the electric field intensity over the first row of the TEM-PRGW cells is 10 dB lower than the original PRGW. The field intensity is dropped considerably outside of the propagating ridge in the TEM-PRGW case. Therefore, the wave propagation is more trapped between the parallel ridges along the guide in the TEM-RGW, which enables the propagation in this waveguide to be more isolated than the regular RGW. As a result, fewer rows of the cells,

comparing with the conventional one, around the guiding medium could be used to suppress the coupling between the adjacent lines.

2.2 Characteristic Impedance Extraction of TEM- and Quasi-TEM-PRGW

The characteristic impedance of the proposed TEM-RGW should be very close to the parallel plate impedance expression given as:

$$Z_0 = \eta d/W \quad (2-1)$$

where $\eta = \sqrt{\mu/\epsilon}$ is the intrinsic impedance of the medium between the parallel plates, W is the strip width, d is the separation between them. However, in this expression the lateral walls of the parallel plate waveguide are assumed PMC walls without considering the fringing fields from the edges of the finite strips. Thus, there is no field variations in the transverse direction. The characteristic impedance of the proposed TEM-PRGW extracted from simulation is compared with

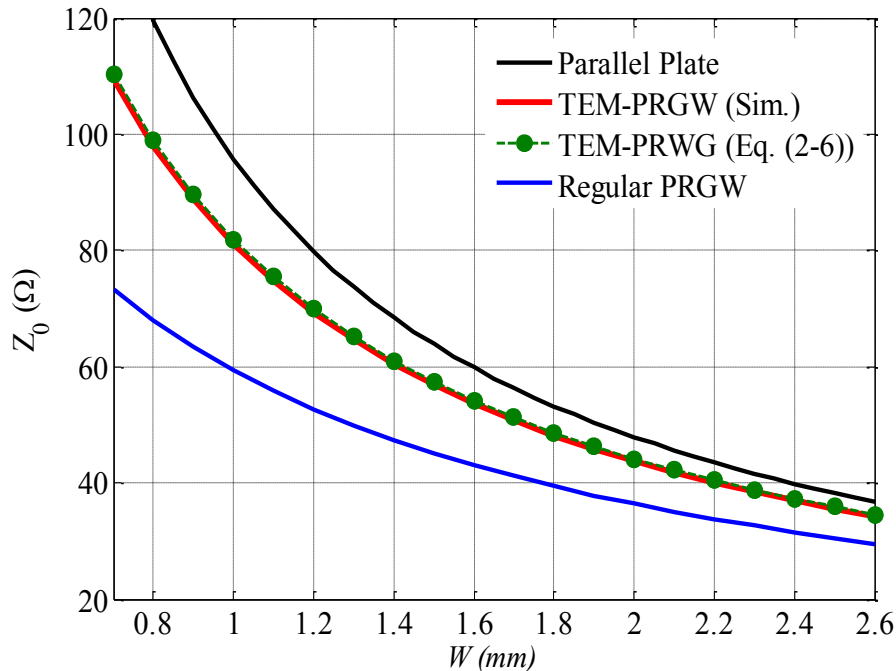


Fig. 2-10. Characteristic impedance of parallel plate waveguide (Eq. (2-1)), proposed TEM-PRGW (full wave simulation and Eq. (2-7)), and regular PRGW with a gap of $d = 0.254$ mm.

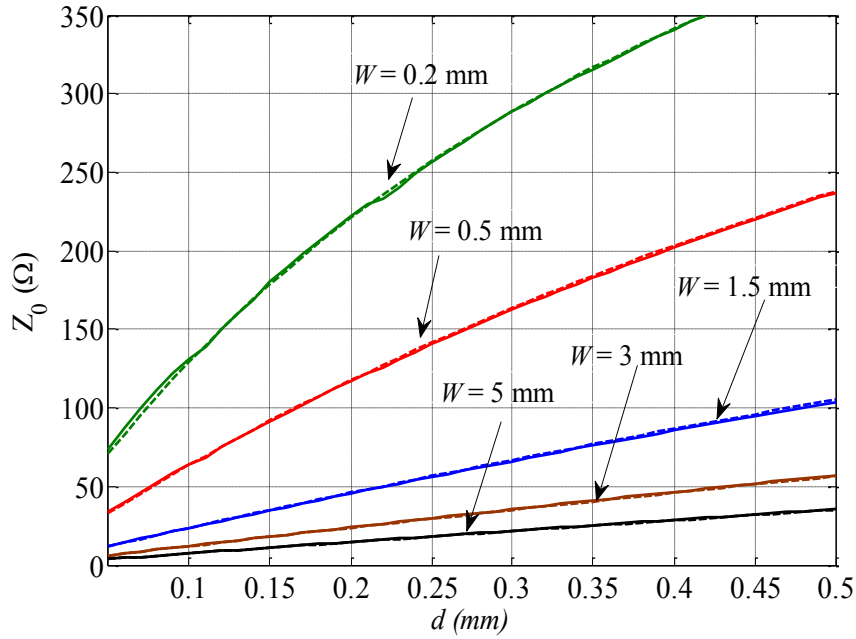


Fig. 2-11. Comparison between full wave simulated characteristic impedance (solid line) and those obtained from (2-6) (dashed line) of the TEM-PRGW for different widths.

the characteristic impedance of the parallel plate waveguide in Fig. 2-10. As seen from this comparison, the characteristic impedance of TEM-PRGW, which is realized by the printed ridges is very close to the impedance values of the ideal parallel plate waveguide because of the similarity in boundary conditions around the guiding medium in both. The differences in the strip width for a certain impedance comes from fringing fields around the real strips of the TEM-PRGW, which increase the effective width of the strip. Besides the characteristic impedance of the corresponding quasi-TEM-PRGW (with the same gap height) is also included in this plot and since it supports q-TEM mode of propagation, the parallel plate impedance approximation is not close to its characteristic impedance.

The parallel ridges of TEM-PRGW impedance can be obtained using the parallel plate impedance relation by replacing the physical width W with the effective width (W_{eff}). So, the impedance expression of (2-1) can be expressed as:

$$Z_{0(TEM-RGW)} = \frac{\eta d}{W_{eff}} \quad (2-2)$$

where

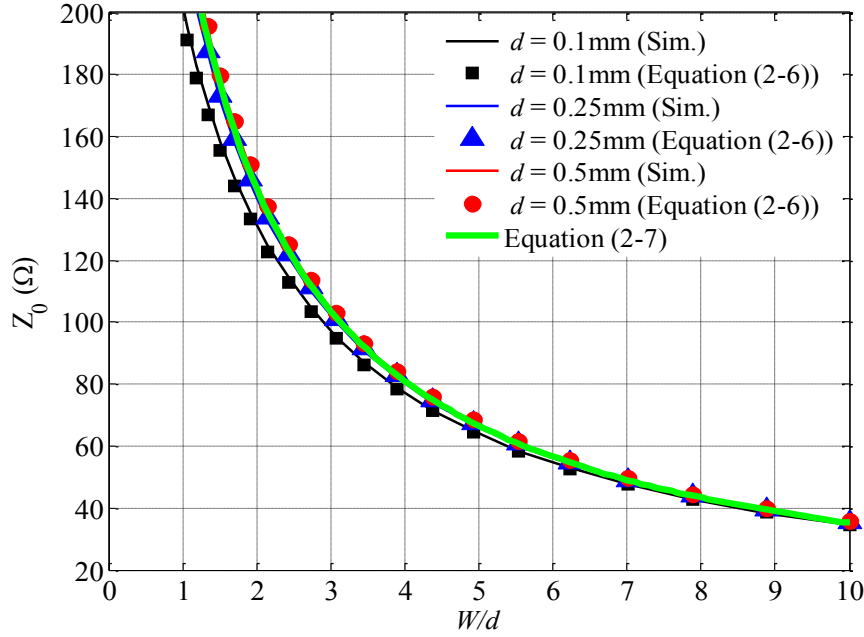


Fig. 2-12. Characteristic impedance of the TEM-PRGW vs. ratio of width to gap height obtained from full wave simulation and (2-7).

$$W_{eff} = W + \Delta W. \quad (2-3)$$

Moreover, ΔW is the effect of the fringing fields around the W edges, and is varying with the distance of the plates d , which is the gap height in the TEM-PRGW configuration. Therefore, it can be expressed as:

$$\Delta W = f(d). \quad (2-4)$$

Several full-wave analyses have been accomplished for a variety of TEM-PRGW configuration to reach an optimum and simple expression for $f(d)$ and finally the following empirical expression is obtained for the effective width of the parallel ridges, by considering all dimensions in millimeter:

$$W_{eff} = W + 0.502d + 0.04. \quad (2-5)$$

Therefore, the characteristic impedance of the TEM-RGW can be expressed as:

$$Z_{0(TEM-RGW)} = \frac{\eta d}{W + 0.502d + 0.04}. \quad (2-6)$$

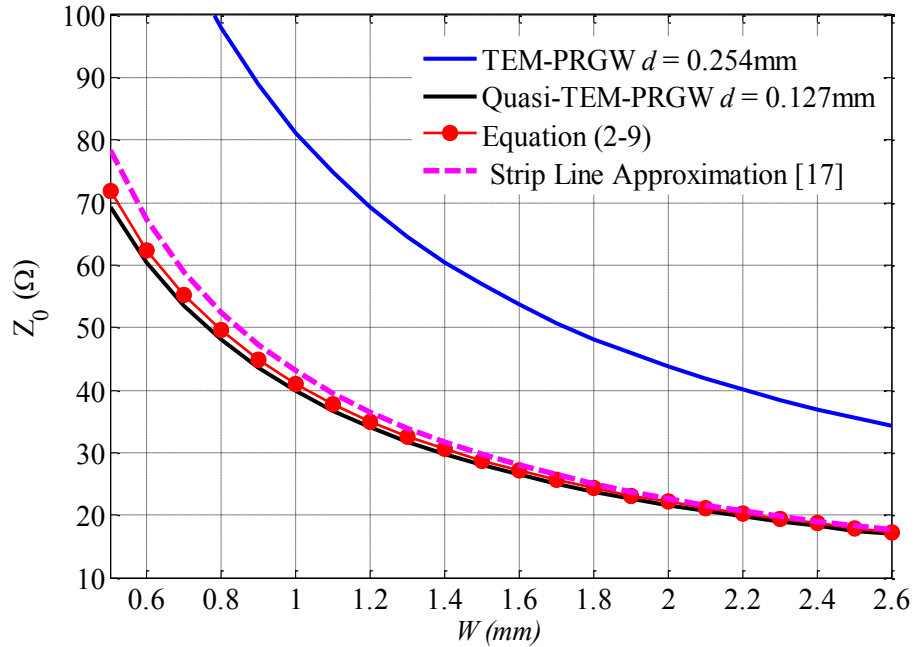


Fig. 2-13. Characteristic impedance of quasi-TEM-PRGW and the TEM-PRGW equivalent compared with those obtained in [17].

The impedance values of the TEM-PRGW with a gap of 0.254 mm obtained by (2-6) are also plotted for different widths in Fig. 2-10. These impedances which are represented by the dashed green line are very close to the full wave simulated impedances for the proposed guide.

To be certain of wideband operation of the TEM-PRGW, the gap height cannot exceed a certain value because the stopband width of the periodic structure around the ridges is inversely proportional to the height. In Fig. 2-11, the impedance obtained from (2-6) for the TEM-PRGW with different widths of the ridges versus the gap height are compared with the full wave simulated results for gaps of less or equal 0.5 mm to ensure the ridge modes are suppressed by the periodic structure. Besides, the characteristic impedance variations with the ratio of W/d is given in Fig. 2-12 for the gap distances of 0.1, 0.25, and 0.5 mm. From this comparison, it can be concluded that for the ratio of $W/d > 1$, which is most common in the practical designs, the impedances obtained from (2-6) and (2-7) agree with those of the full wave simulated values.

A generalized expression for the characteristic impedance of the TEM-PRGW based on W/d is obtained as follows:

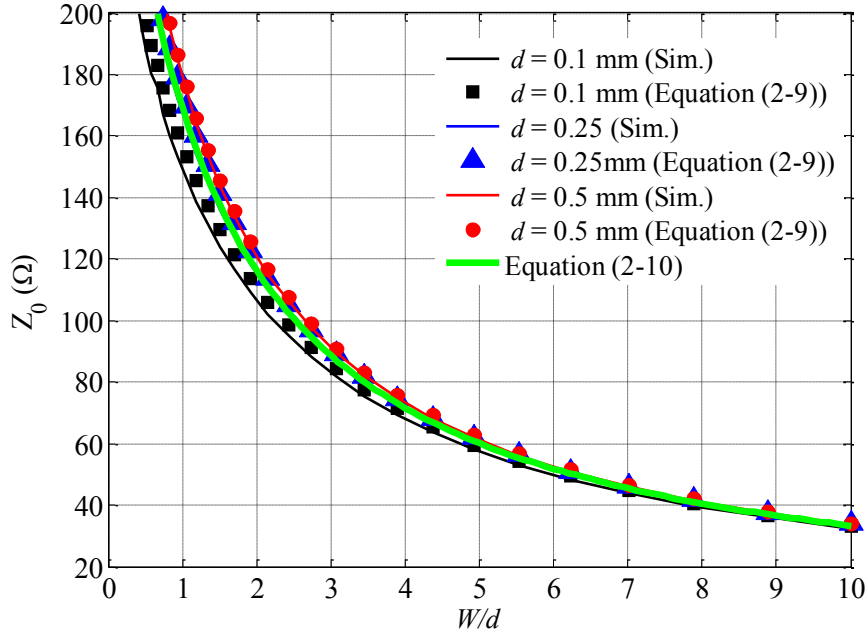


Fig. 2-14. Characteristic impedance variation of the quasi-TEM-PRGW with W/d .

$$Z_{0(TEM-PRGW)} = \frac{\eta}{1.01 \frac{W}{d} + 0.61} . \quad (2-7)$$

The proposed configuration of the TEM-RGW with the gap d is equivalent to the single textured case of the regular RGW with the half gap height ($d/2$). Therefore, the characteristic impedance of the single texture ridge gap waveguide (quasi-TEM-RGW) with the half gap height ($d/2$) can be determined by the simple formulation of the TEM-RGW with full gap height (d). In other words, instead of complicated microstrip and stripline approximations used for the ridge gap waveguide, which is carrying quasi-TEM mode of propagation, the characteristic impedance of this guide can be easily extracted from its TEM equivalent. In light of this, the impedance of the regular RGW with a gap height d can be written as:

$$Z_{0(RGW)}(gap = d) \cong \frac{1}{2} Z_{0(TEM-RGW)}(gap = 2d) . \quad (2-8)$$

Therefore, the characteristic impedance of regular RGW can be closely approximated, by considering all dimensions in millimeter, with the following simple equation based on (2-6):

$$Z_{0(RGW)} \cong \frac{\eta d}{W + d + 0.04} . \quad (2-9)$$

A comparison is made between values of (2-9) and the expression in [17] with the full wave simulation of the impedance of the PRGW and the double gap height of the TEM-PRGW in Fig. 2-13. The impedance values of (2-9) agrees better with the full wave simulation. Based on the relation given in (2-8), the impedance expression of PRGW in terms of W/d can also be written as:

$$Z_{0(PRGW)} = \frac{\eta}{1.01 \frac{W}{d} + 1.22} . \quad (2-10)$$

In Fig. 2-14, the impedance values obtained from (2-9) for various d and (2-10) are compared with the simulated impedance of PRGW for which the band gap is assured within the frequency of operation. Finally, it can be concluded that the high impedance line of the TEM-PRGW is wider than the width of the quasi-TEM-PRGW. Therefore, the high impedance lines of the proposed TEM-RGW will have fewer losses in comparison with the conventional type.

2.3 Modified Configuration of TEM-PRGW

As shown in Fig. 2-4, the proposed unit cells for TEM-RGW including two identical mushrooms are supporting horizontal mode propagations in the band gap of the excited modes on the ridge. As these modes are not supported by a straight ridge, therefore they would not exist around the guiding medium. However, at the discontinuity regions where the line is not continuing straightly, there is a potential of exciting the H-polarized modes that will propagate between the AMC-AMC and not between PEC-PEC. This could cause a leak outside the structure. Therefore, to control the propagation and confine the waves within the ridge borders at all discontinuities, the periodic structure should be modified to suppress the H -polarized waves in the ridge modes stopband. The given configuration for the TEM-RGW in Fig 2-1(b) is more inclined to support H -polarized modes because it has two identical parallel AMC surfaces. Disturbing the symmetricity of the periodic structure may interfere the excitation of the H -polarized modes. To reach this, the primary unit cell given in the Fig. 2-2(b) should be modified. One way is to shift upper layer of the periodic mushrooms for a half cell size in both horizontal directions. Therefore, a single cell would contain a whole mushroom at the lower layer and four quarters of a mushroom in the upper layer, as shown in Fig. 2-15. Dispersion analysis of this cell based on the irreducible Brillouin zone is given in Fig. 2-16. As seen from the diagram, only in the middle section of the diagram, the horizontally

polarized modes are not being supported by the periodic structure in the ridge modes stopband. However, in the first and the last regions, they would be excited such as the main cell of Fig. 2-2(b). Therefore, identical AMC surfaces would not provide a complete stopband for the H -polarized modes in AMC-AMC configuration around the guiding ridges.

It has been found that the H -polarized modes are less prone to be excited when the AMC surfaces are not identical. In fact, as the periodic structures around the guide are not ideal PMC surfaces, and they have some percentage of being close to ideal PMC based on their impedances;

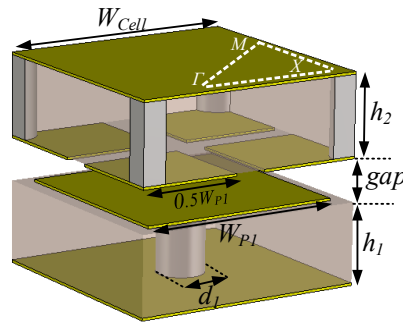


Fig. 2-15. Modified unit cell with shifted upper layer by a half cell size in both directions ($W_{p1}=1.3$, $d_1=0.3$, $h_1=0.508$, $h_2=0.508$, $gap=0.254$, $W_{cell}=1.5$ mm).

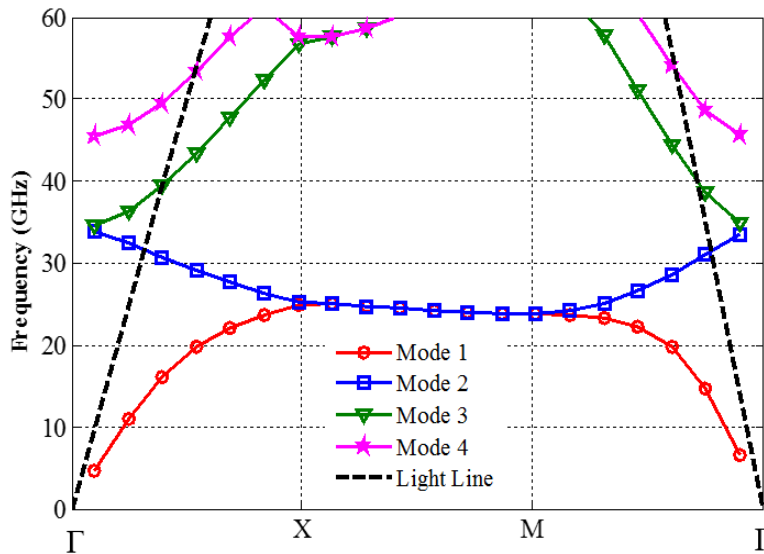


Fig. 2-16. Dispersion diagram of the modified unit cell in Fig. 2-15.

when their impedances are very close or equal together, the parallel polarized waves are strongly supported at a limited frequency band. Using different impedances for the AMC surfaces can intervene their performance of supporting H -polarized waves in the ridge modes (V-TEM) stopband. In light of this, the new configuration for the TEM-RGW would be like the geometry given in Fig. 2-17. In this waveguide, instead of having identical AMC layers on the top and bottom of the guiding gap, non-identical periodic structures for upper and lower layers are applied around the guiding ridges. This asymmetry in the AMC layers can be realized by using different sub-cell parameters in the top and bottom layers. Based on the double patch unit cell given in Fig. 2-2(b), two modified unit cells are provided in Fig. 2-18 in which the lower mushroom is kept the same as the previous cell and the upper mushroom dimensions are changed. In Fig. 2-18(a), the patch size and via diameter of the upper mushroom are reduced. In Fig. 2-18(b), the patch size of the upper mushroom is kept the same as the lower one, but the via diameter is maximized. The fabrication limitations of the available facilities such as minimum pad size and minimum via diameter of the PCB processes are considered in varying the dimensions. By these cells repeated periodically around the guiding ridges, dissimilar AMC layers are made which can stop the propagation of parallel polarized modes. With the dimensions given in Fig. 2-18, both cells are providing the same stopband, which is shown in the dispersion diagram of Fig. 2-19. As seen from this diagram, between first and second modes, a complete stopband is achieved all over the Brillouin zone. This stopband starts from 24.5 GHz and continues till 40 GHz. The cell size of the

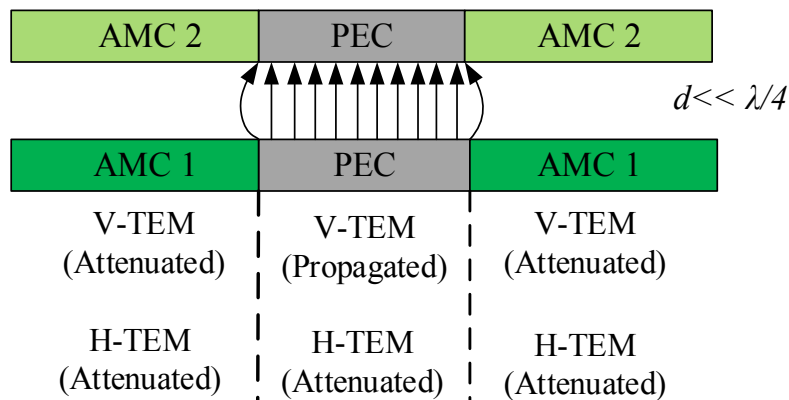


Fig. 2-17. Modified configuration of the proposed TEM-RGW.

modified cell is kept to be the same as the main cell in Fig. 2-2(b) so that the whole size of the guiding structure made by the simple and the modified configurations would be the same.

As we are inclined to modify the upper periodic structure to provide asymmetric AMC layers while keeping symmetric guiding region, different thickness of the substrates can also be applied to the layers to reach this purpose. Obviously, limited standard substrate thicknesses are available, which we have to be restricted to. In Fig. 2-20, two other modified cells are given which have a thinner substrate for the upper layer. In these cells, the lower substrate and the mushroom have kept the same as the previous cells in Fig. 2-18, and the upper substrate thickness and the mushroom dimensions are changed. The substrate thickness of 10 mils is the only thin option after

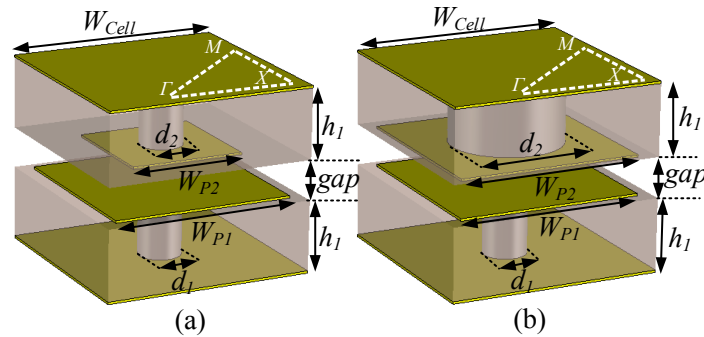


Fig. 2-18. The modified unit cells for TEM-PRGW with equal thicknesses, $W_{p1}=1.3$, $d_1=0.3$, $h_1=0.508$, $h_2=0.508$, $gap=0.254$, $W_{cell}=1.5$ (a) $W_{p2}=0.8$, $d_2=0.2$ (b) $W_{p2}=1.3$, $d_2=0.79$ (all in mm).

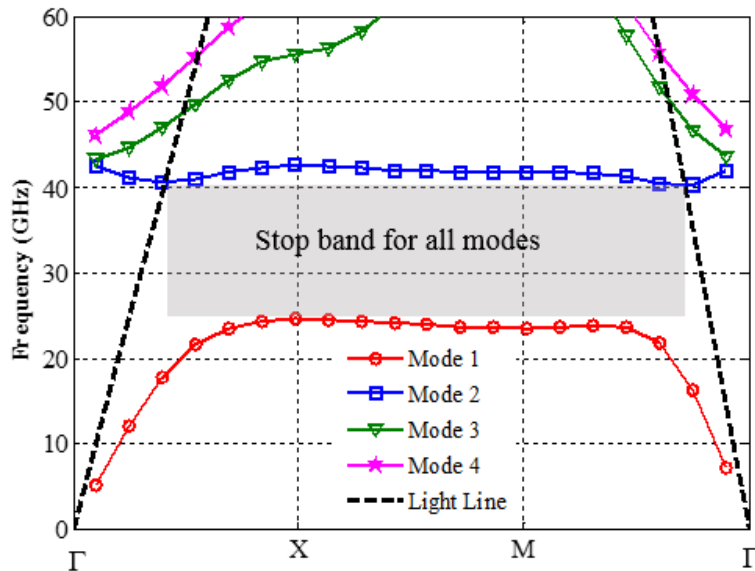


Fig. 2-19. Dispersion diagram of the periodic structure made by modified cells of Fig. 2-18.

20 mils, which can be processed to realize the periodic structure. With the given dimensions, both cells are resulting in almost the same dispersion response, which is given in Fig. 2-21. The stop band for these modified cells is between 24.5 - 47 GHz and is close to the stop band of the ridge modes in the diagram of Fig. 2-3, which is between 22 and 51 GHz. The stopband in the given dispersion diagrams is measured based on the light lines in the diagrams, which are the same for all of them because the cell size has not been changed during the modifications. As mentioned, selecting the cell dimensions is restricted by the available substrate thicknesses and the fabrication limitations. The dispersion analysis of the TEM-PRGW with modified cells of Fig. 2-20 is shown

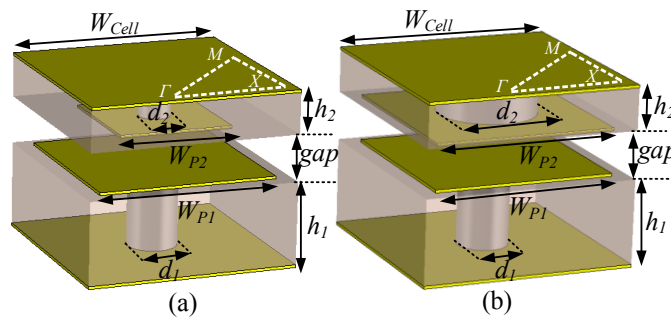


Fig. 2-20. The modified unit cells for the asymmetric TEM-PRGW with different thicknesses, $W_{p1}=1.3$, $d_1=0.3$, $h_1=0.508$, $h_2=0.254$, $gap=0.254$, $W_{cell}=1.5$ (a) $W_{p2}=0.7$, $d_2=0.19$ (b) $W_{p2}=1.3$, $d_2=0.79$ (all in mm).

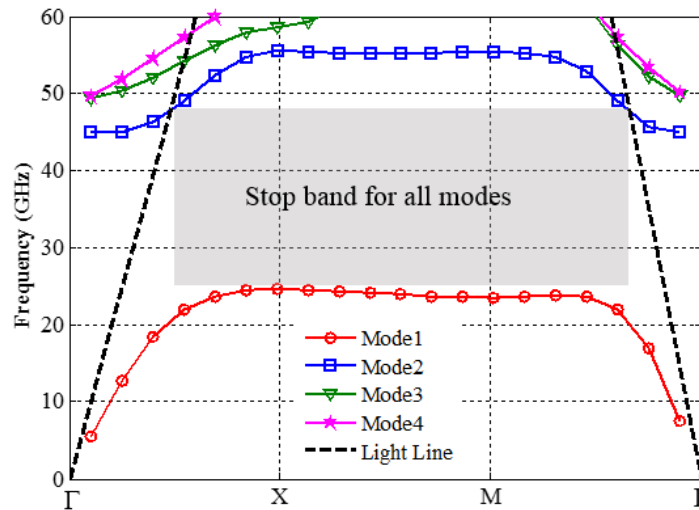


Fig. 2-21. Dispersion diagram of the periodic structure made by modified cells of Fig. 2-20.

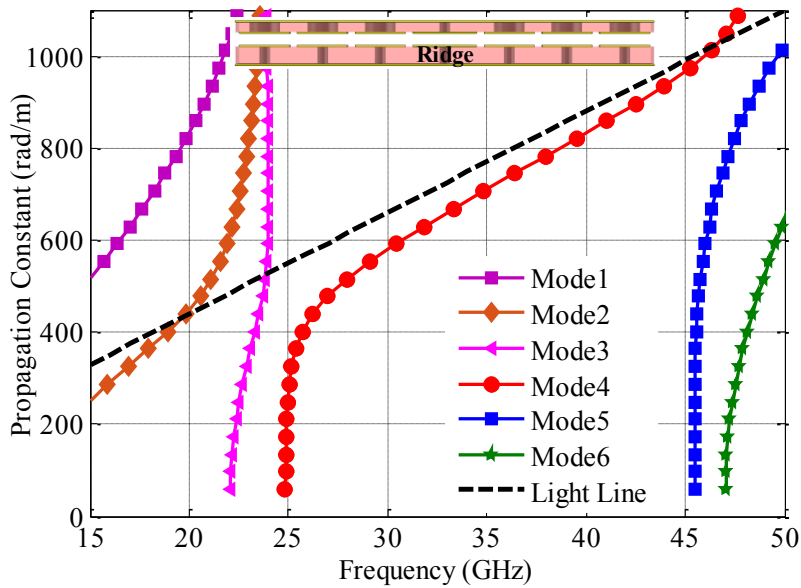


Fig. 2-22. Dispersion analysis of the one row of the TEM-PRGW with modified unit cells of Fig. 2-20.

in Fig 2-22. The single mode propagation of the TEM-PRGW at the stop band of the modified cells is identified as the fourth mode of the finite structure including the guiding parallel printed ridges surrounded by three rows of the double-patch cells on the lateral sides. To evaluate the proposed TEM-PRGW performances, the modified cells of Fig. 2-20 are employed for the all fabricated prototypes of straight and discontinuous waveguides.

2.4 Transition to Microstrip Line

To excite the TEM-RGW and measure its performance, it has to be connected to the standard transmission lines. The PRGW has been excited by rectangular waveguide [30] and by microstrip line [31], [32]. Exciting with the microstrip line looks more beneficial since the microstrip is also supporting quasi-TEM mode of propagation and is horizontally asymmetric in the direction of propagation as RGW, which makes it easier to design the transition. However, the gap height of the PRGW should be equal to a microstrip line substrate thickness, which is restricted to the limited standard thicknesses.

For the TEM-PRGW, the microstrip line can also be used for the excitation. But, since the microstrip line is unbalanced and has a solid ground plane, the transition between the microstrip

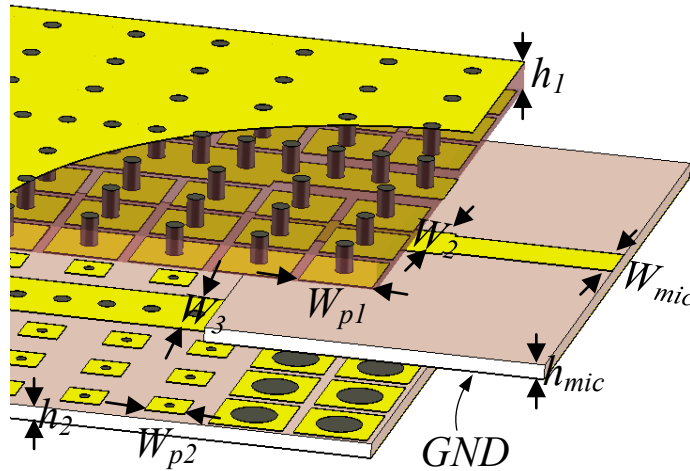


Fig. 2-23. Separated layers of the transition from microstrip to the TEM-PRGW with $W_{mic}=0.87$, $W_2=1$, $W_3=1.75$, $h_1=0.508$, $h_2=0.254$, and $h_{mic}=0.254$.

line and this waveguide should be a single texture conventional PRGW, which is also unbalanced and has a solid ground plane. The transition from the microstrip line to TEM-PRGW is shown in Fig. 2-23. Because of the considerable amount of the fringing fields around the microstrip line, its ground plane cannot stop suddenly in connection with the TEM-RGW. Therefore, the whole ground plane of the microstrip continues inside the TEM-PRGW and covers two rows of the lower cells to make quasi-TEM dielectric filled PRGW. The width of the line in the middle guide is also adjusted to match the 50-Ohm impedance of the microstrip. As the propagation of the waves is more concentrated between the ridge and the extended ground plane in the dielectric filled PRGW, there are much less fringing fields in comparison with the microstrip line. Thus, the ground plane of the quasi-TEM-PRGW can be switched to the periodic structure of the lower layer to deliver the wave propagation from unbalanced to the balanced waveguide. Accordingly, the 50-Ohm microstrip line connected to the 50-Ohm dielectric filled PRGW (W_2) and ended up with a 50-Ohm air-filled TEM-PRGW (W_3). For the microstrip substrate, which is the same substrate filling the PRGW, the RT5880 with permittivity of 2.2 is used, which has the thickness of 10 mils equal to the gap height of the waveguide.

2.5 Fabricated Prototypes

After finding the appropriate unit cells of the TEM-PRGW, which has a complete stop band for all possible modes, as shown in Fig 2-20, the prototypes of the straight and bend waveguides are

designed and fabricated based on these unit cells. In Fig. 2-24, the distributed layers of the fabricated TEM-PRGW configuration with unit cells of Fig. 2-20(a) is shown. In this configuration, the middle substrate, which contains the feeding microstrip line is depleted in the middle to provide the air medium for the propagation and extended from the lateral sides to fix the air gap distance between the TEM-PRGW layers that are meeting each other. Using AMC1 and AMC2 makes the structure not sensitive to the misalignment. However, two alignment holes are added to align the layers using dowel pins before screwing. As AMC1 and AMC2 appear independent of each other, the ridges misalignment could change the line characteristic impedance.

The layers are stacked on the top of each other and fastened with 6 plastic screws around the guiding medium. The feeding microstrip line is extended to be able to feed the waveguide with the

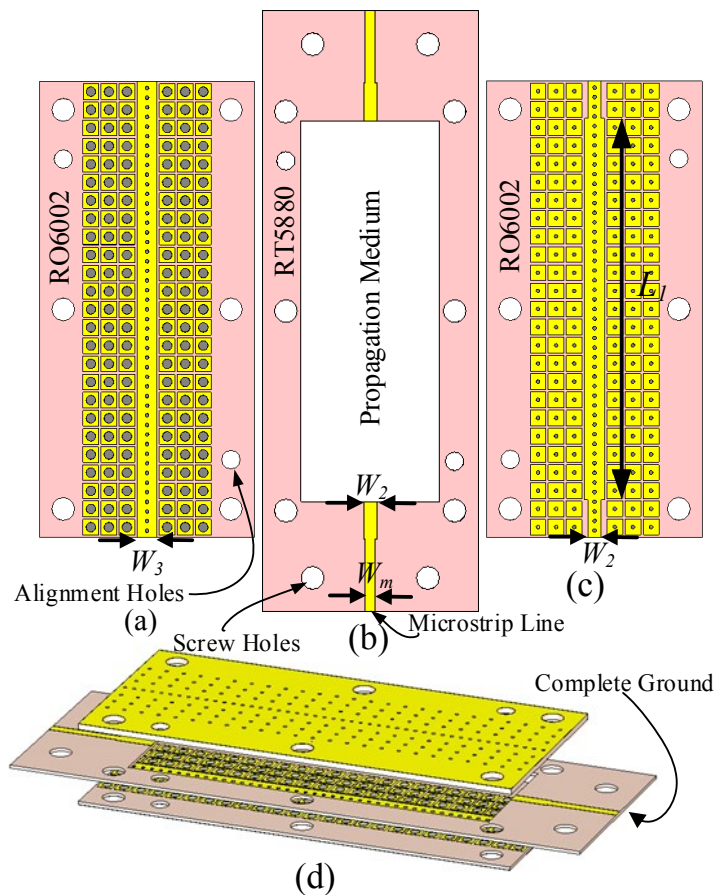


Fig. 2-24. Geometry of the TEM-PRGW with modified unit cell of Fig. 2-20(a), (a) Lower thin AMC layer with straight ridge, (b) Middle microstrip feeding layer, (c) Upper thick AMC layer with straight ridge, (d) 3D view of the stacked layers.

end launch connector. The fabricated prototype of this waveguide is shown in Fig. 2-25. As the transition is used to feed the main propagating waveguide, a TRL calibration kit is prepared to change the reference plane of the measurement from the feed point to the end of the transition, as shown in Fig. 2-26. The simulated and measured reflection and transmission coefficient results of this waveguide are shown in Fig. 2-27. Considering the 30-40 GHz as the stopband middle frequency of the modified cells, based on the dispersion diagram of Fig. 2-21, the measurement follows the simulated results of the waveguide with an acceptable agreement.

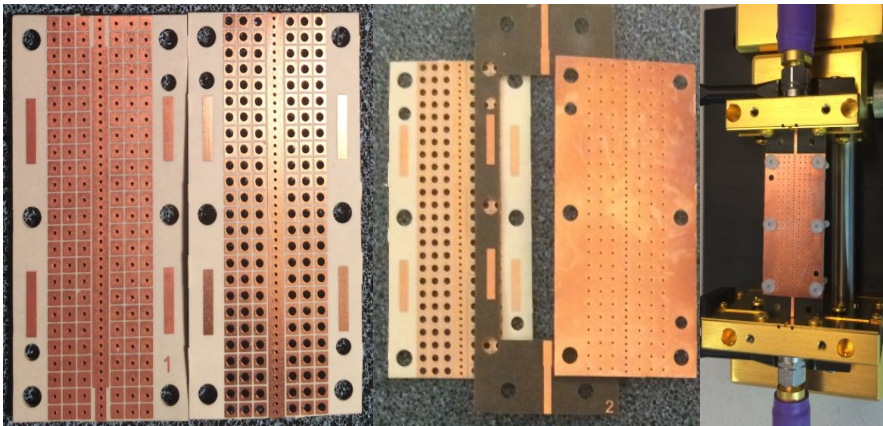


Fig. 2-25. Fabricated layers of the TEM-PRGW with modified cells of Fig. 2-20(a).

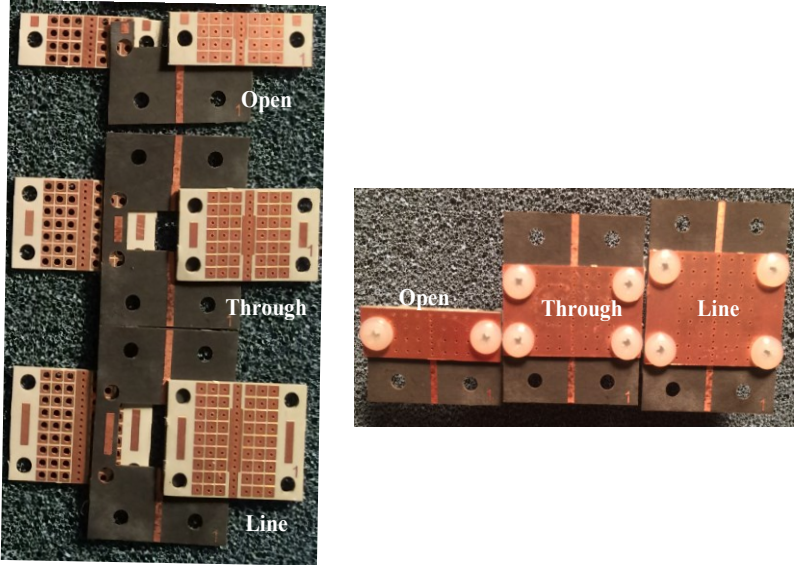


Fig. 2-26. TRL calibration kit for TEM-PRGW with modified cells of Fig. 2-20(a).

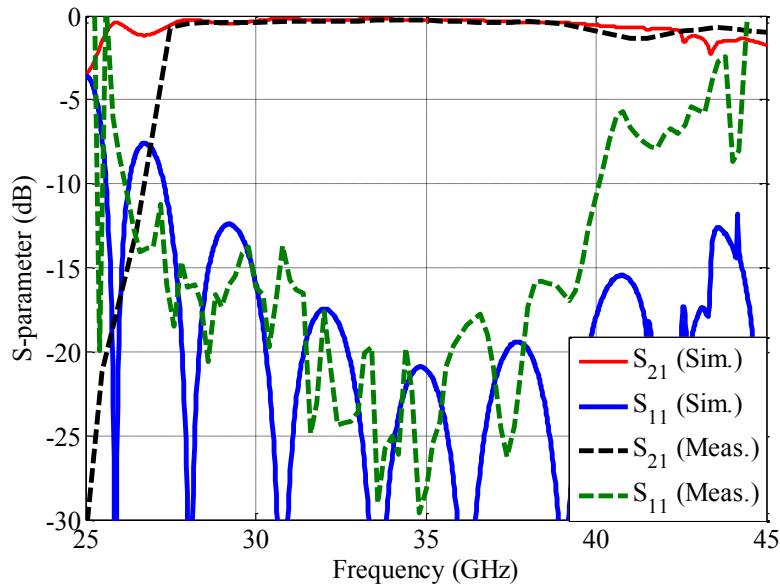


Fig. 2-27. Simulated and measured reflection and transmission coefficient of the TEM-PRGW with modified unit cell of Fig. 2-20(a) with four wavelengths long.

In order to see the effect of the discontinuity in the waveguide performance, a waveguide with double 90-degree bends and with the same overall length of the straight waveguide (L_l) is also investigated. The distributed geometry of the bend line with its fabricated layers is shown in Fig 2-28. In the bend areas, the unit cells of the periodic structure are slightly shifted to be close to the line. In Fig. 2-29 the electric field distribution inside the bent waveguide are shown at different frequencies inside the bandwidth. The performance of the modified unit cells given in Fig. 20 is more pronounced in the discontinuous line because of their superiority in restricting the wave propagations on the ridge by suppressing the other possible modes at the discontinuity regions. As seen from this distribution, the propagation of the waves follows the discontinuous line, and the periodic structure around the line controls any unwanted excitation from the bend regions. The simulated and measured reflection and transmission coefficients of the TEM-PRGW with double 90 degrees bends are shown in Fig. 2-30. As seen from the simulated and measured results, the bend line operates adequately in the desired bandwidth. However, it shows a higher insertion loss in comparison with the straight line.

The geometry of the TEM-PRGW with the second modified unit cell in Fig. 2-20 (b), which has a smaller mushroom on its upper layer size is given in Fig. 2-31 with its fabricated prototype

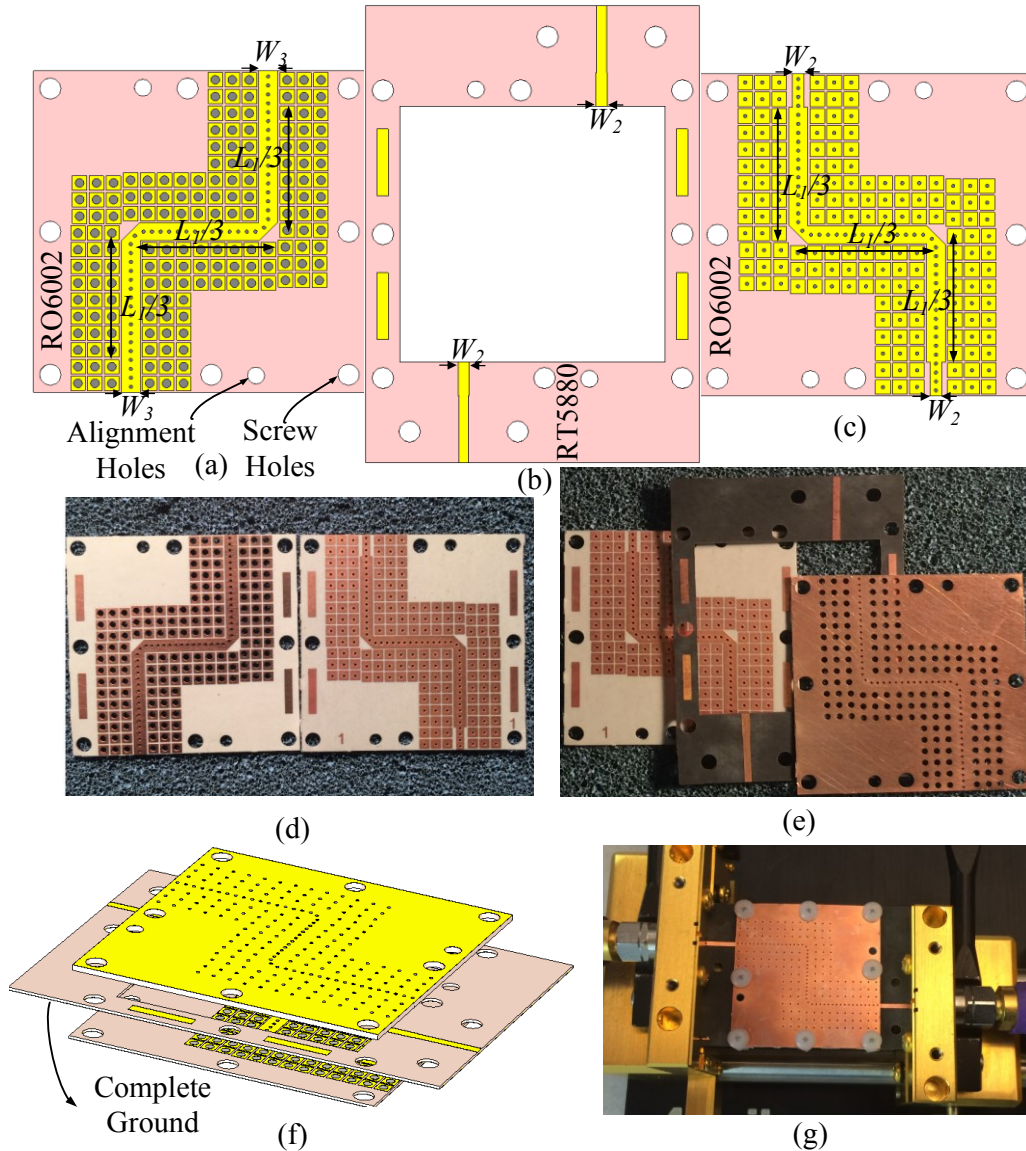


Fig. 2-28. Geometry and fabricated prototype of TEM-PRGW bend line with modified cells of Fig. 2-20(a), (a) Lower thin AMC layer with bend ridge, (b) Middle microstrip feeding layer, (c) Upper thick AMC layer with bend ridge, (d) Fabricated AMC layers with bend ridge, (e) Fabricated bend guide layers with feeding microstrip layers in between (f) 3D view of the stacked layers (g) Assembled layers connected to test fixture probes.

and calibration kit. The same transition from the microstrip line used in the previous waveguide is utilized to feed this waveguide. The two rows of the thin layer, which is the lowest layer in the waveguide geometry, should be covered by the middle layer ground plane. Therefore, there is a high potential for creating a parallel plate region between intermediate layer ground plane and the

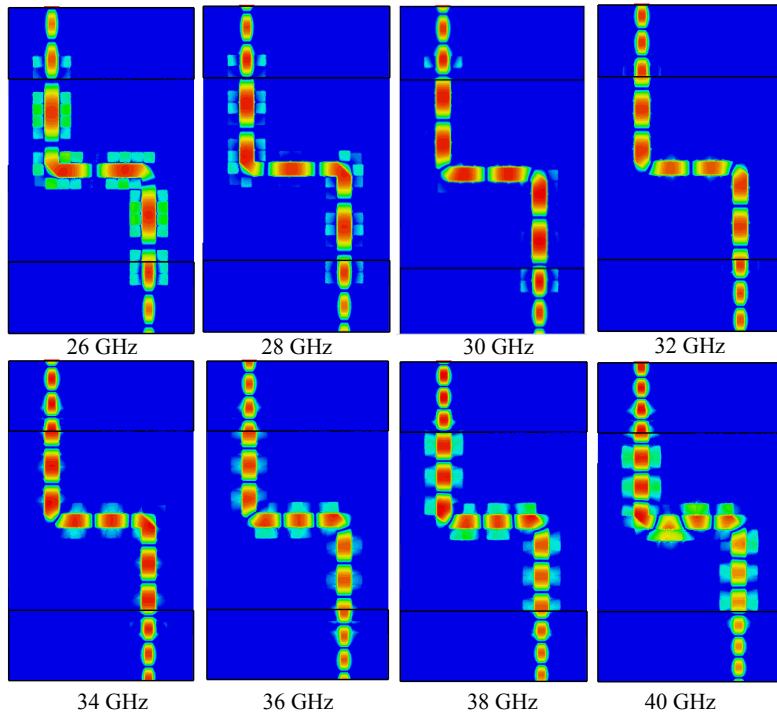


Fig. 2-29. Electric field distribution inside the TEM-PRGW bend line at different frequencies.

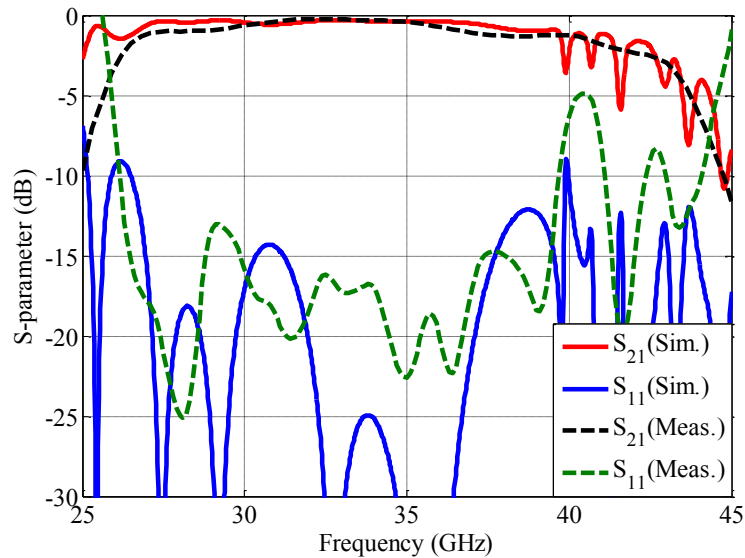


Fig. 2-30. Simulated and measured reflection and transmission coefficients of the TEM-PRGW bend line with modified unit cell of Fig. 2-20(a) with four wavelengths length

lower layer ground plane, which may cause strong leakage of the waves outside the guiding medium. If smaller patches with thin vias are used in these two rows, they would not be able to suppress the leakages from the parallel plate region. Therefore, for the first two rows of the lower

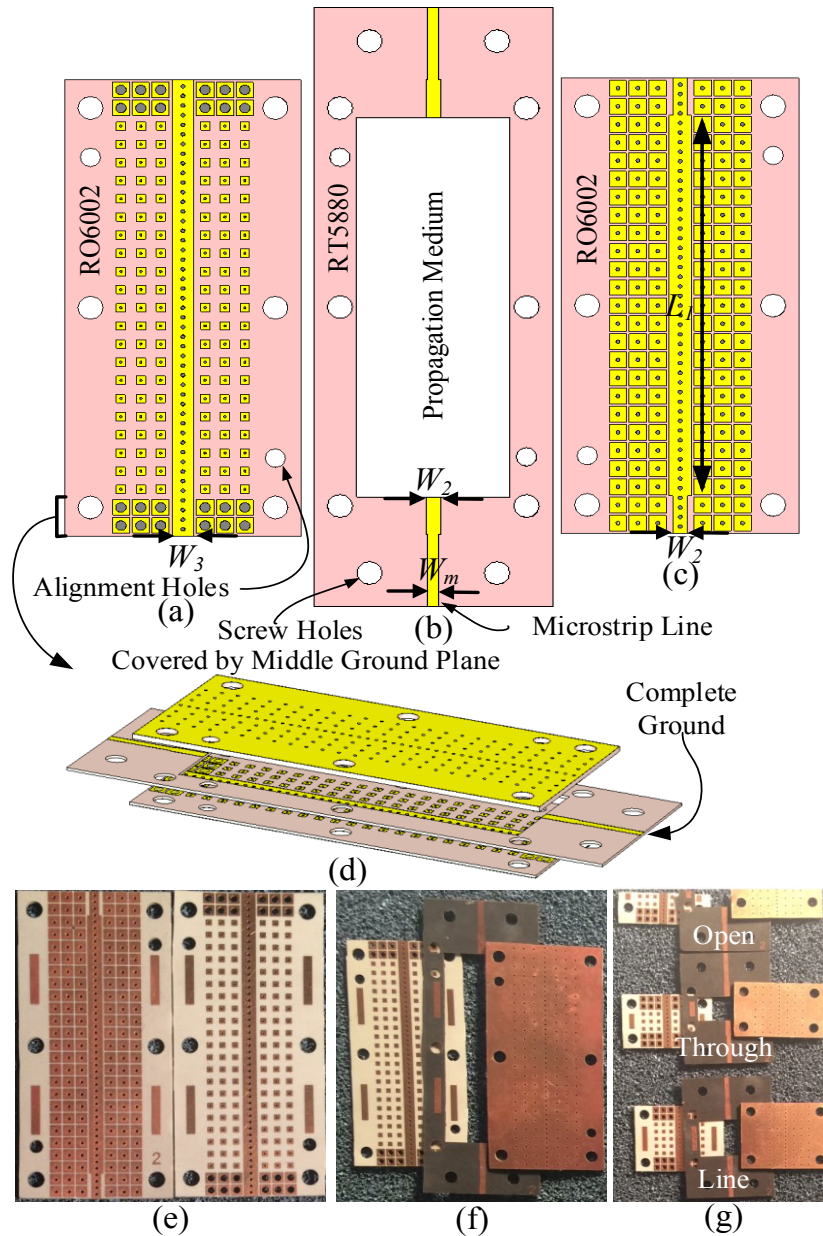


Fig. 2-31. Geometry and fabricated prototype of the TEM-PRGW with modified unit cell of Fig. 2-20(b), (a) Lower thin AMC layer with straight ridge, (b) Middle microstrip feeding layer, (c) Upper thick AMC layer with straight ridge, (d) 3D view of the stacked layers (e) Fabricated AMC layers (f) With feeding layer (g) TLR calibration Kit.

periodic layer, which would be covered by the middle ground plane, wider patches with thicker via holes of the first modified cell are utilized again, as shown in the geometry of the TEM-PRGW in Fig. 2-31. The simulated and measured reflection and transmission coefficient responses of this

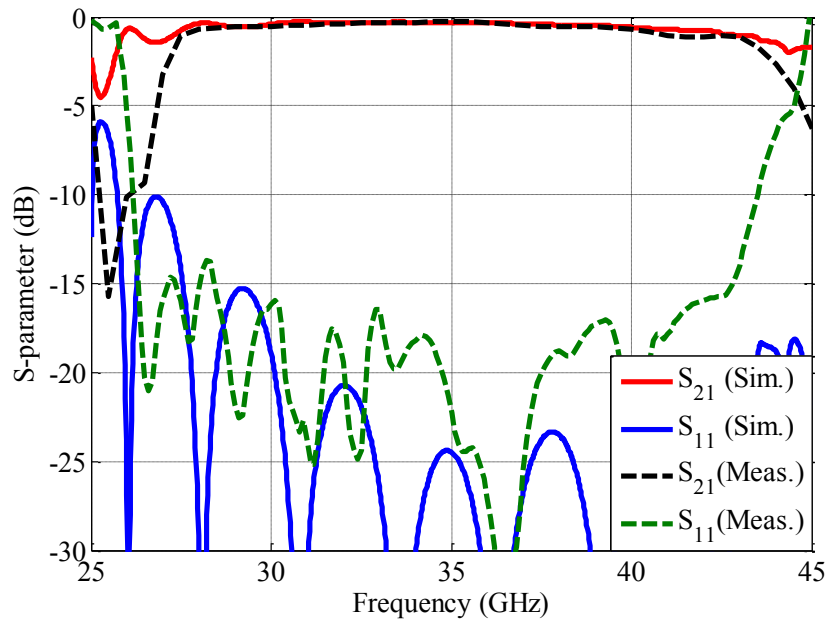


Fig. 2-32. Simulated and measured reflection and transmission coefficient of the TEM-PRGW with modified unit cell of Fig. 2-20(b).

waveguide are plotted in Fig. 2-32. In the middle bandwidth of 30-40 GHz, the measurement and simulation agree with each other as the previous waveguide of Fig. 2-24. However, after 40 GHz this waveguide shows better measured response than the previous one. The geometry of the discontinuous line of this waveguide including two 90° bends is shown in Fig. 2-33. In the first two rows of the periodic structure in the lower layer (thin layer), mushrooms with larger patch and thicker via diameters are used to suppress the wave leakages inside the layer between the overlapped ground planes and between the middle ground plane and patch surface. The scattering parameters of this bent line of the TEM-PRGW are shown in Fig. 2-34. As the straight waveguide, the bend line of this waveguide shows better performance at the end of the band in comparison with the bend line of Fig. 2-28. The measurements of the bend lines are also accomplished using TRL calibration kits utilized for a straight line to shift the reference plane after the transition.

2.6 Conclusion

The new configuration for ridge gap waveguides has been introduced, which enabled the waveguide to support the TEM mode of the propagation instead of quasi-TEM of the single texture

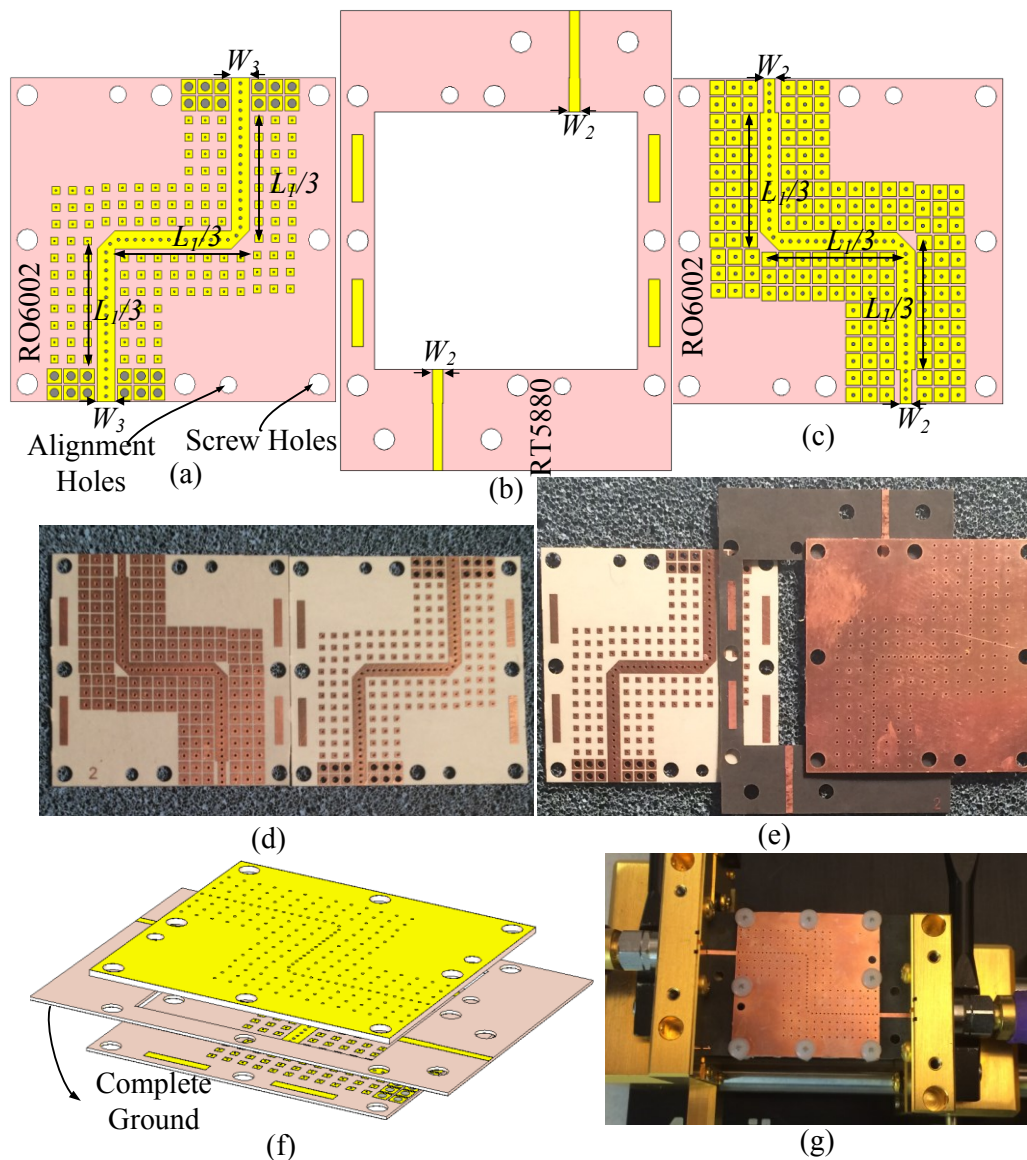


Fig. 2-33. Geometry and fabricated prototype of TEM-PRGW bend line with modified cells of Fig. 2-20(b), (a) Lower thin AMC layer with bend ridge, (b) Middle microstrip feeding layer, (c) Upper thick AMC layer with bend ridge, (d) Fabricated AMC layers with bend ridge, (e) fabricated bend guide layers with feeding microstrip layers in between (f) 3D view of the stacked layers (g) Assembled layers connected to test fixture probes.

of the conventional type. Supporting the TEM propagation has made the RGW behave very close to ideal parallel plate waveguide. As a result, the characteristic impedance of the waveguide lines has been easily extracted from the parallel-plate impedance relation. The horizontally symmetric boundary conditions of the TEM-RGW in the direction of propagation have confined the

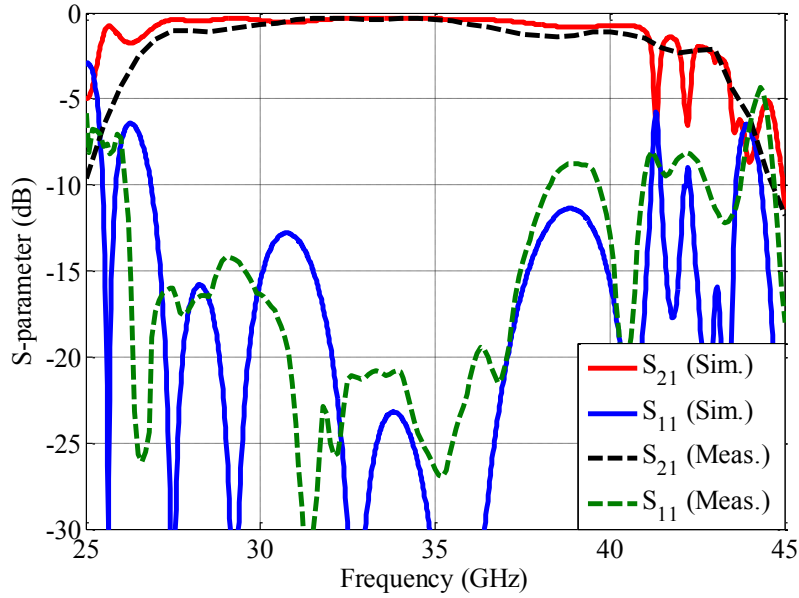


Fig. 2-34. Simulated and measured reflection and transmission coefficient of the bend line of TEM-PRGW with modified unit cell of Fig. 2-20(b) with length of four wavelength.

propagation of the wave on the ridge on both edges of the waveguide. Therefore, the proposed ridge gap waveguide configuration has achieved a lower insertion loss in comparison with conventional gap waveguide with a whole ground plane.

An accurate empirical expression for the characteristic impedance of the proposed TEM-RGW has been presented. Reaching this simple expression for the TEM-RGW impedance has enabled us to define an expression for the characteristic impedance of the quasi-TEM-RGW by considering the TEM-RGW to be equivalent to the regular RGW with half gap height.

The AMC-AMC configuration of the TEM-RGW has been realized by identical mushroom surfaces in the printed version of the RGW, which have been separated by the gap distance. However, since horizontally polarized waves appear in the bandgap of the AMC-AMC parallel-plate periodic structure, the original design of the TEM-RGW has been modified to suppress the undesired polarization that might be excited at a discontinuity. In the modified configuration of the TEM-RGW, asymmetric AMC-AMC parallel plate around the guiding ridges has been utilized to disturb the excitation of the horizontal modes. Therefore, a portion of the ridge modes bandgap has been evacuated from the existence of other possible modes. Two types of new unit cells with

uneven mushrooms have been recommended to produce asymmetric AMC-AMC parallel-plates around the printed ridges. Prototypes of the straight and bent TEM-PRGWs with the modified unit cells have been fabricated, and their performances have been compared with the simulations.

Chapter 3

CONTACTLESS AIR-FILLED SUBSTRATE INTEGRATED WAVEGUIDE

The rapid development of millimeter-wave applications including high-speed wireless data links, short-range radar applications, and high-resolution imaging demands low cost and high performance integrated circuits. As mentioned in Chapter 1, the substrate integrated waveguide (SIW) also known as a post-wall waveguide as a synthetic rectangular waveguide has been a promising technology for implementing compact and low loss millimeter wave devices. In order to get rid of dielectric loss at high frequencies, the air-filled version of SIW has been introduced by removing the dielectric inside the waveguide and covering with the PEC lids to enclose the guiding medium. However, the air-filled configuration of this waveguide requires assured connection of the covering lids to seal the awkward gaps between the layers, which may cause strong leakage, especially at high frequencies. In this chapter, a new configuration of air-filled SIW is introduced that enables the waveguide to be implemented with a cheap connection of the layers without concerning about leaking waves.

3.1 Proposed Configuration of Air-Filled SIW

The geometry of conventional air-filled SIW, which is covered by two other PEC layers is shown in Fig. 3-1(a). For this waveguide realizing the perfect electric contacts between the primary layer and the surrounding plates to form the air-filled waveguide is a challenging task. In fact, any poor contacts of the PEC layers that might leave tiny gaps between them cause a strong leakage of the

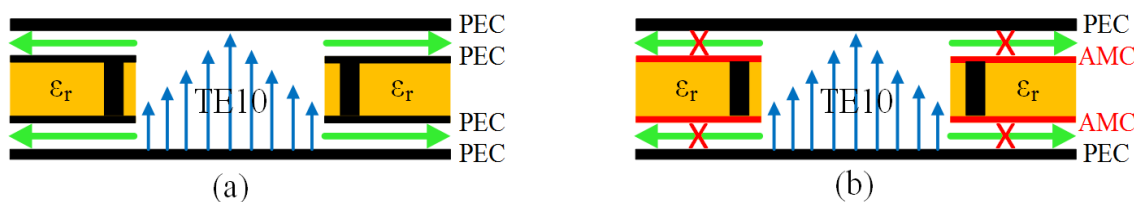


Fig. 3-1. The geometry of (a) Conventional air-filled substrate integrated waveguide (b) Contactless air-filled substrate integrated waveguide.

waves because of the parallel plate mode that has no cutoff frequency. This is a considerable drawback of the air-filled SIW that limits its application, especially in the large scales when there are lots of risks of possible leakages of the propagating waves.

The leakage problem from gaps between meeting PEC layers is solved by introducing a new configuration of the air-filled SIW as shown in Fig. 3-1(b). In the proposed configuration, which takes advantage of PEC-AMC parallel cutoff with any gap of less than quarter of the wavelength, the boundary condition of the substrate solid conductors around the air-filled area is changed to the AMC in the four corners where the covering PEC lids are meeting the middle substrate. Therefore, the parallel plate PEC-AMC regions are created around the guiding medium which provide a cutoff region for parallel plate modes if a gap happens between them.

The concept of PEC-AMC parallel plate cutoff has been utilized in the RGW configuration to confine the propagation of the waves [12]-[14]. However, since the wave is propagating inside the same air-gap height between PEC-AMC layers, the separation of the layers, which is the gap height, should be strictly controlled to keep the bandgap provided by parallel PEC-AMC layers. The operating frequency bandwidth of the waveguide and the components made of the RGW technology is limited to the bandgap of the parallel PEC-AMC plates, which varies with the gap height. In the air-filled SIW, the propagation happens inside the etched regions of the substrate which is fixed with the thickness of the substrate, and the gap happens between the covering lids and the etched main substrate. Therefore, there is no need to control the gap between PEC-AMC layers because the gap intrinsically takes place between the plates that are meeting each other without any additional connection.

Since the bandgap provided by PEC-AMC parallel plate is becoming narrower by increasing the gap between the plates, the minimum possible gap would provide the widest band gap. Hence, the tiny gap created by the overlapping waveguide layers would be helpful to have a wide filtering bandwidth of PEC-AMC parallel plate in this air-filled SIW.

This configuration of air-filled SIW can be called as contactless air-filled SIW because the stopband region created by PEC-AMC formation for any parallel plate mode (TE or TM) does not necessitate the waveguide layers to have complete contact with each other. To evaluate the band

gap performance of the double sided AMC slab with PEC lids, the approximate amount of the possible gap between the stacked waveguide layers has to be measured.

3.2 Gap Estimation Between Overlapping Substrate Layers

According to the studies done by high-frequency circuit laminate manufacturers, such as Rogers, as the signal frequencies increase into the microwave and millimeter wave regions, the contribution of copper foil to the performance of printed circuit boards (PCB) becomes more substantial. This contribution, which mostly comes from the surface irregularities (roughness) of the copper foils, affects both insertion loss and phase constant of the transmission lines in the circuit, as the frequency increases to the extent that the signal skin depth is comparable or smaller than the scale of the conductor roughness [62], [63].

The copper surface roughness also facilitates adhesion to the dielectric during PCB manufacturing. However, the surface roughness of the copper foils of the substrate laminates also contributes in adding gaps between the overlapping substrate layers. For the different Rogers circuit laminates, the copper roughness on the dielectric side and on the top side are given in [64]. The given roughness on the top sides of the copper cladding of the substrates varies between 0.3-1.3 micrometers for different laminates. It can be said that these roughness values are for the microscopic study of the copper cladding of the clean and unprocessed laminates. It has been realized that the fabrication process of the PCB circuit, lots of unwanted scratches have happened on the copper cladding introduced surface roughness. Therefore, in order to reach approximate values for the gaps between stacked layers of the substrates with copper claddings, a prototype is



Fig. 3-2. Measuring the thickness of stacked layers with regular plastic screws to identify possible gap height between them.

made with three stacked substrates which are fixed together tightly with regular and cheap plastic screws. Then, the total thickness of the layers was measured with a digital Vernier caliper, as shown in Fig 3-2, and compared with the nominal total thickness of the different layers. As a result, the possible gap height between the PEC-PEC layers is established as typically $10\mu\text{m} < \text{Gap} < 20\mu\text{m}$.

Such a gap between the PEC-PEC layers is sufficient to cause severe leakages at millimeter wave frequencies. Therefore, regular stacking of the substrate layers would not be efficient for high-frequency applications. For the air-filled SIW designs with PEC-PEC construction methodology, as shown in Fig. 3-1 (a), to be applicable at these frequencies, good contact between the stacked layers is needed, which will be expensive. In contrast, the configuration of air-filled SIW in Fig. 3-1(b) with PEC-AMC parallel plates around the guiding medium would suppress any leakage from this tiny gap. An AMC surface may, for example, be realized with a periodic lattice of unit cells, such as mushroom cells and the obtained gap distance with the PEC layers will be utilized to predict its provided bandgap.

3.3 Unit Cell and Waveguide Configuration of Proposed Air-Filled SIW

After estimating possible gap distance between stacked PCB layers, a variety of unit cells can be designed to realize the AMC surface by considering a PEC layer separated with the gap distance on the top of the cell to provide a bandgap region. In the printed version of ridge gap waveguide, the combination of the parallel PEC-AMC surfaces is realized by a grounded mushroom on a

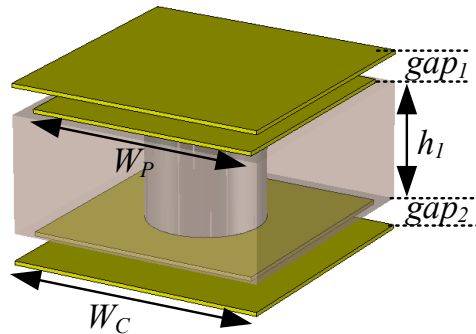


Fig. 3-3. Proposed unit cell for contactless air-filled SIW ($W_P=1.3$, $d=0.8$, $W_C=1.4$, $h_1=0.508$ mm).

substrate separated by an air-gap with upper PEC layers. The grounded mushroom includes a square patch on one side of the substrate which is connected through a metallic via to the complete ground plane on the other side of the substrate. This configuration of the printed mushrooms on a grounded substrate is the conventional method of realizing a high impedance surface (HIS) or AMC surface on one side of the substrate, which has been widely used in different applications such as printed ridge gap waveguide (PRGW) structures. For all of those requests, only one side of the substrate is utilized to deal with and control the propagating waves.

In the proposed configuration of air-filled SIW, the AMC surfaces have to be realized on both sides of the intermediate substrate off the air-filled propagating region, as shown in Fig 3-1(b). In other words, a single substrate should support the realization of AMC surfaces on its both sides. Therefore, the periodic lattice of unit cells should be created on both sides of the substrate surrounding the air-filled region. This cannot be done by the traditional configuration of the mushroom structures. In light of this, the geometry of the mushroom cells has to be modified to make high impedance surfaces on both sides of the single substrate. The proposed configuration of this unit cell with the modified mushroom structure is shown in Fig 3-3. In this configuration of the unit cell, another printed square patch replaces the ground plane. Unlike the traditional

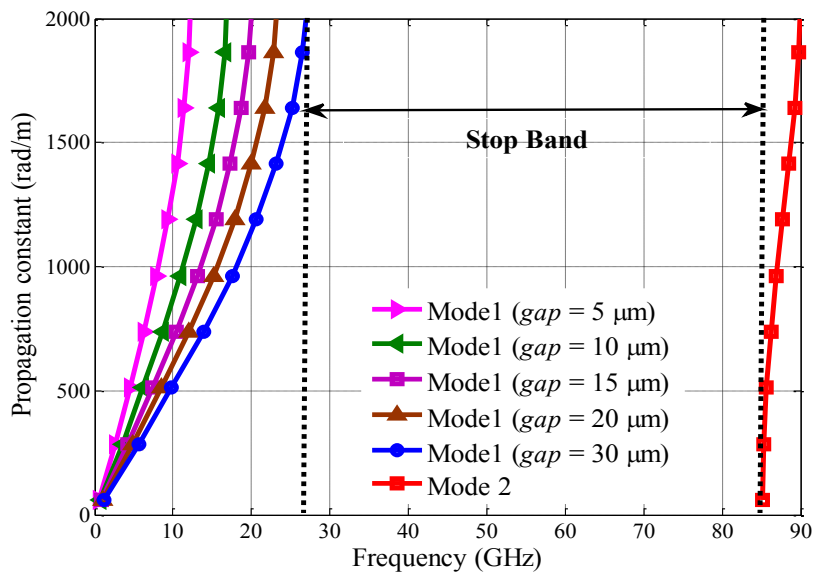


Fig. 3-4. Dispersion diagram of the periodic structure made by proposed cells with different gap size on the both sides.

mushroom unit cell which is horizontally asymmetric, the proposed unit cell has a symmetric configuration. In fact, this is similar to having the mushroom and its image on the other side of the ground plane by removing the ground plane itself. Applying a periodic lattice of this configuration on a single substrate would provide a couple of identical AMC surfaces around the substrate. Covering these AMC surfaces around the substrate with a couple of PEC layers creates a STOP region [65] in any tiny gap which might happen between them. To distinguish the bandgap provided by the combination of a double-side AMC substrate with covering PEC layers, the dispersion relation of the double patch unit cell with a couple of solid PECs on top of each patch with a tiny gap has to be analyzed. As measured before, the amount of this gap could vary from 10 to 20 micrometers on the both sides. If one side of the conducting cover is connected to the patch making perfect electrical contact, the cell would be like a simple mushroom cell, which still operates adequately.

Dispersion diagram of the periodic structure made by this unit cell is shown in Fig. 3-4 for different possible gap heights on the both sides of the substrate. As seen from this diagram, the periodic structure of the given cell provides a wide bandgap for the propagating modes while having a tiny gap between PEC-AMC layers. This bandgap which happens between first and second modes of the dispersion diagram depends on the dimensions of the cell including patch size and via diameter, the periodicity of the cells, and the gap between the square patches and the covering conductor. For the fixed physical dimensions of the cell, changing the possible gap height shifts the lower mode of the dispersion diagram. As seen from the given diagram, by increasing the gap height on the both sides, the first mode moves to higher frequencies and limit the bandgap

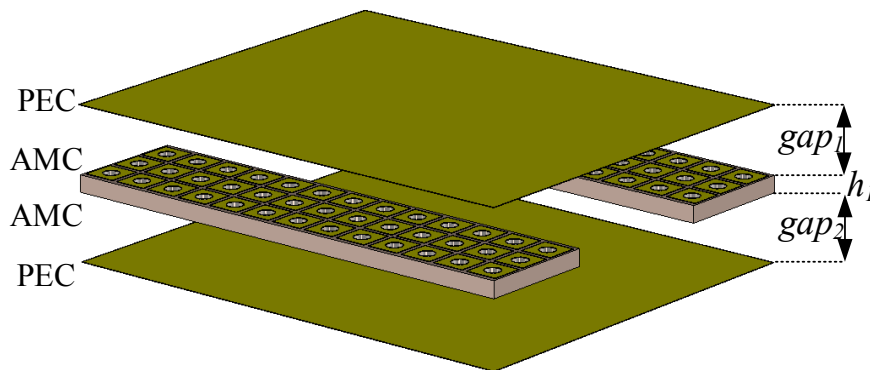


Fig. 3-5. Air-filled SIW configuration with the proposed cells ($gap1=gap2$).

of the periodic structure while the second mode happens at the same frequencies for all gaps. In the best case when the upper and lower conductors are completely connected to the patches, the lower mode disappears, and the upper mode starting frequency varies with the periodicity, and the structure operates like a completely isolated air-filled SIW.

The geometry of the air-filled SIW facilitated with these surfaces around the air-filled guide is given in Fig 3-5. Since the gaps on the both sides of the substrate are not controlled and fixed, they could vary in different circumstances, and they might not be identical; but in the unit cell and the waveguide analysis, they are considered identical on the both sides.

In the normal periodic electromagnetic bandgap mushroom structures, the plated vias with any diameter are used to connect the square patches to the lower ground plane to provide the periodic cells with inductive effect, with a minimum restriction on choosing via diameters. However; for the proposed waveguide configuration, any type of via diameter cannot be selected for the unit cells. Since this waveguide is intrinsically a substrate integrated waveguide, the design of the plated via arrays, including their spacing and diameter, around the guiding medium should satisfy the conventional SIW conditions. For the proposed configuration in which each via around the integrated guiding medium belongs to a single unit cell, the via diameter, and the periodicity of the periodic structure unit cells should meet the conventional SIW design regulations. Therefore,

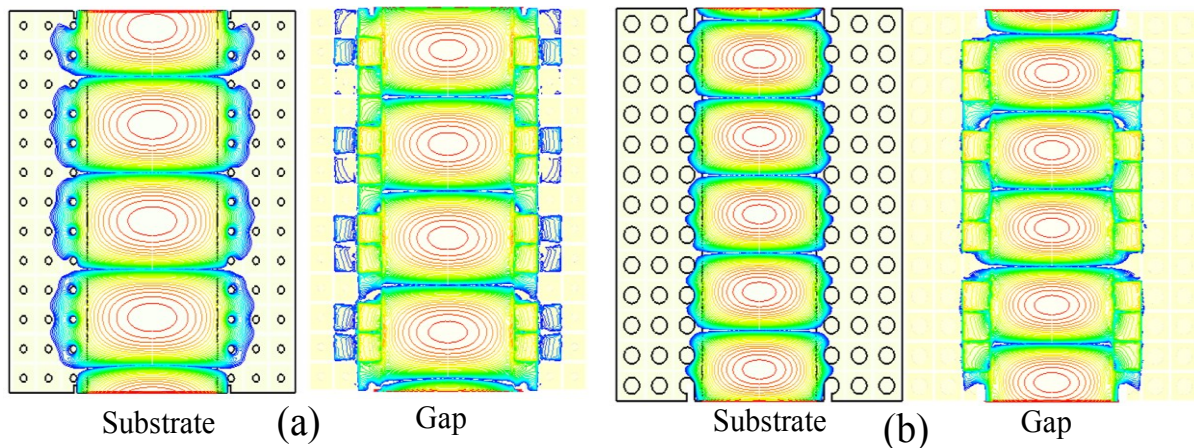


Fig. 3-6. Electric field distribution inside the substrate and in the gap regions of the air-filled integrated waveguide (a) Small via diameter, (b) Via diameter meeting conditions in (3-1).

for an operating frequency with the guiding wavelength of λ_g , the periodicity of the unit cells (p_{Ucell}) and via diameter (d_{via}) has to satisfy the following relations:

$$d_{via} < \frac{\lambda_g}{5} , \quad p_{Ucell} < 2d_{via}. \quad (3-1)$$

The reason that these criteria must be considered in the design of the periodic structure comes from the difference in the application of this periodic structure with the conventional ones. In the conventional periodic mushroom structure operating as AMC surface, the periodic structure is only being excited on its surface, and it is expected to suppress the propagation on the surface. However, the periodic structure utilized in this air-filled waveguide is going to be excited in all three regions, including inside of the substrate and two surfaces around the substrate in which the periodic patches are about to suppress the propagations. Thus, to stop the leakage of the propagating waves inside the substrate the conditions in (3-1) are required. In Fig. 3-6 a comparison is made between two contactless air-filled SIWs with and without considering the conditions of (3-1) and by the fixed 15-micron gap height on the other side of the intermediate substrate with covering layers.

As seen from this comparison, in the waveguide with the larger via diameters there is considerably less leakage inside the substrate. Besides, as the selected frequency is in the band gap of both periodic structures, the AMC surface suppresses the propagation strongly in the gap region after the first row of the cells in the waveguide in which the spacing and via diameter meets the conditions in (3-1).

Selecting the appropriate via diameter for the periodic unit cells that satisfy the given conditions is also a factor to consider against the fabrication limitations enforced by the manufacturer(s) of the SIW which typically define a minimum pad size required at the top of each plated via hole. For instance, based on the available facilities in our laboratories, a minimum annular ring width of 10 mils (0.254 mm) is necessary for each plated via hole and a minimum possible diameter for each via should be equal to half of substrate thickness. Therefore, the minimum patch size for each unit cell would be given as:

$$W_{patch (min)} = d_{via} + 2(d_{pad}) \quad (3-2)$$

where d_{pad} is the minimum distance between the plated via edge and the patch edge.

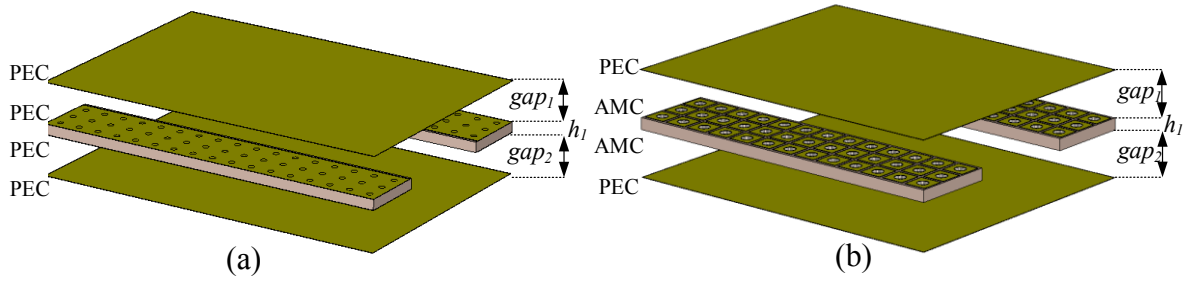


Fig. 3-7. (a) Conventional air-filled SIW, (b) Proposed contactless air-filled SIW, covered by PEC lids with the same gap heights.

3.4 Comparison with the Corresponding Air-Filled SIW

As mentioned, the gap height between the layers mostly determines the existence of the first mode in the unit cell dispersion diagram and the size of the cell affects the second mode frequency, which usually determines the upper limit of the band gap. Therefore, the smallest we select the cell size, the wider the band gap can be expected from PEC-AMC parallel plate around the waveguide. Based on the estimated possible gap that might exist between the intermediate substrate and the covering layers, the performance of the proposed contactless air-filled SIW is compared with the corresponding conventional air-filled SIW. Both waveguides are of the same length, and since the via positioning of the proposed configuration of the waveguide is meeting SIW conditions based on the relations in (3-1), the same vias are repeated for the conventional air-filled SIW, as shown in the Fig. 3-7(a). Therefore, the only difference between two waveguides is the surface of the middle substrate off from the air-filled guiding medium. In the simulation model, an air gap of 15 micrometers is considered between the middle slab and the covering metal lids to be in the range of estimated gap height between the stacked PCB layers. Both waveguides are excited with the ideal wave ports provided by the simulator, and the backside of the ports are attached to an absorbing boundary condition. The simulation is performed under completely identical conditions, and the only difference between the models is the texture of the conductor on the middle substrate. The simulated transmission coefficients of the waveguides are compared in Fig. 3-8. The air-filled SIW with solid conductor surface results in much higher insertion loss in comparison with the

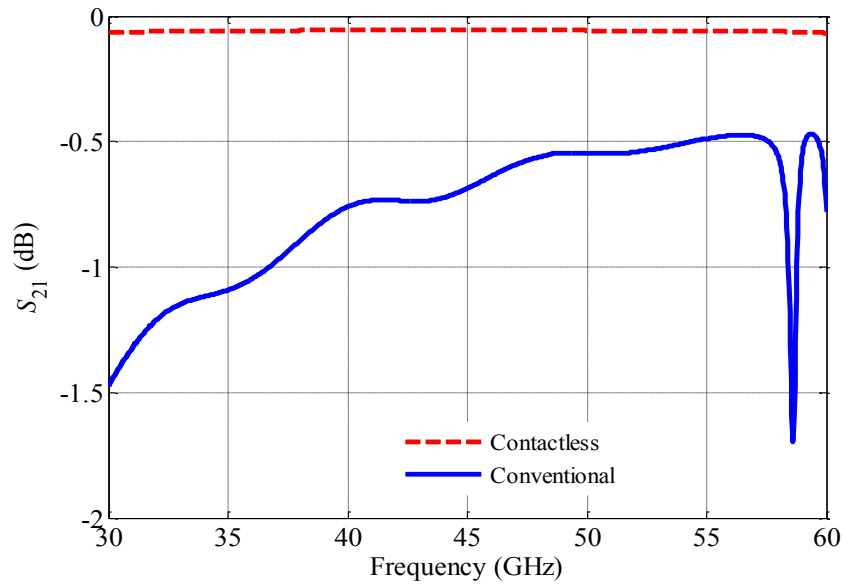


Fig. 3-8. Simulated transmission coefficient comparison between the conventional and contactless air-filled SIW.

waveguide with the textured surfaces. The electric field distribution inside the 15 μm gap height and inside the substrate of both waveguides at 40 GHz are shown in Fig 3-9. It is clear from this illustration that there is a strong propagation of leaking waves in the tiny gap between the PEC layers of the air-filled SIW which cause considerable losses along the propagation. However, the air-filled SIW with the textured surfaces around the guiding medium suppresses the leakage of the waves in the gaps with the PEC lids and controls the wave to propagate inside the waveguide. Therefore, a considerable reduction in insertion loss is obtained for this waveguide showing that

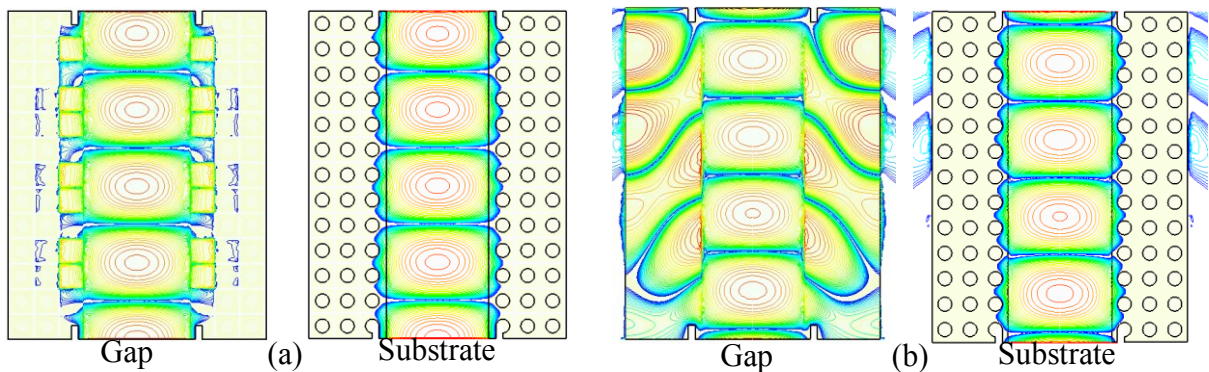


Fig. 3-9. Electric field distribution inside the substrate and the air-gap of (a) Proposed contactless air-filled SIW with textured surface off the guiding medium (b) Simple air-filled SIW with solid conductor off the guiding medium.

the proposed air-filled SIW is not sensitive to the electrical contacts of the upper and lower covering lids with the intermediate substrate and still preserves a low loss propagation.

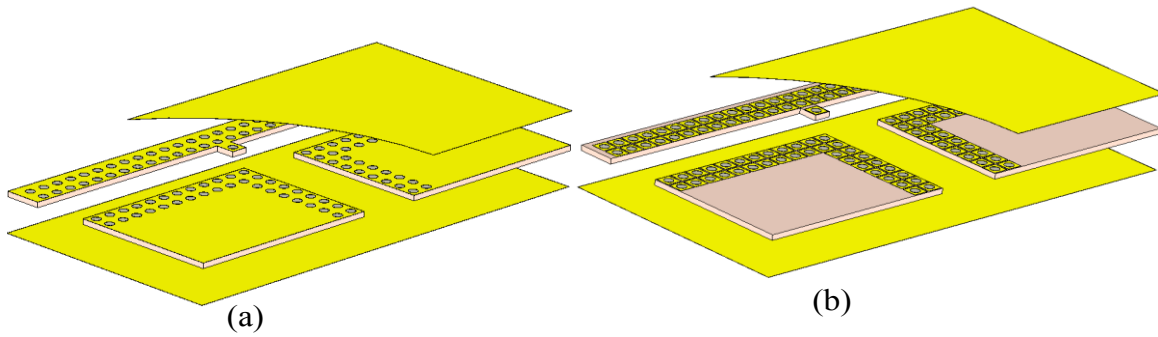


Fig. 3-10. Geometry of air-filled SIW T-junctions (a) Conventional (b) Contactless.

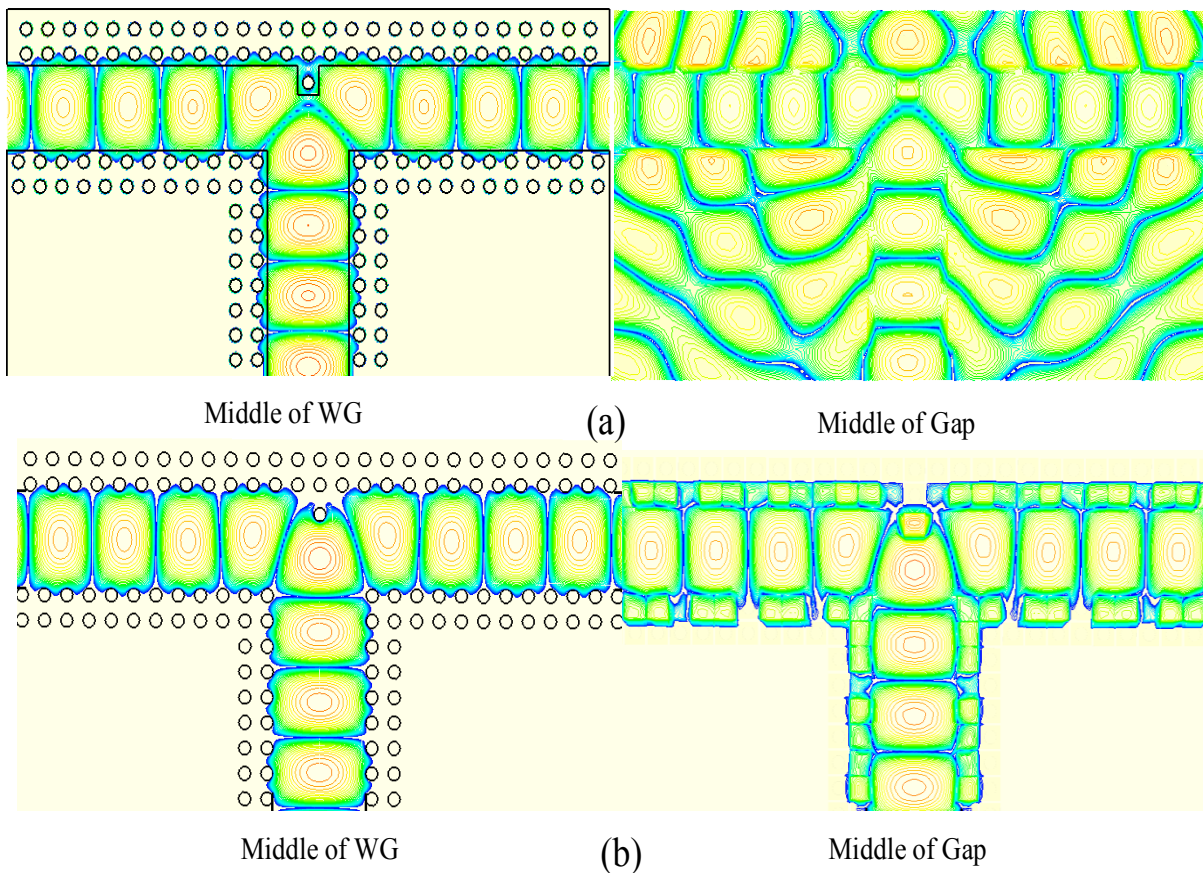


Fig. 3-11. Electric field distribution of air-filled SIW T-junctions (a) Conventional (b) Contactless.

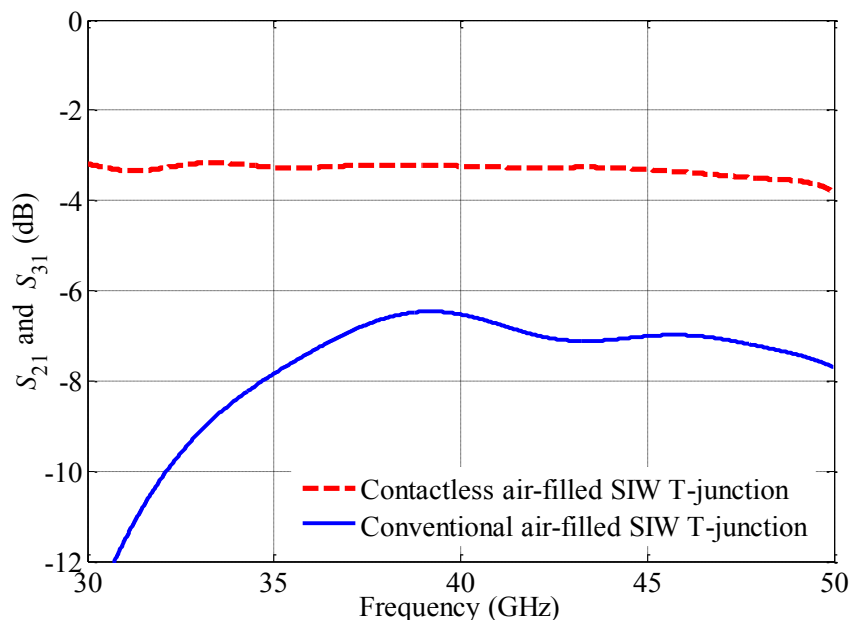


Fig. 3-12. Simulated transmission coefficient comparison of the conventional and contactless air-filled SIW T-junctions.

The same comparison is also made for an air-filled SIW T-junction between the conventional structure and present configuration. The geometry of air-filled SIW T-junctions is shown in Fig. 3-10. Both junctions are fed with an ideal wave ports by considering a gap of 15 μm between the covering lids and the intermediate layer. The electric field distribution in the air-filled substrate and inside the gap of both T-junctions are shown in Fig. 3-11 at 40 GHz. Inside the air-filled region, the field distributions of both junctions are identical. However, inside the tiny gap with the covering lids, the waves are leaking outside the junction in the conventional type while they are suppressed in the proposed contactless configuration. The transmission coefficients of the T-junctions are compared in Fig. 3-12. Obviously, the leakage from the tiny air gap in the conventional air-filled SIW has caused a considerable difference in the insertion loss of the T-junctions.

3.5 Transition to Standard Feeding Line

As mentioned, the waveguides in Fig. 3-7 are excited by the wave ports provided by the simulator. In order to feed the proposed air-filled waveguide with standard transmission lines for possible

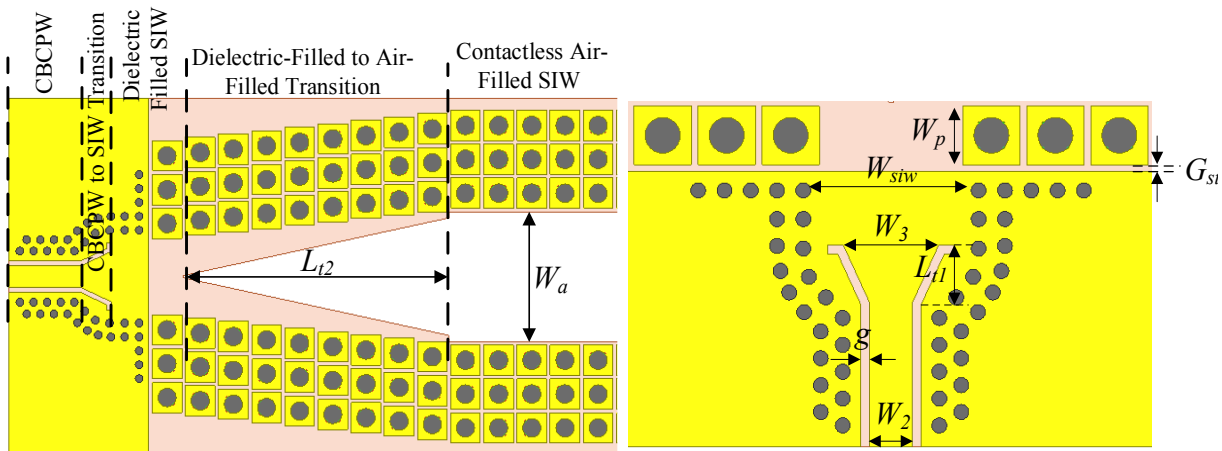


Fig. 3-13. Transition segments from CBCPW to contactless air-filled SIW.

connections to commercial connectors, a transition has to be applied to make an effective interconnect between the proposed air-filled waveguide and the other standard transmission lines. Here, the transition is designed to connect the proposed air-filled waveguide to the grounded coplanar waveguide with a 50-Ohm characteristic impedance, which can easily connect to the end-launch connectors that are widely accepted by measurement instruments. The standard conductor backed coplanar waveguide (CBCPW) can only be implemented on the dielectric slab, and a transition is needed to connect it to the dielectric filled SIW. The CBCPW to SIW transition, which has been widely used for most of the substrate integrated circuits, usually ends up with tapering of the CPW cuts to reach the corners of the SIW. However, the design should be modified for the desired frequency band and the waveguide dimensions. Therefore, transitions from the air-filled SIW to the conventional dielectric-filled SIW and from SIW to the CBCPW are required. The geometry of the transitions is given in Fig. 3-13.

The sections of this transition are all implemented on the intermediate substrate. The periodic structure around the air-filled waveguide continued until the end of the first transition from air-filled to the dielectric-filled waveguide and extended as one cell inside dielectric-filled waveguide to pass all air-cut medium. Therefore, the upper and lower conductors in Fig. 3-7, which cover the whole air-filled areas and the periodic structure should be extended till almost the middle of the dielectric filled waveguide. At the end of the contactless environment, the entire ground planes on either side of the substrate starts and continues to the end of the substrate. The vias diameter for

the rest of the transition is selected to be small by considering SIW conditions. The SIW to conductor-backed CPW (CBCPW) transition is designed for the middle frequency of 40 GHz. The backing plated vias of the transition should be carefully placed to narrow down the width of the SIW similar to the tapered etched transition on the conductor to conveniently convert the TE_{10} mode of SIW to quasi-TEM mode of CBCPW line. These vias are continued around the CBCPW line to suppress any possible parallel plate modes between upper and lower conductors of the intermediate substrate. The width of the line (W_2) is chosen to provide a 50Ω characteristic impedance to be matched with the standard connectors. The overall view of the contactless air-filled waveguide with transitions covered by a couple of grounded layers is given in Fig. 3-14. The length of the transition from the air-filled SIW to the dielectric-filled SIW can also be increased to reach better insertion loss of the transition. However, in this design, the whole length of the line cannot exceed a certain amount to be able to measure the line performance with the available test fixture. The effect of the transitions in the measured insertion loss can be canceled by utilizing a TRL calibration kit.

At the contact point of the covering lids and the solid conductor of the intermediate substrate in the middle of the dielectric-filled SIW, two solid PEC layers are meeting each other where the existence of the gap would cause leakage toward the transition. In order to minimize the leakage from this part of the transition, the length of the overlapping section can be kept as short as possible, and after fixing the layer, a small amount of conductive glue can be added here. The other

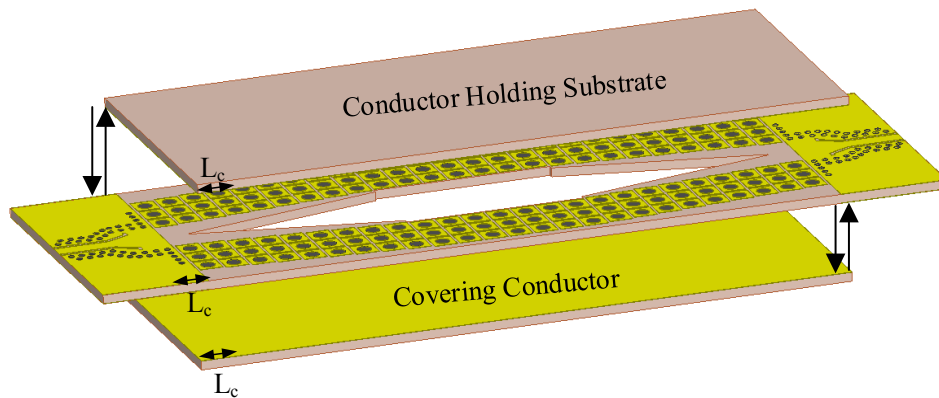


Fig. 3-14. The whole configuration of contactless air-filled SIW with transitions.

way that may decrease the wave leakage outside the waveguide is to extend the overlapping section (L_c) as a quarter of a wavelength at the middle frequency of waveguide so that the leaking waves would see short circuit at the end of the opening. It should be stated that the covering layers of the air-filled medium and the partially air-filled transition in Fig. 3-14 can be selected from any type of low cost substrates that are just holding the covering conductors around the waveguide.

3.6 Experimental Evaluation

As mentioned in the first section, the contactless air-filled SIW is proposed to solve the contact problem associated with the conventional air-filled SIWs. The conventional air-filled SIWs necessitates very strict connection of the covering layers to control the leakage of a propagating wave to reach an acceptable insertion loss of the waveguide. Therefore, the simple and cheap connection of the waveguide layers such as regular stacking and screwing substrate layers would destroy the waveguide performance because of the possibility having tiny gaps between the layers; but the new configuration of the air-filled SIW is supposed to operate adequately with the simple connection of the layers. To demonstrate practically the superiority of proposed waveguide, its performance should be compared to the simple air-filled SIW. In light of this, two prototypes of the air-filled SIW are made with the same length and via positioning in the intermediate layer as shown in Fig. 3-15. Both waveguides are excited with the 50Ω CBCPW transmission line which connected to the waveguides with identical CBCPW to SIW transitions. After the transition from CBCPW line, the continuous copper cladding of the dielectric-filled SIW is removed to begin the multi-layer section of the waveguide where the covering PEC lids are becoming to sandwich the middle substrate and cover the air-filled region. As the intermediate substrate should be partially cut in the transition from dielectric-filled SIW to air-filled SIW, the covering PEC lids must cover this section of the transition. Therefore, from the feed point of the CBCPW line until the middle of the dielectric-filled SIW, where the continuous conductor of the substrate stops, both prototypes are identical. After this point, the only difference in the waveguides is on the surface of the intermediate substrate around the guiding region, which is textured with periodic square patches for the proposed waveguide, and it is the continuous conductor for the conventional type. The propagating wave along these air-filled SIWs is dealing with three regions, including the

intermediate region inside the substrate and the upper and lower contact regions with the possible gaps. In the middle region, both waveguides are supposed to operate the same, as the plated vias are in the identical positions forming a waveguide with the same characteristics. The difference in the performance comparison will only come from the differences in the upper and lower layers connections with the intermediate substrate.

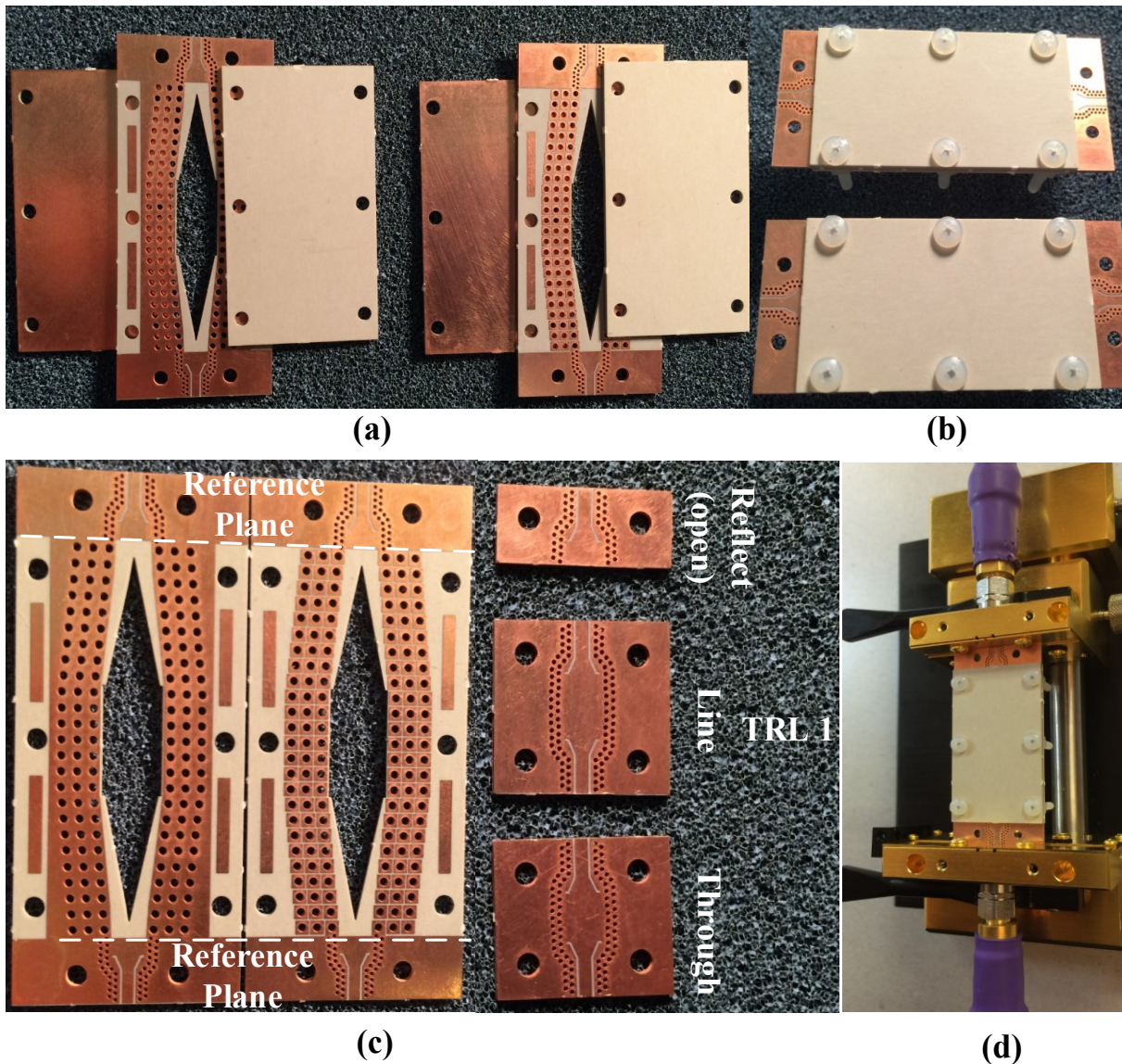


Fig. 3-15. (a) Simple and contact less air-filled integrated waveguides with covering lids (b) Stacked layers fastened with plastic screws (c) TRL calibration kit and moved reference plane location of the air-filled waveguides (d) Exciting the air-filled SIWs with test fixture.

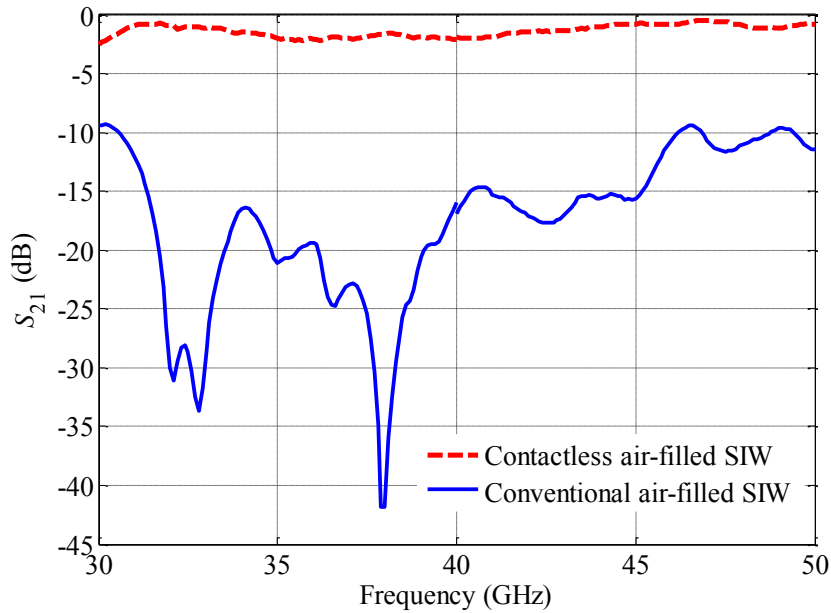


Fig. 3-16. Measured transmission coefficient comparison between contactless and simple air-filled SIW.

The upper and lower layers are selected from any available and relatively thick substrates to hold the solid and firm PEC lids for the waveguide. The layers of the waveguides are stacked and fixed with 6 plastic screws with almost the same pressure of the layers to have a fair comparison, as shown in Fig. 3-15(b). After assembling layers, both waveguides are looking identical in all dimensions. To exclude the losses coming from the CBCPW transmission line and CBCPW to SIW transition, a Through Reflection Load (TRL) calibration kit is prepared to remove the reference plane from the exciting port to the starting point of the contact region with covering lids in the middle of dielectric-filled SIW, as shown in Fig. 3-15(c). The S -parameters of the assembled waveguides are measured using the PNA. In Fig. 3-15(c) the air-filled SIW is launched by test fixture which is connected to the PNA cables. The measured insertion loss comparison of the contactless and regular air-filled SIWs are shown in Fig. 3-16. The considerable difference between the insertion losses of the two same-length air-filled SIWs is evident. The proposed contactless air-filled integrated waveguide with periodic structure shows a much lower loss with the bandwidth of the cheap connection of the covering lids. This is because the periodic structure around the guiding medium is suppressing leaking waves from the tiny gaps of the covering layers. However, the leaking waves easily propagate outside the guiding medium in the regular air-filled

SIW. This can be seen by monitoring the variation of the scattering parameters on PNA in the measurement process when a metallic object is becoming close the air-filled waveguide under test. In fact, at this frequency band realizing the genuine connection between the contacting layers is very expensive and demands high accuracy in the fabrication process. Therefore, utilizing the proposed configuration for the air-filled integrated waveguides are more advantageous and cost-effective.

As mentioned, in this measurement the reference plane of the waveguides is moved from the excitation port to the middle of dielectric-filled SIW where the covering PEC lids are meeting the waveguide. This means that the loss effects of the second transition section, which is dielectric- to air-filled SIW transition, and the discontinuity in the layers contact region are included in the measured insertion loss of the waveguides. Therefore, a significant portion of the insertion loss of the proposed contactless air-filled SIW comes from these sources.

To remove the losses coming from the second part of the transition and the contact section of the covering layers with the intermediate substrate, the reference plane should be moved to the end of the transition where the complete air-filled waveguide starts. To do this, another TRL calibration

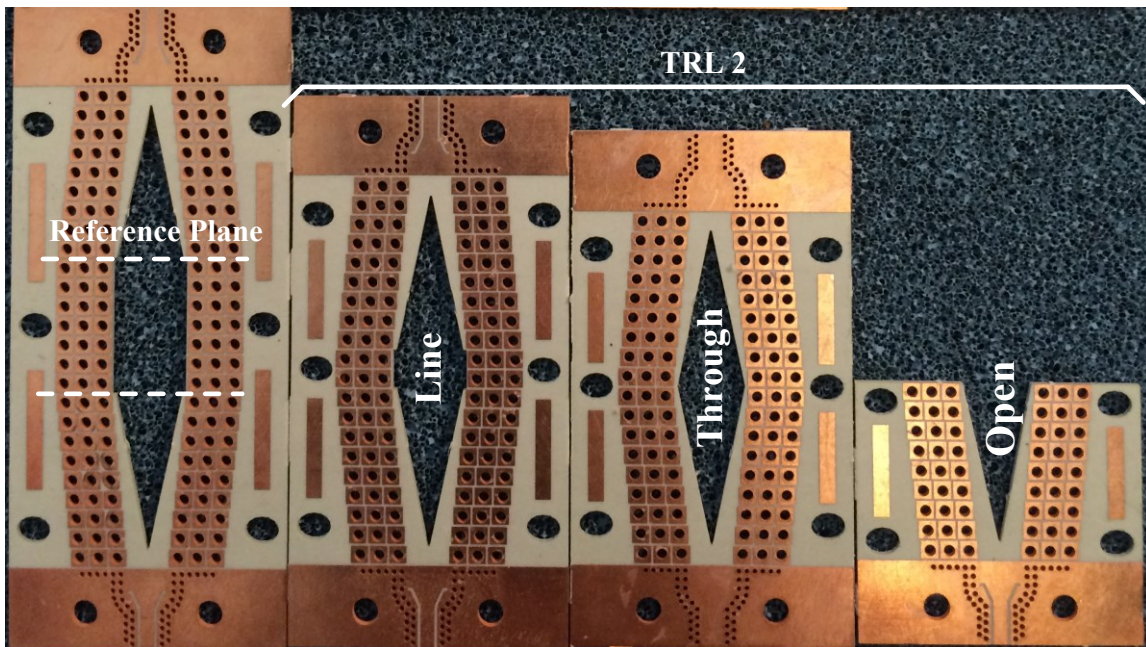


Fig. 3-17. Contactless air-filled SIW with the second TRL calibration kit.

kit is prepared and fabricated for the contactless air-filled SIW, as shown in Fig. 3-17. Measured transmission coefficient of the proposed contactless air-filled SIW, with the reference planes, shifted to end of the transitions using a second TRL calibration kit, is compared in Fig. 3-18 with the first measurement, in which the reference planes are in the contact region of the covering lids. As expected, the measured losses in the middle section of the waveguide are much less than the whole waveguide including transitions. Comparing with the simulated transmission coefficient of this waveguide in Fig 3-8, lots of fluctuations appeared in the measured transmission coefficient of the contactless air-filled SIW. This might be because of the uneven gap between the covering PEC lids and the intermediate substrate. In the simulated model, the gap distance between the intermediate substrate and the covering lids is fixed on both sides, and the waveguide is excited with ideal wave ports. However, in the fabricated prototypes, this gap is accidental and might vary along the waveguide. It should also be said that the test fixture used in the measurements has a limited frequency range till 50 GHz which could be another reason for high losses at upper end of the band after applying TRL calibration.

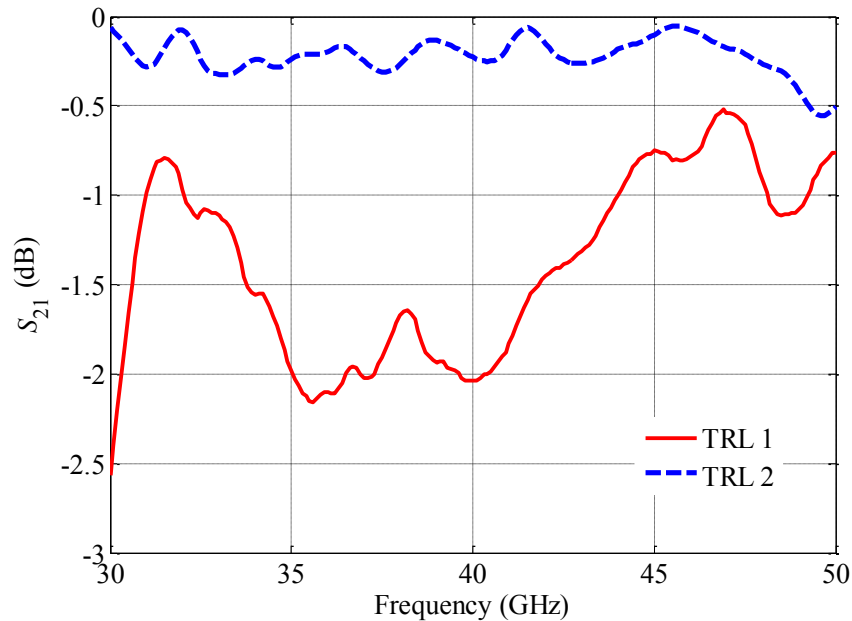


Fig. 3-18. Measured transmission coefficient of contactless air-filled SIW with different reference planes moved by TRL kits.

One of the loss sources of the contactless air-filled SIW with transitions is the imperfect contact point of the covering lids with the air-filled substrate in the middle of the transition, which is not isolated unlike the lateral sides of the contactless air-filled SIW. In the next chapter, a new configuration of the conductor-backed CPW is introduced which can be utilized to launch the air-filled SIW directly with an air-filled planar transmission line. Therefore, the effects of dielectric-filled with air-filled transition can be removed from the waveguide excitation. Besides, as the exciting feed line is supporting air propagation and needs to be covered with another substrate layer, the covering layer can be extended whole over the waveguide to avoid having any discontinuity of the layers.

3.7 Conclusion

The new configuration for air-filled SIW has been introduced, which is not sensitive for the leakages from the cheap connection of the covering layers. In the proposed SIW structure, the complete conductors of the substrate cut region are replaced with the AMC surfaces realized by periodic structure. These AMC surfaces with the upper conductor lids make a cutoff region in the tiny gaps happening between the layers for any leakage of the waves. Therefore, the etched middle substrate, which supports the air-filled medium of the propagation, can be stacked with covering grounded layers using any cheap type connections. The performance of the proposed configuration of the air-filled SIW is compared with the simple air-filled integrated waveguide of the same length and same via the positioning of the middle layer. Both simulation and measurement results have shown a considerable difference in the insertion loss of the waveguides. As the covering lids are fixed to the main layer with plastic screws for both waveguides, at the millimeter wave frequencies, the proposed contactless waveguide shows substantially lower loss than the conventional air-filled SIW.

Chapter 4

PARTIALLY AIR-FILLED CONDUCTOR-BACKED COPLANAR WAVEGUIDE

Microstrip and coplanar waveguide formats have been chosen over other high-frequency transmission lines, such as strip line, due to their simplicity in the fabrication and accessibility of the signal layer for component mounting. The conductor-backed coplanar waveguide (CBCPW) has received considerable attention in conjunction with the microstrip line in microwave circuit designs. The ground layers of CBCPW are connected to each other via metallic vias to suppress the substrate waves. Therefore, the CBCPW line requires three times less lateral space than the microstrip line, as both are carrying the quasi-TEM wave mode. Although CBCPW lines are suffering from higher conductor loss in comparison with microstrip and coplanar launched microstrip lines, its loss follows as almost constant slope over a wide frequency range than others. In other words, at higher frequencies, microstrip and CPW lines exhibit considerable radiation loss than CBCPW line. Therefore, using proper design techniques and via spacing, CBCPW circuits can be fabricated with minimum radiation loss and a wider range of impedance than microstrip circuits [66]-[69].

For the dielectric filled CBCPW to be less depressive, the signal line should be tightly coupled to the ground on the coplanar layer, since the electric-field mostly concentrates in the air so that the effective inhomogeneity of wave traveling medium would be reduced. Here, a new configuration of CBCPW is introduced which support wave propagation mostly in the air medium resulting in considerable reduction in the dispersion. In this configuration, tight coupling between the signal line and lateral grounds would not be necessary for diminishing the line dispersion.

4.1 Air-Filled CBCPW Configuration

The geometry of the proposed structure of air-filled CBCPW is illustrated in Fig. 4-1(a). The structure is based on multilayer PCB process, which contains three layers of the same substrate

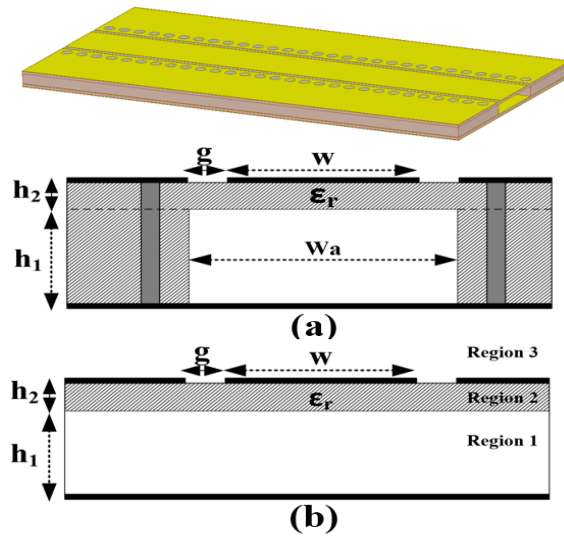


Fig. 4-1. The geometry of air-filled CBCPW (a) Simulated model (b) Model used for quasi-static analysis.

type of RO6002. The middle layer is chosen to be a thicker than the others without any metal plates and is depleted in the central part to support propagation in the air medium. On the upper side of the top layer, a microstrip line with a couple of coplanar grounds is printed with a gap between them representing CPW configuration. This layer is selected to be as thin as possible because its main function is holding the signal line and the coplanar grounds. The lower layer is also keeping the back conductor of the CPW, and it could be from any low-cost type substrates used in the baseband or digital circuits. Reportedly, adding conductor on the back of coplanar launched a microstrip line causes unexplained high losses and visible resonances in the form of parallel-plate waveguide modes, resonant patch mode, or coupled slot-line mode. Therefore, a shorting technique using metallized via holes should be applied between two lateral grounds and backed conductor to suppress to some extent the unwanted modes, as shown in Fig. 4-1(a).

The width of the area filled with air in the middle layer of this CBCPW structure is equal to the width of the signal line in addition to its lateral gaps on the top layer. In this structure, the wave propagation medium is a combination of air and dielectric substrate, but the air volume is more considerable than the dielectric volume. Therefore, the effective dielectric constant of this CBCPW line is close to unity than dielectric filled CBCPW. Considering this, the width of signal line and lateral the gap size have to be modified to achieve a 50Ω line.

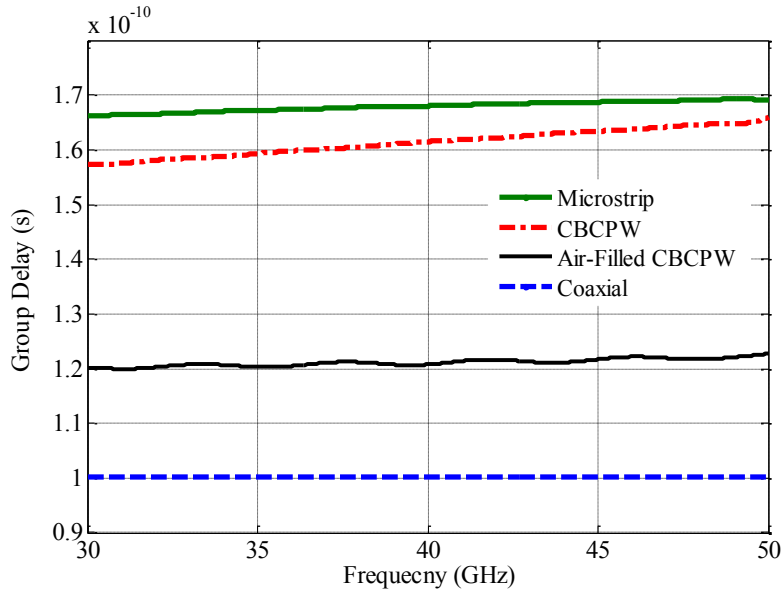


Fig. 4-2. Group delay response comparison of air-filled CBCPW with other three lines.

The group delay response of the proposed air-filled CBCPW in comparison with microstrip line, dielectric-filled CBCPW, and coaxial line with same line length are illustrated in Fig. 4-2. It is shown that the group delay variation of proposed air-filled CBCPW is much close to the coaxial line group delay response compared to the microstrip line and dielectric-filled CBCPW, which is an indication of being less dispersive than other planar lines.

4.2 Quasi-Static Analysis of Air-Filled CBCPW Based on Conformal Mapping

To design the proposed line for particular characteristic impedance, an approximate expression is obtained considering the simplified geometry shown in Fig. 4-1(b). The conformal mapping is utilized with zero conducting thickness. The basic approach used in conformal transformation method is to replace all dielectric interfaces in the structure, including slots, by magnetic walls [70], especially for structures that the electric field lies along the dielectric interfaces. Since we are dealing with the quasi-static approximation of the mode of propagation, the general value of characteristic impedance can be expressed as [71]:

$$Z_0 = \frac{1}{c_0 \sqrt{\epsilon_{reff}} C^a} \quad (4-3)$$

where c_0 is the velocity of the wave in free space and C^a is the total capacitance per unit length of the coplanar line by considering air as the dielectric. Using conformal transformation applied for multilayer CPW in [71] the effective dielectric constant for the proposed air-filled conductor-backed CPW can be written as:

$$\varepsilon_{reff} = q_1 + q_2\varepsilon_r + q_3 \quad (4-4)$$

where q_1 , q_2 , and q_3 are the filling factors related to the air-filled area under the line, the thin dielectric holding the line, and the free space above area up the line. The filling factor for each area is defined as the ratio of the capacitance of each layer (C_{si}^a) to the capacitance of whole coplanar structure (C^a) by considering air as a dielectric for all layers as:

$$q_i = \frac{C_{si}^a}{C^a} \quad (4-5)$$

The total capacitance of the C^a can be divided into two portions, one due to upper half-plane above CPW metallization (C_1^a) and the other is due to the area between the ground plane and the CPW metallization (C_2^a) considering air as the substrate. Therefore, the filling factor for each region of Fig. 4-1(b) can be written as:

$$q_1 = \frac{C_2^a - C_{s2}^a}{C^a}, \quad q_2 = \frac{C_{s2}^a}{C^a}, \quad q_3 = \frac{C_{s3}^a}{C^a} \quad (4-6)$$

As the region 1 is away from signal line, its filling factor is calculated based on the feeling factors of the regions close to the signal line. This is because the values related to the capacitances are obtained using conformal transformation which can only be applied for the areas in the vicinity of the signal line.

The arguments of elliptical integrals used for conformal transformations for this line are defined as:

$$k_0 = \frac{w}{w + 2g} \quad (4-7)$$

$$k_1 = \frac{\tanh(\pi w/4(h_1 + h_2))}{\tanh(\pi(w + 2g)/4(h_1 + h_2))} \quad (4-8)$$

$$k_2 = \frac{\sinh(\pi w/4h_2)}{\sinh(\pi(w+2g)/4h_2)} \quad (4-9)$$

An accurate but simple expression of ratio K/K' is available in [72] and is included here:

$$\frac{K(k_i)}{K'(k_i)} = \frac{\pi}{\ln[2(1+\sqrt{k'_i})/(1-\sqrt{k'_i})]} \quad 0 \leq k_i \leq 0.707 \quad (4-10)$$

$$\frac{K(k_i)}{K'(k_i)} = \frac{1}{\pi} \ln[2(1+\sqrt{k_i})/(1-\sqrt{k_i})] \quad 0.707 \leq k_i \leq 1 \quad (4-11)$$

where $k'_i = \sqrt{1 - k_i^2}$.

Based on the explanations given in [71] for the conformal transformation of CPW lines, the capacitances used for the filling factor calculations are:

$$C^a = C_1^a + C_2^a = 2\varepsilon_0 \frac{K(k_0)}{K'(k_0)} + 2\varepsilon_0 \frac{K(k_1)}{K'(k_1)} \quad (4-12)$$

$$C_{s2}^a = 2\varepsilon_0 \frac{K(k_2)}{K'(k_2)} \quad (4-13)$$

$$C_{s3}^a = 2\varepsilon_0 \frac{K(k_0)}{K'(k_0)} \quad (4-14)$$

Having the filling factor related to each part of the line, the effective dielectric constant could be calculated using (4-4), then the characteristic impedance of the line can be obtained by (4-3) as follows:

$$Z_0 = \frac{60\pi}{\sqrt{\varepsilon_{reff}}} \frac{1}{\frac{K(k_0)}{K'(k_0)} + \frac{K(k_1)}{K'(k_1)}} \quad (4-15)$$

By considering an available commercial dielectric substrate with permittivity of 2.94, the variation of characteristic impedance in terms of signal line width (w), gap size (g), and the thickness of air-filled area (h_1) under the signal line is given in Fig. 4-3. For this analysis, the thickness (h_2) of the dielectric filled part is fixed with the thinnest available substrate which is 5 mils (0.127 mm).

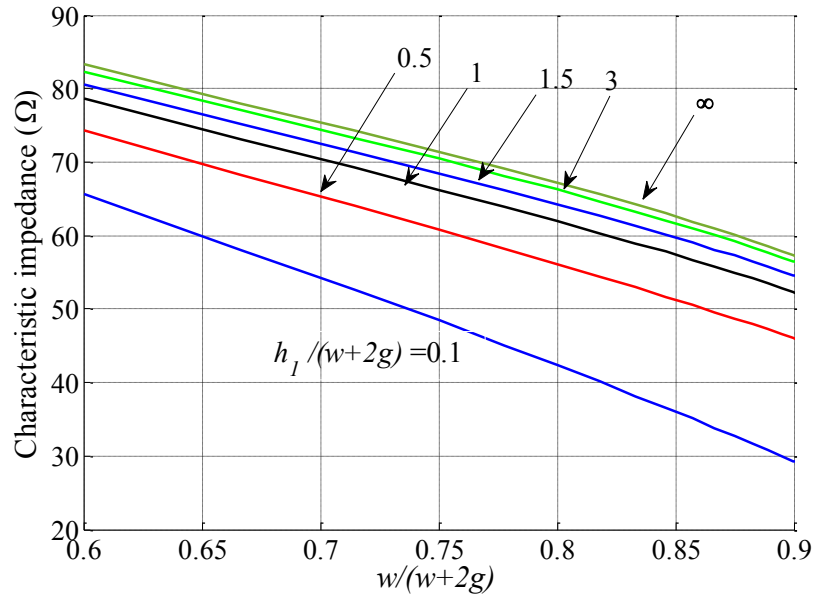


Fig. 4-3. Characteristic impedance for partially air-filled CBCPW ($\epsilon_r = 2.94$).

4.3 Contactless Air-Filled SIW Fed by Partially Air-Filled CBCPW

As mentioned in Chapter 3, the unshielded discontinuous region in the transition from the excitation where the covering PEC lids of the contactless air-filled SIW are meeting the intermediate substrate, besides of the dielectric to air-filled transition might cause some losses in the whole waveguide performance. To tackle this problem, the partially air-filled CBCPW, which is introduced and analyzed in the previous section can be utilized to feed the air-filled SIW. Feeding the air-filled SIW with this transmission line, enables the air-filled waveguide to be excited directly with an air-filled transmission line without any need for dielectric-to-air transition. To hold the signal line in the air-filled CBCPW, a thin substrate has to be used on top of the air-filled etched substrate of CBCPW; and it can continue to cover the air-filled SIW. Therefore, for the contactless air-filled SIW, the configuration of the unit cells around the air-filled guiding medium should be modified to include the thin covering substrate. This modified unit cell is shown in Fig. 4-4. In this cell, a thin dielectric substrate is considered at the top of the upper patch which is the thin covering grounded substrate layer that holds the CPW line. On the other side, the estimated 15 μm of the possible gap is considered such as the cell of Fig. 3-3 because the waveguide will be covered with a PEC lid from the other side. In other words, the only difference

between this cell and the cell of Fig. 3-3 is the additional thickness of the substrate on top of the upper cell. Dispersion diagram of a periodic structure comprising this unit cell is plotted in Fig. 4-5. The bandgap provided by this cell is limited compared with Fig. 3-4, especially from the upper end of the bandgap due to increasing the gap distance on the upper side of the cell. But it provides the band gap for the operating frequency of the proposed waveguide, which is between 30 and 50 GHz. The contactless air-filled SIW geometry fed by the proposed air-filled CBCPW is shown in Fig. 4-6(a). The conventional CBCPW to SIW transition, which is etched on the covering layer at the end of the CPW signal line, is utilized to couple the signal from the feed line inside the SIW. The electric field distribution inside the layers of the waveguide is shown in Fig. 4-6(b) and (c). In

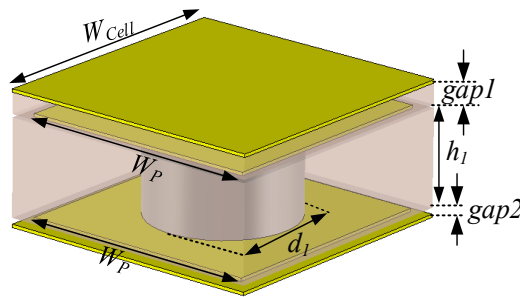


Fig. 4-4. Modified unit cell of the contactless air-filled SIW to be fed with air-filled CBCPW ($W_p=1.3$, $d_1=0.8$, $h_1=0.508$, $gap1=0.127$, $gap2=0.015$ all mm).

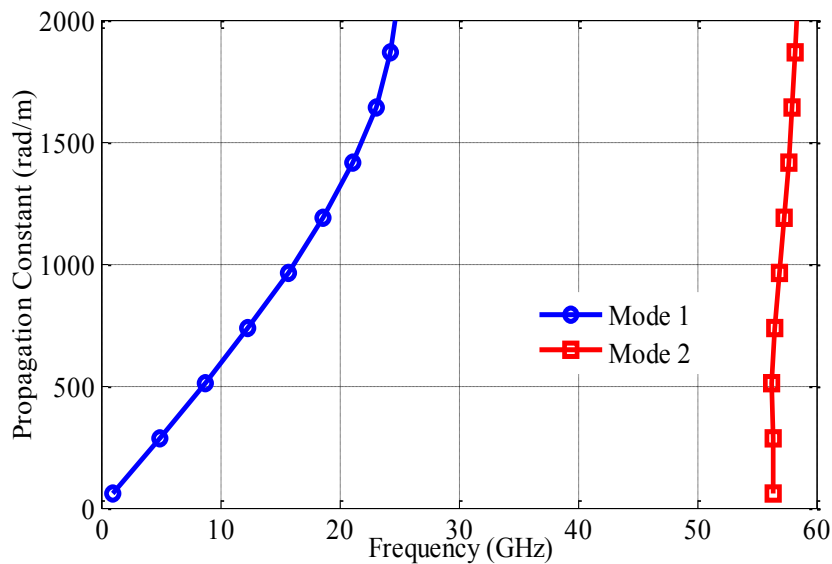


Fig. 4-5. Dispersion diagram of the modified cell of contactless air-filled SIW.

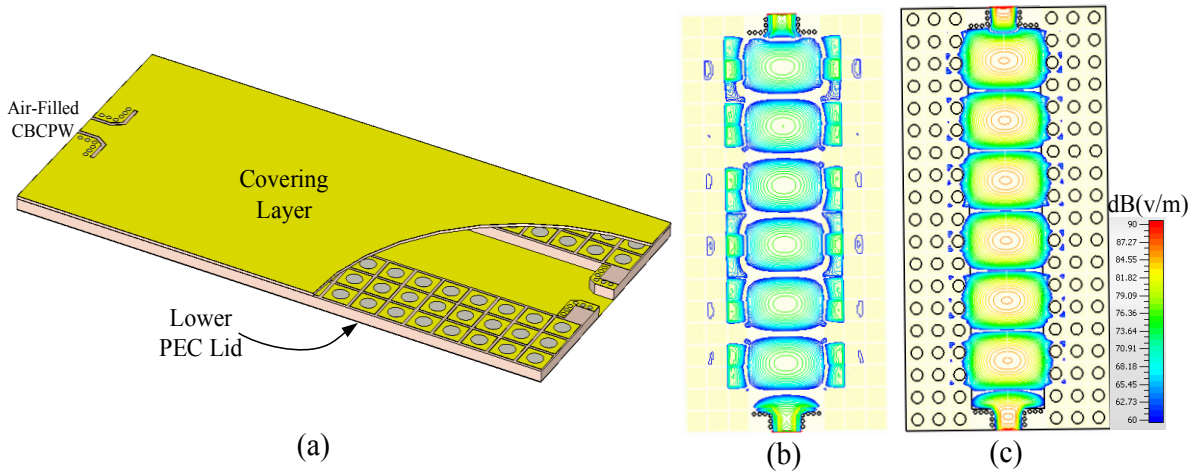


Fig. 4-6. Geometry of the contactless air-filled SIW fed by air-filled CBCPW (b) Electric field distribution inside the covering layer (c) Electric field distribution inside the main layer.

the main layer, the propagation is limited by the via array around the air-filled guiding medium, which meets the conventional SIW conditions given in (3-1). In the upper layer, the thin-dielectric-filled PEC-AMC parallel plate provides a stopband region for suppressing waves outside the waveguide boundary. Besides, PEC-AMC parallel plate on the lower side of the waveguide blocks the leaking waves from any tiny gap with lower PEC lid. Comparing with the previous method of exciting contactless air-filled SIW, here there is much less discontinuity in the transition from the

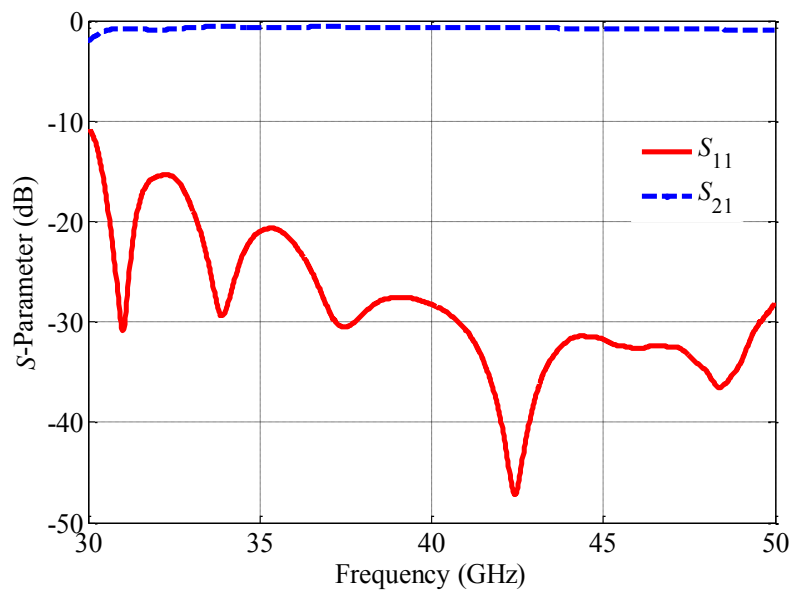


Fig. 4-7. Simulated S -parameter response of contactless air-filled SIW fed by air-filled CBCPW.

exciting point of the air-filled waveguide. This is because an air-filled transmission line is exciting the waveguide and the layers on the both sides are covering the whole waveguide and the transition so that no discontinuity of the layers happens along with the propagating wave. The simulated reflection and transmission coefficient responses of this waveguide are plotted in Fig. 4-7 by considering 15 micrometers of the gap with the lower lid. This tiny gap could also happen between the upper AMC surface and the covering grounded thin dielectric slab, which can be considered or ignored in the simulation. Because there is a dielectric separation between the upper conductor plane and AMC surface, and adding a tiny air gap to this dielectric separation would not change the waveguide performance.

4.4 Conclusion

A less dispersive conductor-backed CPW based multi-layer PCB technology has been represented. The line is constituted of three layers. The thick middle layer has been cut to support wave propagation in the air medium. The top layer is holding the signal line, and lateral grounds and the lower layer are supporting the backed conductor. The group delay comparison between this line and other counterparts shows the less dispersive characteristic of the line in the millimeter wave frequency band. As this configuration of the CBCPW is novel in the classification of the planar coplanar waveguides, a quasi-static analysis of the proposed line base on conformal mapping has been utilized to reach an approximate design expression of the characteristic impedance for the different thickness of the layers.

One issue that has been faced in exciting the contactless air-filled SIW was the discontinuity of the layers in the contact region of the covering PEC lids with the complete conductor of the intermediate layer in the transition section. The proposed configuration of CBCPW enables the contactless air-filled SIW to be fed directly by an air-filled transmission line. Therefore, the upper and lower lids of the air-filled SIW can be shared with the partially air-filled coplanar line. However, the unit cell configuration of the contactless air-filled SIW has to be modified to include the thin covering grounded substrate that holds the signal line of CBCPW.

Chapter 5

SUBSTRATE INTEGRATED HORN ANTENNAS WITH IMPROVED PERFORMANCE

5.1 Substrate Integrated *H*-plane Horn Antenna Loaded with Open Parallel Transitions

5.1.1 Motivation

Since the substrate integrated horn antenna is inclined to be integrated with other circuits around, which are mostly mounted on high dielectric constant substrates, the *H*-plane horn will be faced with high reflection response because of the aperture discontinuity. Accordingly, improving reflection feature of the *H*-plane horn fabricated on a high dielectric constant substrate is more beneficial. In this section, a new method is introduced which provides high dielectric constant *H*-plane horn with a variable matching bandwidth.

5.1.2 Substrate Integrated Horn with Open Parallel Transitions

The basic design of the substrate integrated waveguide with metallic vias has been formulated in [37]. The antenna is realized with metallic vias of diameter d with a period p that has the limits of

$$d < \frac{\lambda_g}{5}, \quad p < 2d \quad (5-1)$$

where λ_g is the guided wavelength of the dominant mode in the SIW. By flaring the two walls of the waveguide in the plane normal to the electric field, the integrated *H*-plane horn antenna is achieved. Design guidelines for conventional *H*-plane horn antennas given in [73] have been utilized to achieve the highest directivity of the horn. In light of this, the horn length (L_h) and aperture width (D_h) have to satisfy the following relation:

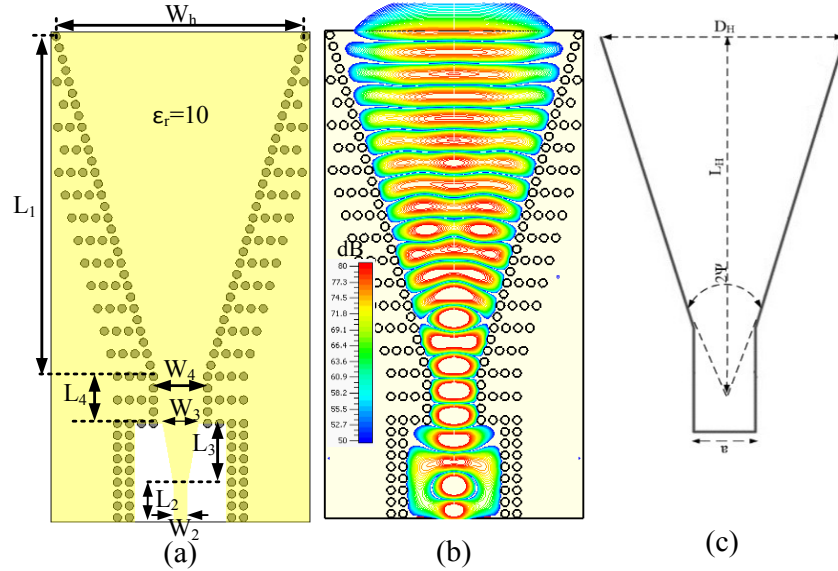


Fig. 5-1. (a) Basic geometry and parameters of H -plane horn (b) Geometry of simple substrate integrated H -plane horn antenna (c) Electric field distribution inside designed simple substrate integrated H -plane horn antenna.

$$D_h \cong \sqrt{3\lambda_g L_h} . \quad (5-2)$$

Rogers 6010 substrate material with permittivity of 10.2 and a thickness of 1.27 mm (h_1) is selected for the horn design. To equip the antenna with a planar feeding feature, a microstrip line is used to excite the integrated waveguide of the horn in the frequency band of its dominant mode. For this reason, a tapered line has to be printed as an interconnection between 50 Ω initial microstrip line and the SIW. This tapered transition [7] is utilized to make an adequate mode transformation from the quasi-TEM mode of the microstrip line to the dominant TE_{10} mode inside the SIW. Some basic principles for this transition are reported in [74] through experimental analysis; however, the optimum dimensions can be achieved by fine-tuning of a back-to-back transition to reach the best return loss response. The geometry of a microstrip-fed the horn antenna is shown in Fig. 5-1(b).

The additional vias around the horn walls are to suppress the parallel waveguide modes excited around the horn. The effect of the presence of these vias on the field distribution is shown in Fig. 5-2. To reduce the reflection coefficients, two slots near the horn apertures are added to the top

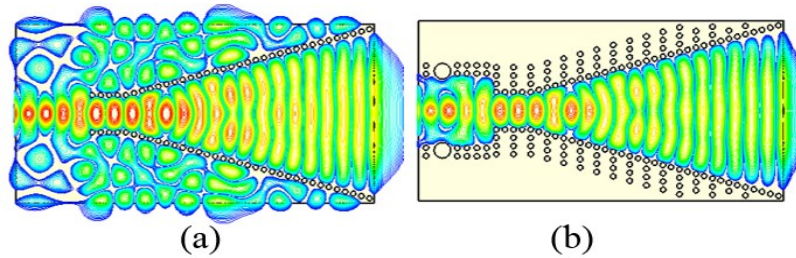


Fig. 5-2. Field distribution inside the substrate of simple integrated H -plane horn (a) Without outer vias (b) With outer vias.

and the bottom walls. The slots near the horn aperture make some cancellation of the reflection from the horn radiating aperture similar to the technique used in [75] - [76] where we considered the aperture as another radiating slot. Having the slots on both sides of the horn widens the beam width in the E -plane and further increases the back radiation. Therefore, parallel transitions are added to redirect the slots radiation to be in the same direction as the horn aperture. To facilitate the transition construction, a low permittivity substrate is used (Rogers RO3003 substrate with a thickness of 1.52 mm (h_2) and relative permittivity of 3) instead of air. The geometry of the horn loaded with the parallel transitions through long transverse slots is given in Fig. 5-3. For the redirected radiation to be in phase with the horn aperture, the transition should be shorted at the

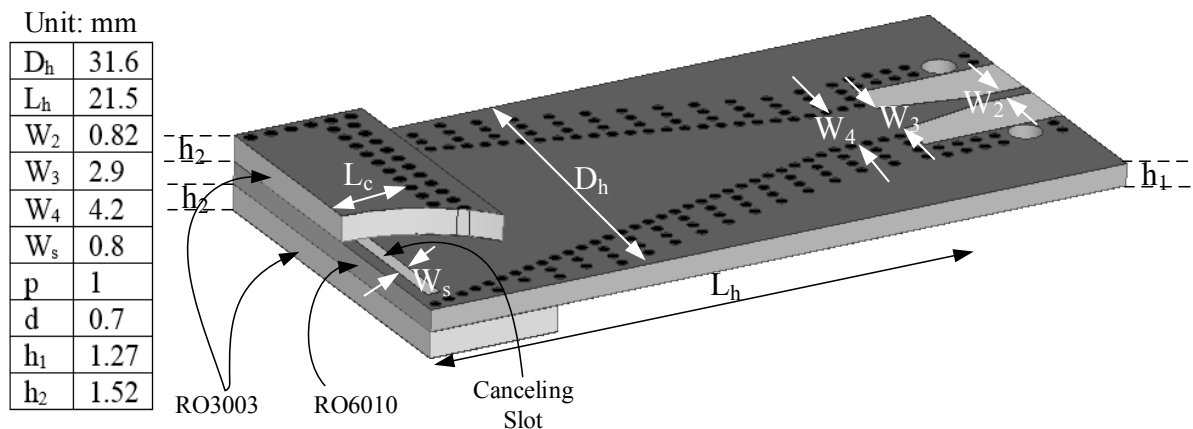


Fig. 5-3. The geometry of the substrate integrated H -plane horn antenna loaded parallel transitions by long transverse slots, and design dimensions.

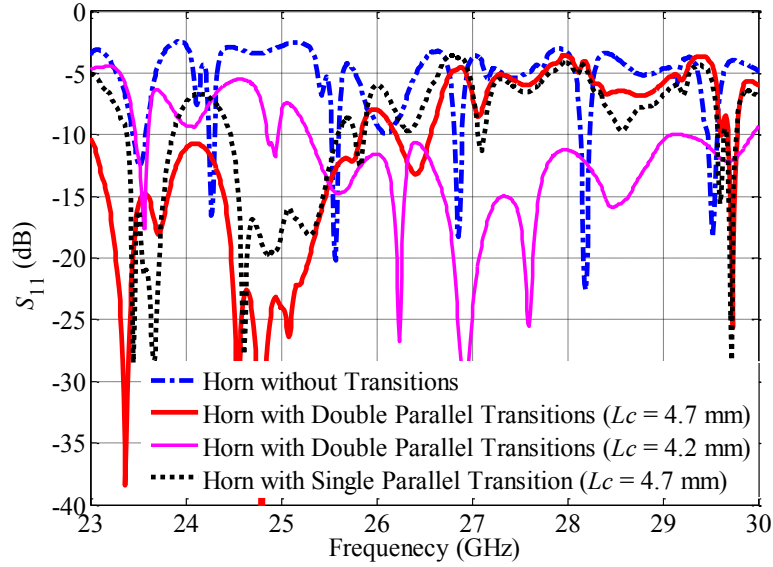


Fig. 5-4. Simulated reflection coefficients for the horn with the transition (single or double) and without the transition.

slot edge. However, practically, shorting the transition at the slot edge is not possible and the plated vias should be shifted away from the edge. The proper shift is a half wavelength that keeps the impedance at the slot edge looking towards the transition to be zero. The slots have the same dimensions and locations on both sides with a width of W_s . The depth of the transitions (L_c) from the aperture affects the matching operating frequency band. Thus, ideally, the effective depth for a transition should be three-quarter wavelength. The introduced parallel transitions, which are supposed to alleviate the aperture discontinuity, could be reduced to a single one located on the top or bottom side of the horn in case of strict limitations in antenna dimensions. For the single transition, an improvement in the antenna bandwidth performance can be obtained. However, the impedance bandwidth would be limited in comparison with double transitions, and the radiation pattern symmetry in the E -plane deteriorates.

5.1.3 Simulation and Fabrication Results

The proposed horn with the parallel transitions is simulated using CST Microwave Studio and fabricated with multilayer PCB process. The return loss response of the horn without the transitions is compared in Fig. 5-4 with the same horn when it is loaded with a single and double parallel transition. The horn without transitions shows high reflection response. However, loading the horn

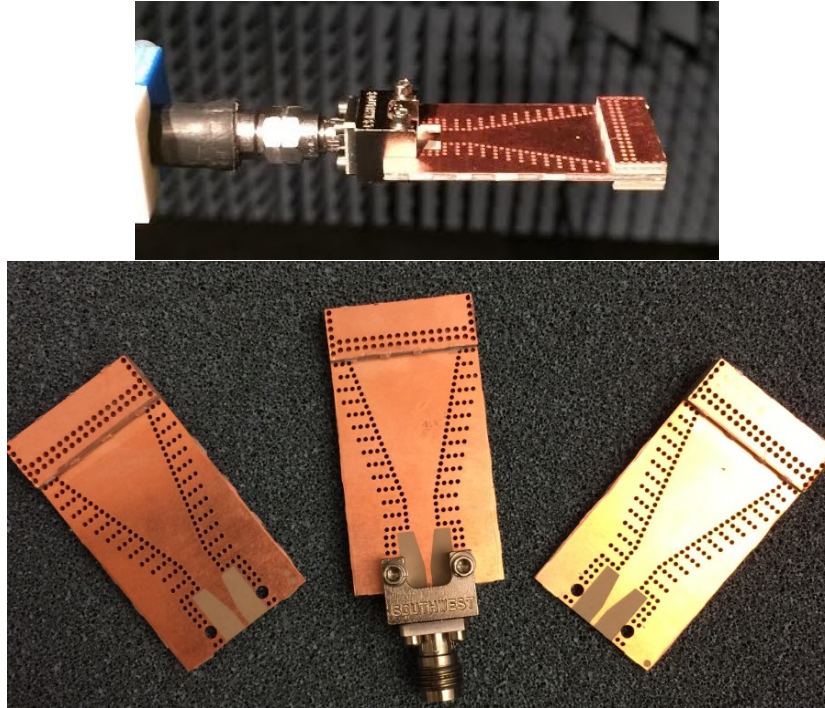


Fig. 5-5. The fabricated prototypes of substrate integrated horn with parallel transitions.

with single or double transitions improves the matching of the antenna. It is clear that adding double transitions around the aperture instead of single one results in better matching performance. By decreasing the length of the transitions from 4.7 mm to 4.2 mm, the center frequency of the impedance bandwidth is shifted from 24.57 GHz to 27.5 GHz. When both transitions are used, at

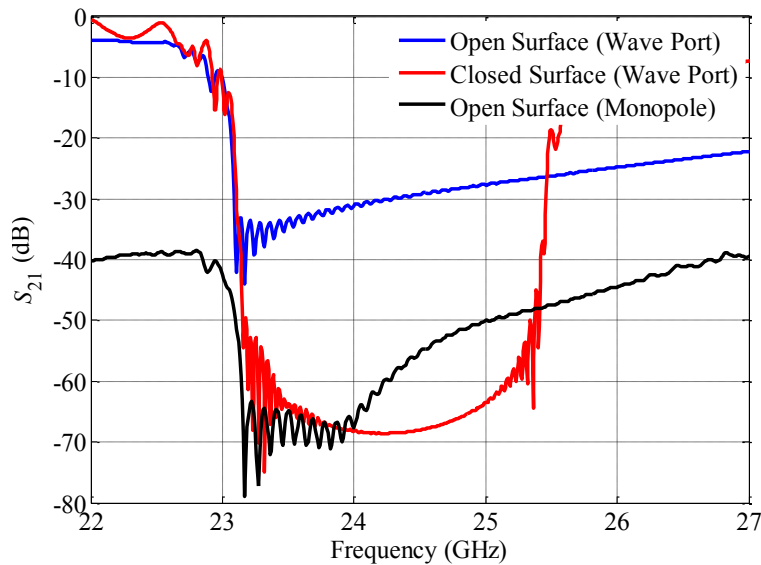


Fig. 5-6. Measured return loss response of the fabricated H -plane horn with parallel transitions.

least, 12% simulation bandwidth is achieved. Prototypes of the antenna with double parallel transitions of 4.7 and 4.2 mm length are shown in Fig 5-5. The antenna is fed using a 1.85 mm female type connector, which is fastened to the antenna by a couple of screws around the microstrip line. The performance of the fabricated samples has been evaluated regarding the reflection and radiation pattern responses. The measured reflection coefficients of the antenna with the transitions are plotted in Fig. 5-6. These results can be compared with the simulated results in Fig. 5-4. The transition depth is a very sensitive parameter as it can shift the matching bandwidth significantly.

It is also observed that the present design improves the antenna back radiation. The H -plane horn without the transitions has considerable back radiation because its aperture behaves as a long slot suspended in free space. The proposed horn with the parallel transitions has lower back radiation since the transitions act as high impedance chokes around the aperture. The high

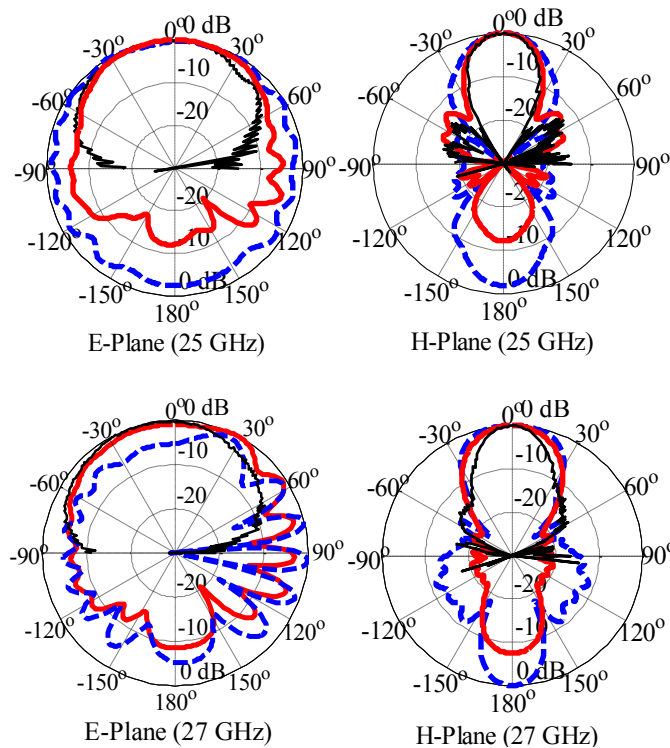


Fig. 5-7. Radiation patterns of the H -plane horn without and with the transitions, blue dashed lines, simulated without transitions; red solid lines, simulated with transitions; and black thin lines, measured with transitions. Upper patterns at 25 GHz for the 4.7 mm transitions and the lower patterns at 27 GHz for 4.2 mm transitions.

impedance reduces the surface currents strength of the horn walls and consequently reduces the antenna back radiation. The single transition seems to have half the effect of the double transitions in terms of the back radiation. This is another advantage of using double transitions over a single one besides having wider impedance bandwidth. In Fig. 5-7, the radiation patterns of the H -plane horn are provided with and without the transitions. Without the transitions, the radiation patterns have wider beam widths in both E - and H -plane. However, the radiation patterns of the antenna with the transitions show narrower beamwidth in both planes. Also, the back radiation is lower.

5.2 Substrate Integrated Horn Antennas with Uniform Aperture Distribution

5.2.1 Soft and Hard Horns and Surfaces

As mentioned in Chapter 1, the natural boundary condition of the horn aperture makes the field distribution tapered at the radiation aperture. For the H -plane horn antennas especially the integrated ones, the tapered aperture distribution results in limited aperture efficiency and this efficiency cannot be improved considerably by widening the aperture of the H -plane horn. As the boundary condition of the walls decreases the field intensity in wall regions.

For horn antennas, maximum directivity can be achieved if the horn is designed to have a uniform aperture. In recent years, a new group of horns called “hard” horns has such features, and they are just simple horns with modified walls to realize the hard boundary conditions. The definition of hard and soft electromagnetic surfaces was firstly studied and formulated in [77]-[79] in comparison with corresponding surfaces in acoustics in addition to their possible applications on horn antennas. The relation between these surfaces and electromagnetic band gap structures (EBG) was presented in [65] with respect to their STOP and GO characteristics of surface waves. Kildal clarified the concept of soft and hard horn antennas including balanced hybrid conditions at the design frequency in [80]. Briefly, they can be defined by the electric and magnetic field components tangential to the boundary. Considering E_t and H_t as transverse and E_l and H_l as longitudinal components with respect to the direction of propagation the definitions of soft and hard surface impedances can be given as:

$$Z^{TE} = Z_t = \frac{E_t}{H_l} = 0 \text{ (soft)}, \infty \text{ (hard)} \quad (5-3)$$

$$Z^{TM} = Z_l = -\frac{E_l}{H_t} = 0 \text{ (hard)}, \infty \text{ (soft)} \quad (5-4)$$

In other words, a tapered aperture distribution characterizes soft horns, generating low side lobe levels, such as transversely corrugated horn with zero field intensity on the horn walls [81]. Hard horns support uniform aperture distribution resulting on high directivity with high aperture efficiency and high side lobe levels. The realization of hard horns can be achieved by longitudinal corrugations filled with dielectric material on the horn wall, or by longitudinal strips on a dielectric wall liner, which is firstly introduced in [82]-[83] and later thoroughly analyzed in [84]-[85].

Hard horn antennas are also termed as “aperture controlled” or “narrow band” antennas since they have a frequency-dependent beam width [85]. In [86] a dielectric loaded hybrid-mode horn antenna with the versatility of being adjusted to satisfy either the hard or soft conditions or any boundary between hard and soft under the balanced hybrid condition is presented. Finally, in [87] a review study and comparison have been made on different types of presenting hard horns.

In general, by increasing the transverse wall reactance of the horn antennas, the field intensity at the wall increases. For smaller values of transverse wall reactance, the field intensity is almost zero at the wall, so the horn operates as a soft horn. When this reactance goes to infinity, it results in constant field intensity over the aperture and therefore higher directivity with a smaller beam width due to the increased aperture efficiency which is a feature of the hard horn antenna.

Here, the anisotropic boundary condition is applied to the substrate integrated H -plane horn to realize the hard horn antenna features.

5.2.2 Planar Strip-Via Array Soft Surface Design

From the previous literature, it can be found that soft surfaces have been utilized to reduce the back radiation and the mutual coupling between the elements in the antenna structures [88] - [90]. However, in [65] they are preferred for mutual coupling reduction than regular EBG surfaces since soft surfaces are aiming to cancel both vertical and horizontal polarizations.

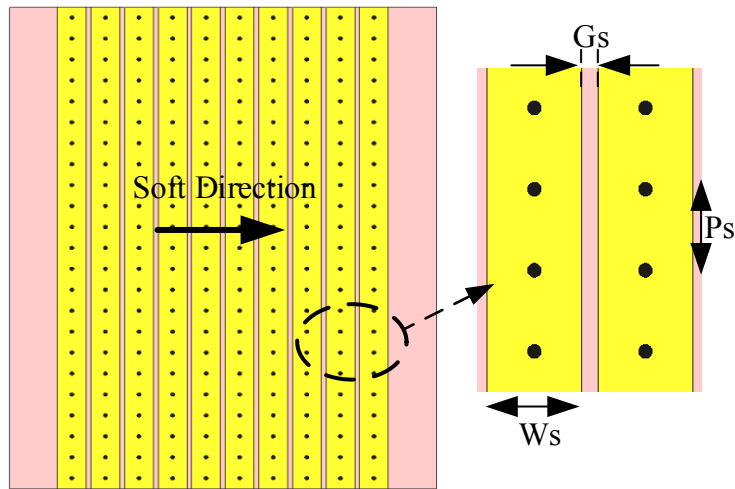


Fig. 5-8. Geometry of the strip-via soft surface.

To differentiate with the EBG surfaces, the soft surfaces are usually implemented to operate in a single direction. These surfaces are realized using air-filled or dielectric filled corrugations or long strips with a centrally located metal post in the planar format.

For an end-fire antenna such as H -plane horn antenna which is radiating from the substrate cutting edge, the conducting H -walls of the horn are more likely to support the aperture radiated waves; in other words, the solid H -wall conductors of this horn are ‘hard’ for the aperture wave polarization. Therefore, they can be easily supported by the solid conductors of the antenna to travel the antenna backside so that they intensify the antenna back radiations. To deal with this problem, which has not been considered so far, applying soft surfaces around the horn aperture could be useful. Therefore, a single direction strip-loaded soft surface with a centrally located vertical wall, which is realized by metal pins or metallized via holes, can be utilized for this application. The geometry of the analyzed soft surface is shown in Fig. 5-8.

The critical parameters defining the stop band of the surface are the width of the strips, the gap between them, and the metallic via spacing on the middle of the strips. In order to analyze the performance of the surface, a finite structure composed of a grounded dielectric slab with a finite number of periods of the soft surface is created. Then, the transmission parameter (S_{21}) is computed in the soft direction to evaluate its filtering properties. The analysis is performed in the bandgap direction of the surfaces; that is when the waves propagate transverse to the direction of the strip.

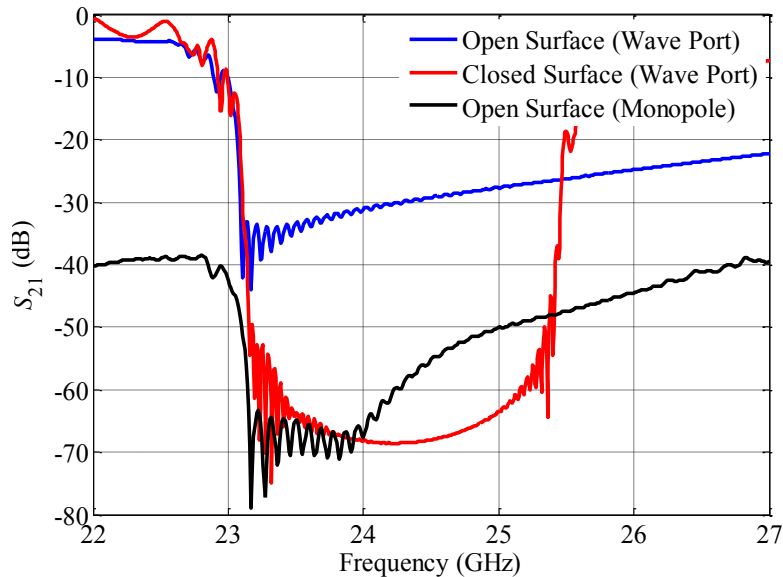


Fig. 5-9. Transmission coefficient of soft surface with different excitations.

A couple of waveguide ports provided by the simulator are used to excite the surface, which is open to free space. This simple setup is meaningful enough to find out and set the bandgap provided by the surface. The PMC boundary conditions are applied to the lateral sides of the finite soft surface. Moreover, since the open free space would require a significant computation volume, it is acceptable to assign the PEC boundary condition with a distance greater than the free space wavelength above the surface that results in the same filtering response, but with a higher level of transmission. As the surface is about to impede the propagation of the normally polarized wave, which is emitted from the antenna aperture, the surface analysis is repeated by two monopole antennas that are radiating the same polarization of the aperture waves. In Fig. 5-9, the transmission coefficients of the designed soft surface are shown under different scenarios. It can be concluded that the designed surface for 25 GHz acts as a soft surface within a bandwidth of 2 GHz frequency.

5.2.3 Hard Conditions in the Integrated Horn

For dielectric-filled horns such as substrate integrated horn antennas, the increment in the transverse wall impedance to reach a hard condition can be accomplished by making inverse-graded index behavior inside the horn through perforating the horn substrate, or by cutting part of the substrate while having a thickness of higher permittivity at wall regions of the horn. Both

methods can be applied to the integrated horn to reach a uniform amplitude distribution of electric fields at the aperture. However, in order to propose a better design for the hard horn, we intended to compare these two methods of realizing hard conditions inside a dielectric-filled horn in terms of feasibility and bandwidth of improvement.

It is shown in [80] that air-filled horn antenna with longitudinal corrugations filled with a dielectric material with the relative permittivity of ϵ_r can realize hard boundary conditions when the depth of corrugations is:

$$d_h = \frac{\lambda_0}{4\sqrt{\epsilon_r - 1}}. \quad (5-5)$$

For dielectric-filled horns like substrate integrated horn, inside of the horn has to have lower permittivity than areas close to the wall to achieve this boundary condition. The important factor that makes this condition at the desired frequency is the thickness of the high dielectric constant on the horn walls, which could be determined by the following relation:

$$d_h = \frac{\lambda_0}{4\sqrt{\epsilon_{r1} - \epsilon_{r2}}} \quad (5-6)$$

where ϵ_{r1} is higher dielectric constant with the thickness of d_h backed by wall conductors, and ϵ_{r2} is the lower dielectric constant inside area of the horn. In order to realize the dielectric constant diversity inside the substrate integrated horn, which is totally fabricated with a single dielectric slab, the perforation procedure can be used for the substrate inside the horn. In the perforated substrate, if the hole diameter and spacing remain very less than half-wavelength, the quasi-static effective permittivity of the perforated area can be determined using the volume average method [91] summarized hereinafter:

$$\alpha = \frac{\pi}{2\sqrt{3}} \left(\frac{d_{per}}{p_{per}} \right) \quad (5-7)$$

$$\epsilon_{r(eff)} = \epsilon_r(1 - \alpha) + \alpha. \quad (5-8)$$

where d_{per} is the diameter of perforated holes, p_{per} spacing between the holes, and ϵ_r is the dielectric constant of the perforated substrate.

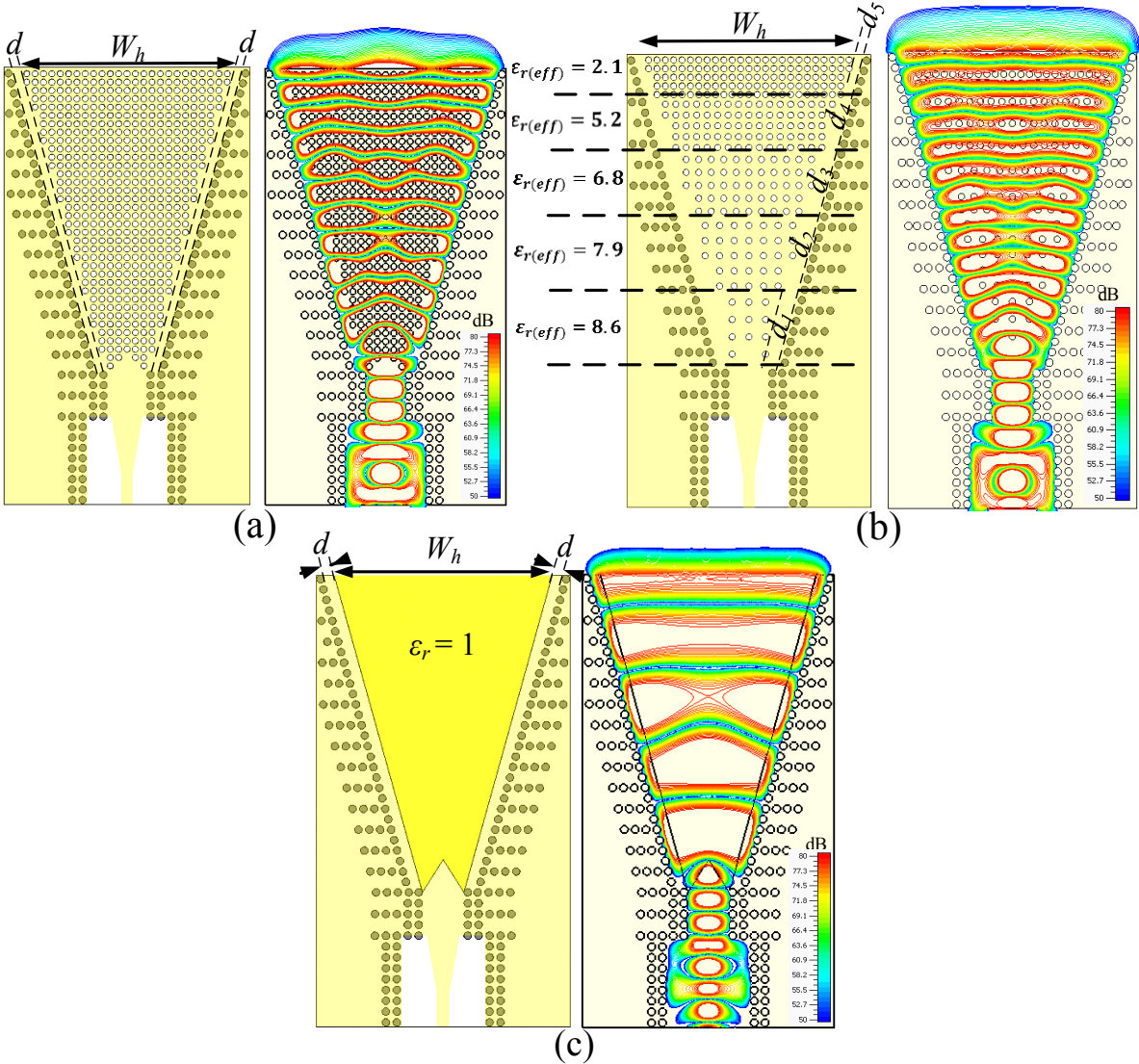


Fig. 5-10. Geometry and electric field distribution (at 25 GHz) of the substrate integrate horn antennas with realized hard boundary conditions by (a) Single step perforation (b) Five-step perforation (c) Substrate cut.

For the simple integrated horn shown in Fig. 5-1, which is designed for the optimum directivity based on (5-1) regarding its dimensions, perforation procedure is applied to reduce the effective permittivity inside the horn, as shown in Fig 5-10(a). The effective permittivity of the perforated region is reduced to 2.1 (ϵ_{r2}) by air-hole perforation with the diameter of 0.6 mm, while keeping a thickness of d_h , obtained by (5-6), with a high dielectric constant of 10.2 (ϵ_{r1}) on the lateral walls. As seen from the amplitude distribution of electric field and comparing it with simple horn aperture in Fig. 5-1, almost uniform amplitude distribution is achieved at the perforated horn aperture. This

uniformity happens at the hard frequency band for which the thickness of d_h on the walls is calculated with (5-5).

Alternatively, instead of single step perforation, five steps of perforation are applied to the same horn in Fig. 5-10(b). All of the steps are with the same via diameter, but with different spacing. Therefore, different effective permittivities are achieved which need different thicknesses of dielectric on the wall that can be calculated with the following relation:

$$d_{hn} = \frac{\lambda_0}{4\sqrt{\epsilon_r - \epsilon_{rn(eff)}}} \quad (5-9)$$

where $\epsilon_{rn(eff)}$ is effective permittivity of the nth step of the perforation and d_{hn} is the required thickness of high dielectric constant for the nth perforated region. In the integrated horn of Fig. 5-10 (b), the effective permittivity of the horn interior dielectric starts from 8.6 and end reaches to 2.1 with five steps perforation. The five-step hard boundary conditions implemented inside the horn makes a smooth transition from high to low dielectric constant until the aperture that provides a more uniform amplitude distribution comparing with the single-step perforated horn. In addition, applying different steps of perforation simplifies the antenna geometry due to reducing the number of air holes.

The hard boundary condition can also be realized by depleting the integrated horn interior and filling it with air while keeping a thickness of dielectric (d) on the walls. As the horn inside is filled with air ($\epsilon_r=1$), the main equation of (5-5) for the air-filled horns gives the required dielectric thickness on the horn walls, which is also used for conventional hollow rectangular or circular waveguide hard horns. For the horn in Fig. 5-10(c), the uniform distribution of the aperture is obtained by removing the horn inside dielectric to have the relative permittivity of air inside and keeping a thickness of high dielectric constant on the walls. The uniformity of the amplitude distribution at the aperture of this hard horn is clearer than the perforated hard horns. This is because of the fixed thickness of the dielectric on the E -walls throughout the horn that provides more accurate thickness wall dielectric at the hard frequency. However, for the perforated horns, the boundary of the dielectric thickness on the E -wall is not exactly constant along the horn due to the position of the perforation holes. In Fig. 5-11 the directivity of these integrated hard horns is compared with the simple horn given in Fig. 5-1 over the hard frequency bandwidth. As seen from

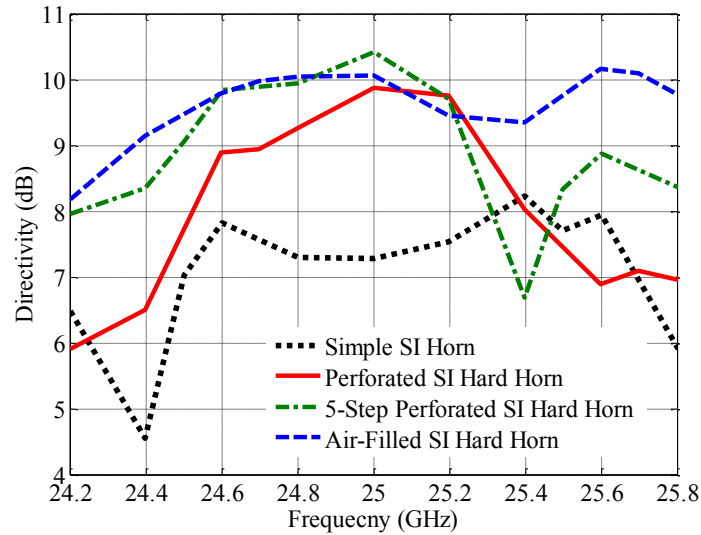


Fig. 5-11. Directivity comparison between simple integrated horn and perforated and air-filled hard horns.

this comparison, the hard boundary condition has improved the horn directivity more 2dB at 25 GHz, which is the center frequency of the hard condition, by making amplitude attribution of the aperture close to uniform. Comparing the three integrated hard horns of Fig. 5-10, the single-step perforated horn shows narrower bandwidth than the others, and the 5-step perforated horn shows the best improvement at the center design frequency. However, air-filled horn demonstrates more stable directivity enhancement at hard frequency band compared with two other perforated hard horns. Besides, air-filled horn demands less accuracy in the fabrication process than the perforated ones. The main difference between the perforated and air-filled hard horns is that the air-filled horn has to be covered with other grounded layers after the dielectric inside the horn is removed.

5.2.4 Air-Filled Substrate Integrated Horn with Uniform Phase and Amplitude Distribution of Aperture

5.2.4.1 Antenna Design

Based on design procedure for the H -plane horns of the optimum directivity in [73], an air-filled horn with the length of 5λ at the center frequency is designed. For this horn to be integrated into a substrate, a part of the substrate has to be cut to provide the air-filled horn. However, due to

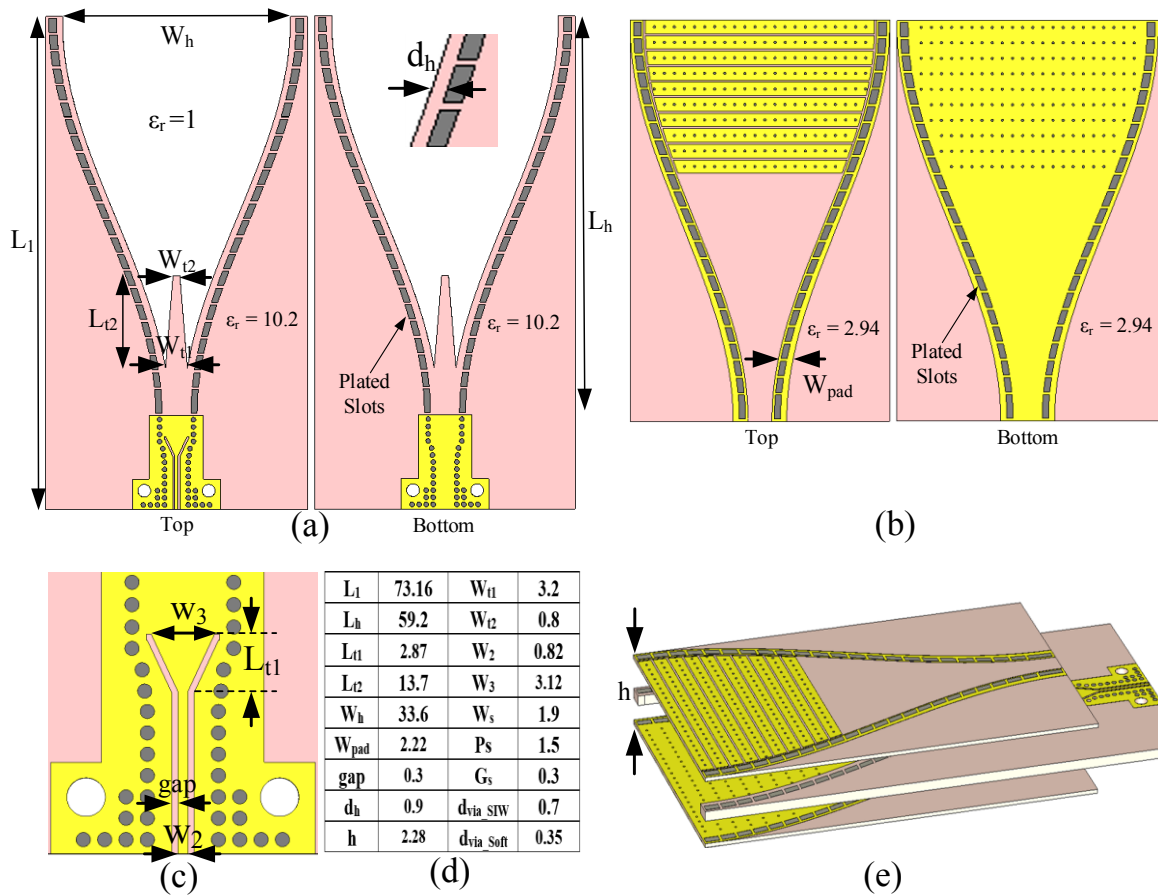


Fig. 5-12. Geometry of the air-filled H -plane hard horn antenna, (a) Middle substrate (b) Top and bottom substrates (c) CBCPW to SIW transition (d) Table of dimensions (unit: mm) (e) 3D view of the stacked layers.

fabrication limitations of the SIW structures, the metallic vias cannot be located exactly at the edge of the substrate cut regions to form the horn walls.

As mentioned, for an air-filled horn with the longitudinal corrugations filled by the dielectric material with a relative permittivity of ϵ_r , the hard boundary conditions can be accomplished when the corrugation depth d_h is calculated from (5-5). Therefore, positioning the plated vias of the SIW around the air-filled medium of the horn with d would be practically feasible. Yet, the cutting part must be carefully considered to maintain the constant thickness of the dielectric (d_h) on the lateral walls of the horn. After the cutting process of the substrate, which obviously eliminates the copper cladding of the removed part, to cover the removed area of the substrate to establish the horn medium, two other grounded substrates are needed to sandwich the main substrate from the top

and bottom sides. In fact, the fabricated horn should have three layers practically. The geometry of the proposed horn configuration is given in Fig. 5-12. The substrate material of Rogers RO6010 with a thickness of 1.27 mm and the dielectric constant of 10.2 is used as the main (middle) substrate. According to (5-5) using the high dielectric constant substrate requires a thin dielectric thickness (d_h) on the horn wall to make an increment in the transverse wall reactance for the hard conditions that finally adds a minimum width to the aperture.

It is known from the early literature that horn antennas with the uniform phase distribution of the aperture can be reached by the profiled shaping of the horn walls. For this hard horn, the profiled shape also applies to the E -walls of the horn to provide nearly uniform phase distribution. In other words, the horn length is kept the same as the simple horn designed by (5-2), but only the lateral walls are profiled to correct the aperture phase. This profiled flaring is accomplished by the plating slots starting from the horn throat region.

The horn feeding waveguide is kept as the regular SIW, which is exciting the air-filled horn by a tapered dielectric-to-air transition. The design of this transition has a considerable effect on the antenna matching. The conventional substrate integrated horn antenna usually has a poor return loss response because of the dielectric-air discontinuity in its aperture causing a high standing wave inside the horn. So, a transition is required to be added to the antenna aperture to alleviate this discontinuity. Since the proposed integrated horn antenna takes advantage of the air-filled medium inside, there is no dielectric-air discontinuity at the antenna aperture. In fact, the dielectric-air discontinuity for this integrated horn is moved from the aperture to the throat region of the horn. Accordingly, designing the right transition from the dielectric-filled feeding waveguide to the air medium inside of the horn can improve the antenna matching bandwidth. For the proposed antenna, tuning the parameters of the semi-triangle transition from the horn feeding waveguide, including L_{t2} , W_{t1} , and W_{t2} , smooths the dielectric-air discontinuity to the horn interior. The waveguide is excited by a conductor-backed coplanar waveguide (CBCPW) through a flared transition to SIW, shown in Fig. 5-10(c). The $50\ \Omega$ CBCPW is confined with lateral vias to prevent resonances from the dielectric-loaded waveguide mode. The reason for choosing CBCPW to feed the horn waveguide is that with the connected ground planes, the CBCPW is less prone to radiate

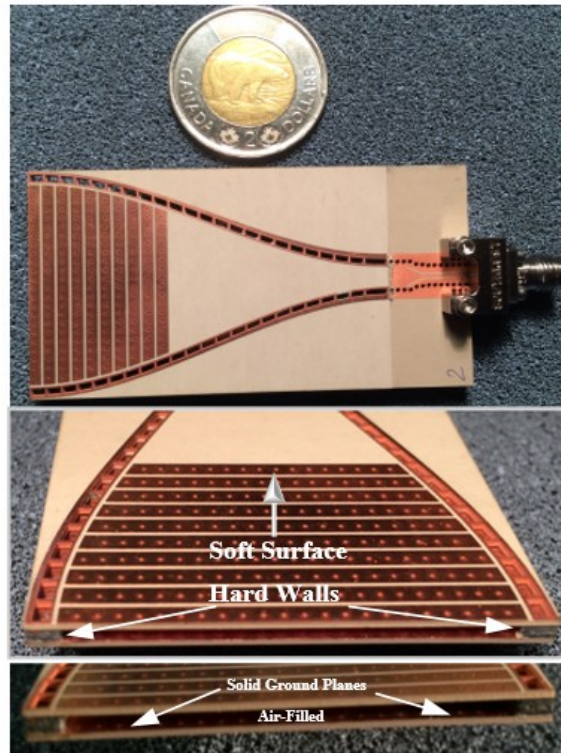


Fig. 5-13. The fabricated prototype with soft surface on the top and bottom and hard walls at the aperture.

and shows a higher isolation than microstrip line, especially for the high dielectric constant substrate, which has a higher concentration of the fields inside the substrate.

The conducting H -walls of the H -plane horn are more likely to support the aperture radiated waves contributing to the back radiations; in other words, the solid H -wall conductors of this horn are ‘hard’ for the aperture radiated wave polarization. Therefore, by taking advantage of the three-layer structure of the antenna, a couple of strip-via arrays are placed on the lower and upper substrates, which are designed to function as soft surfaces at the antenna frequency band. The substrate of RT/Duroid 6002 with 0.508 mm thickness is used as surrounding layers, which contain 10 rows of planar strips with centrally located vias. The design details of the soft surface are described in the previous section.

The ground planes of these soft surfaces, shown in Fig. 5-12(b), are shared with the H -walls of the horn that covers the air-filled area. In addition, the plated slots are applied through the three

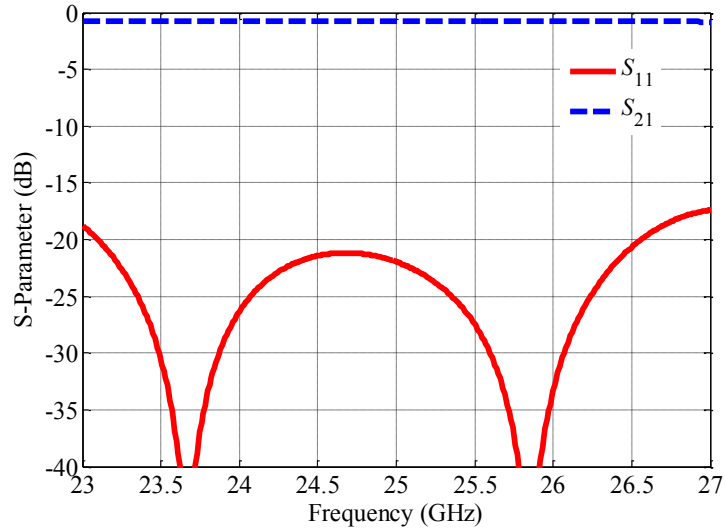


Fig. 5-14. Frequency responses of the return and insertion losses for the CBCPW to SIW transition.

layers in the fabrication process after stacking layers. Therefore, the strip-via array is confined from the lateral edges to prevent their connection with the plated slots. Considering the fabrication process constraints, a minimum width of the pad (W_{pad}) is needed around the plated slots to guarantee the excellence of plating. Although the antenna is composed of three substrate layers, the radiating aperture thickness (E -plane dimension of the aperture) is the thickness of the main substrate.

5.2.5 Simulation and Measurement Results of the Proposed Hard Horn

The fabricated prototype with an end launch connector is shown in Fig. 5-13. Since the antenna is excited by a CBCPW line, the design parameters of the CBCPW to SIW transition, shown in Fig. 5-12(c), are adjusted to obtain the best performance of the transition at the antenna frequency band. The S -parameters of the back-to-back connection of this transition is plotted in Fig. 5-14. The main antenna design attempt is to achieve a uniform amplitude and phase distribution of the aperture by applying the hard boundary conditions and profiled shape of the horn. The amplitude and phase distribution of the electric field at the design frequency of the hard condition, which is 25 GHz, is shown in Fig. 5-15. The almost uniform amplitude distribution of the aperture is achieved at the frequency of the hard condition. The phase distribution of the aperture is controlled by profiling

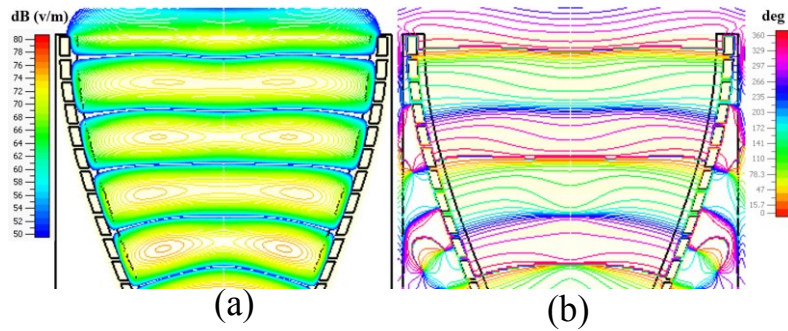


Fig. 5-15. Electric field distribution inside the air-filled hard horn at 25 GHz (a) Amplitude (b) Phase.

the horn shape starting from its throat region by changing the phase front along the horn propagating regions. The profiling changes the phase front from cylindrical within the horn to planar at the aperture. The hard condition also achieves the uniform distribution of fields on the radiating aperture. The effect of adding soft surfaces around the antenna can also be observed from the comparison given in Fig. 5-15 between the designed horn with and without soft surfaces. It can be seen that the strip-via soft surfaces around the horn suppress the back traveling waves. The simulated and measured return loss responses of the antenna are given in Fig. 5-16. The fabricated prototype shows wider impedance bandwidth than the simulation. The hard horn is naturally narrow band antenna since the hard boundary condition happens in a narrow bandwidth around

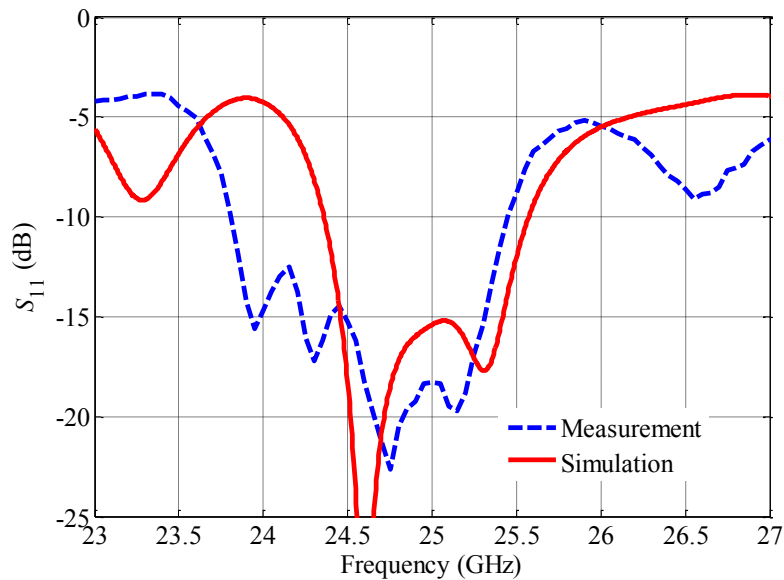


Fig. 5-16. Simulated and measured reflection coefficient of the air-filled substrate integrated hard horn.

the design frequency. Therefore, the antenna matching is tuned to cover the hard frequency band. Generally, the parameters that mostly affect the matching bandwidth of this horn are the thickness of the main substrate, its dielectric constant, and the tapered transition from the horn waveguide to

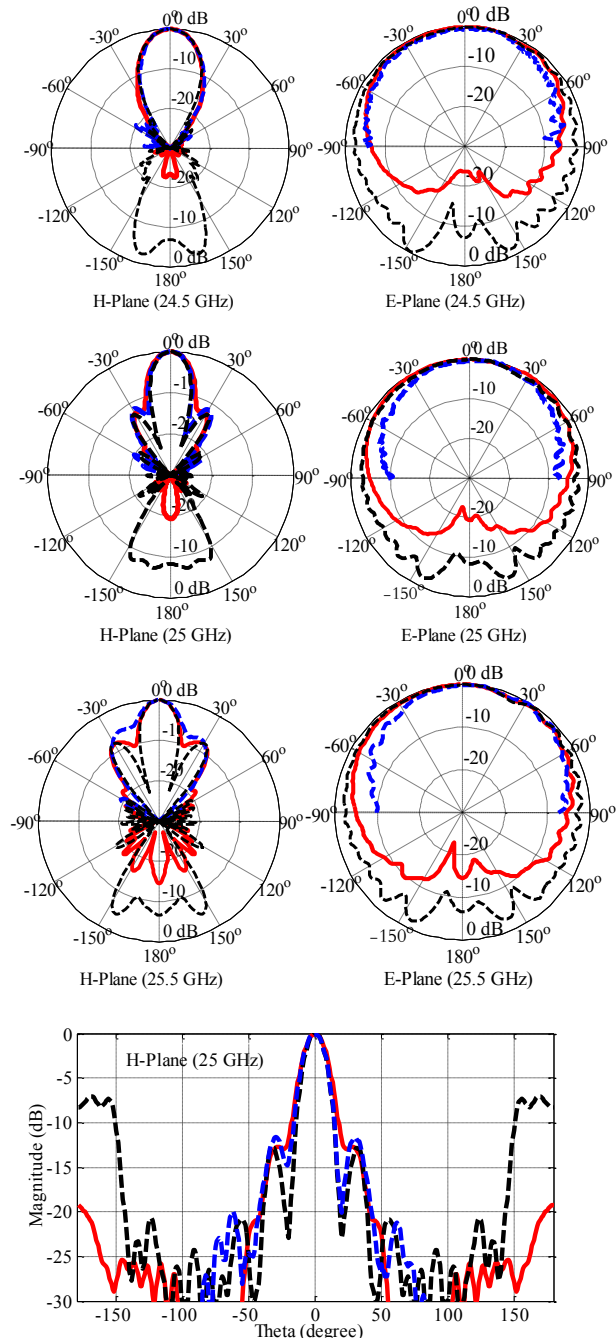


Fig. 5-17. Simulated and measured radiation patterns of the air-filled substrate integrated hard horn (solid lines, simulation; dashed black lines, simulation without soft surfaces; dashed blue lines, measurement).

the air medium. The discrepancy between the simulated and measured return loss responses could be attributed to the fabrication tolerances, especially the laser cutting procedure because the laser beam that follows the cut signs has a 2 mils diameter, which cuts 1 mil more on the other side of the cut. The width of the plated slots around the horn also widens for almost two mils after the fabrication process because of the laser cut tolerance. Besides, the layers are stacked and adhered to each other with epoxy glue with a thickness of nearly 5 μm and permittivity of three, which are not considered in the simulations.

The radiation patterns of the antenna at three frequencies are shown in Fig. 5-17. The simulated *H*-plane radiation pattern at 25 GHz is showing narrow beam width with a couple of side lobes at -13 dB, which proves the uniformity of the aperture distribution at the hard frequency. The rectangular plot of the *H*-plane radiation pattern at the middle frequency is also given in Fig. 5-17, which provide a better evaluation of the hard condition. The measured *H*-plane also reveals the aperture uniformity in the fabricated prototype. From the nature of the hard boundary conditions, the uniform amplitude exists in a limited bandwidth around the hard frequency, but the profiled shape of the horn makes the phase uniform for a wider frequency band. At the frequencies higher than the frequency of the hard condition, the side lobe levels are increasing to add up to the main beam and making wider beam width. The measured *H*-plane shows a rapid growth of the side lobes

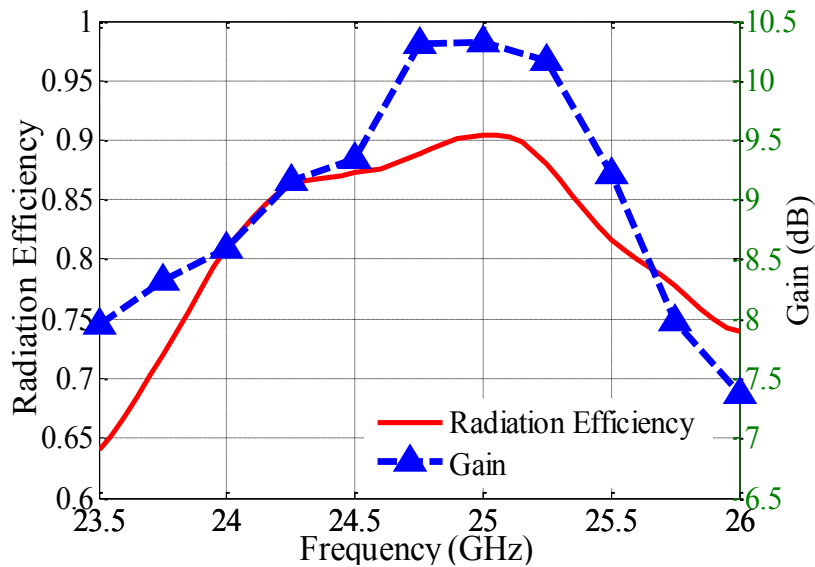


Fig. 5-18. Simulated radiation efficiency and measured gain of the proposed hard horn.

after the hard frequency because the hard frequency band might be shifted in the fabricated prototype due to the fabrication tolerances mentioned above, which may cause a different thickness of the dielectric on the horn walls.

Since the antenna is equipped with a couple of soft surfaces around its aperture, low back radiations are achieved. In Fig. 5-17, the simulated radiation pattern of the antenna without the strip-via soft surfaces are also plotted to make a clear comparison with the proposed horn equipped with soft surfaces. As seen from the radiation patterns in the both planes, at the central frequencies of the soft surface stopband, as per Fig. 5-18, the antenna back lobes are reduced to be better than -20 dB. Radiation efficiency and the measured gain of the antenna are given in Fig. 5-18. The uniform aperture distribution made by the hard condition and the profiled walls improved the gain and the aperture efficiency at the hard frequency band.

5.3 Millimeter-Wave Substrate Integrated Dual Level Gap Waveguide Horn Antenna

5.3.1 Motivation

As seen so far, the SIW based structures are inclined to be fed by the planar feeding mechanisms such as microstrip line because of simplicity and ease of fabrication on the same substrate. However, this obliges the substrate integrated H -plane horn aperture thickness to be limited to the thickness of the transmission line substrate. In fact, electrically thick substrates cannot be used for the integrated H -plane horn designs, which are supposed to be excited with the planar transmission lines. Because the thick substrate feed line would not operate perfectly at high frequencies due to its direct radiation. As a result, the horn ends up with limited matching bandwidth and deformed radiation pattern. Moreover, at the millimeter-wave frequencies, the width of SIW that feeds the horn becomes narrow and close to the thickness of the substrate. This makes the feeding of the SIW very difficult with planar feed lines, because designing the tapered transition to transform the quasi-TEM mode of the feed line to the TE mode of the integrated waveguide that functions adequately with lower loss is more challenging and impossible in any case, which adds a further barrier to the antenna matching bandwidth.

Here, by taking advantage of the printed ridge gap waveguide technology [29]-[32], the design of elevated substrate integrated gap waveguide (E-SIGW) is elaborated, which enable us to introduce a new design of the integrated horn antenna that makes the horn with thicker aperture than its feeding part. Besides, the integrated H -plane horn is fed by a low insertion loss transition from the planar feed line at millimeter wave frequencies, which is not easily possible with conventional SIW structures.

5.3.2 E-SIGW Design

The regularly printed ridge gap waveguide consists of a base substrate supporting the printed ridge surrounded by a patch-via mushroom of the periodic structure and a full conducting plate on the top separated by an air-gap. However, in the substrate integrated gap waveguide (SIGW) configuration, shown in Fig. 5-19(a), this air-gap is filled with a dielectric in which the wave is supposed to propagate. In other words, a single unit cell in the conventional ridge gap waveguide includes a patch-via mushroom with an air gap on top while in the unit cell of the SIGW, the air gap is filled with the dielectric on the top of the mushroom. In the modified version of printed ridge gap waveguide [31], a thin layer of dielectric is used between the air gap and the mushroom lattice in order to print the ridge on a separate layer. Printing the ridge on a separate layer gives more freedom to shape the ridge without the need to reform the unit cells positions or shape.

The proposed elevated SIGW (E-SIGW) takes advantage of the separate layer for the guiding ridge beside having another layer of the substrate on the ridge to fill the gap area. In Fig. 5-19(a), the configuration of the E-SIGW is illustrated. For the mushroom lattice, the substrate of RO6002 with a thickness of 10 mils is utilized because of its low permittivity and robustness in the fabrication process of closely repeated patch-via lattice. For the middle layer and the third layer, Rogers RT5880 with thicknesses of 10 and 20 mils is utilized. The geometry of the proposed unit cell for E-SIGW is also shown in Fig. 5-19(c) with dimensions. The dimensions of the unit cell including the patch size and the cells periodicity are adjusted to reach a bandgap in the 60 GHz frequency band. The dispersion diagram, also known as a k - β diagram, is used to predict the band gap region of the periodic structure. Since the periodic structure made by this unit cell has a square lattice shape and is symmetric in the longitudinal and transverse directions, according to Brillouin,

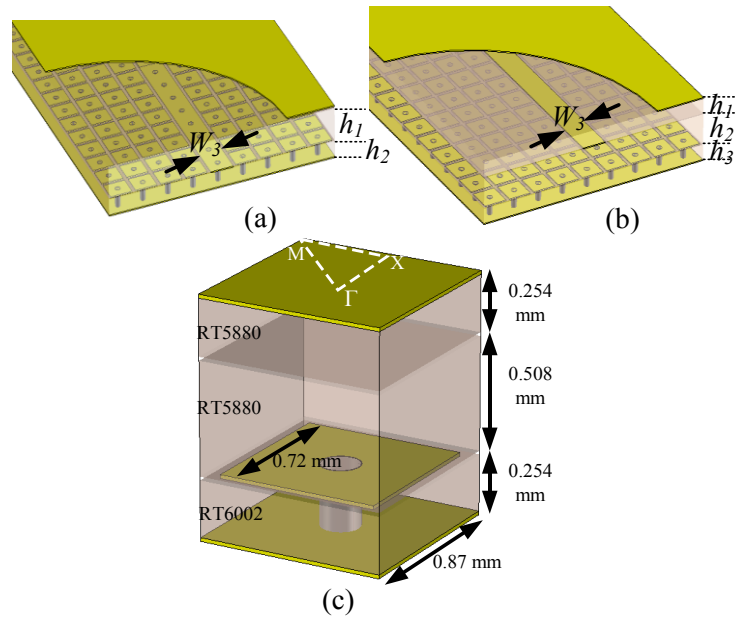


Fig. 5-19. (a) Substrate integrated gap waveguide (SIGW) (b) Elevated substrate integrated gap waveguide (E-SIGW) (c) E-SIGW unit cell.

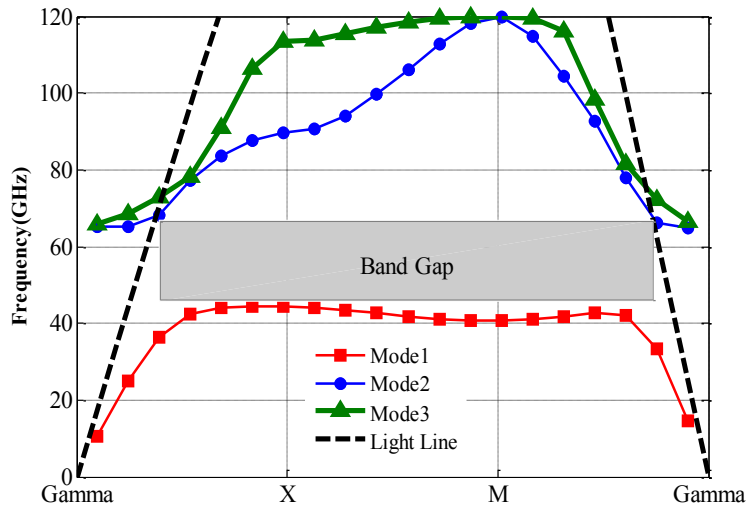


Fig. 5-20. Dispersion diagram of a single unit cell at E-SIGW structure.

all possible directions of propagation can be combined in an irreducible Brillouin zone [92] that is a triangular wedge with $(1/8)^{\text{th}}$ area of a square, which is indicated on the upper conductor of the unit cell in Fig. 5-19(c). The dispersion relation for different regions of Brillouin zone of the periodic structure composed of this unit cell is obtained using Eigenmode solver of the CST Microwave Studio. This dispersion diagram is given in Fig. 5-20. Light lines for the pure TEM

mode propagation in the same medium at the different regions are also plotted in the same diagram to realize the obtained band gap by the periodic structure of this unit cell. Based on the light lines, it can be concluded that the 2D periodic structure composed of this unit cell suppresses any propagation along its surface in the frequency band between 45 and 68 GHz. It is well known that increasing the thickness of the gap limits the band gap of the cell. In the given configuration of the unit cell, for instance, if both layers filling the gap are with 10 mils of substrate thickness, the bandgap would be from 45 GHz to 73 GHz. This means, cutting the thickness of the upper gap layer in half will widen the bandgap by 5 GHz. This may be beneficial for the E-SIGW in terms of wider operational bandwidth. However, in terms of the horn performance, reducing its thickness would make a considerable effect on the horn matching bandwidth and its radiation efficiency.

As the ground plane of the E-SIGW line is shared with the upper conductor of the periodic structure, the propagation would remain only between the elevated ridge and the upper conductor. The quasi-TEM propagation of the E-SIGW line can be observed from the dispersion plot of the one row of the cells with the guiding strip in Fig. 5-21. The uniformity and less dispersive identity of the single quasi-TEM mode propagation at the band gap region of the periodic structure can be seen by comparing this mode with the light line in the dispersion diagram.

In order to excite this line with a standard transmission line, a microstrip line is preferred because of its similarity in the propagation mode with the E-SIGW line. However, since the

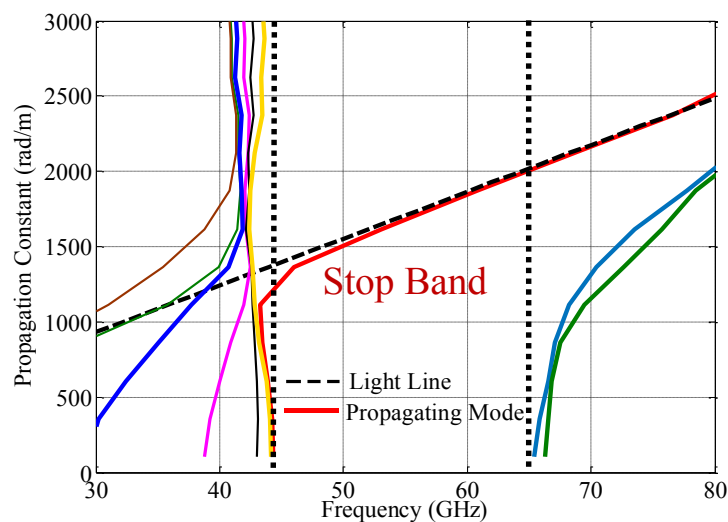


Fig. 5-21. Dispersion diagram of the E-SIGW line.

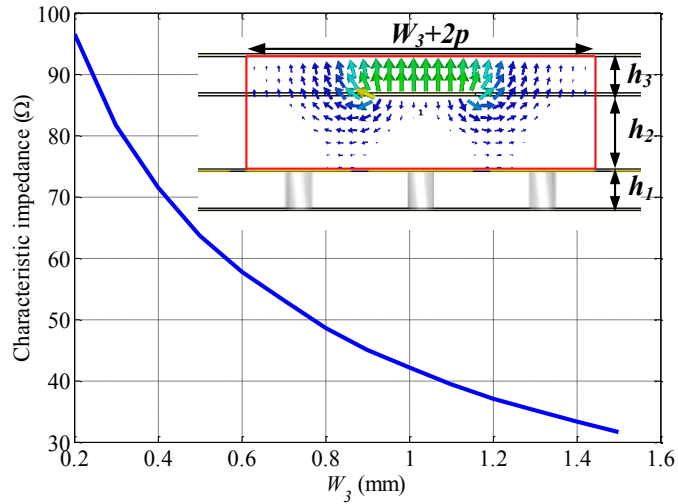


Fig. 5-22. Variation of the characteristic impedance of the E-SIGW line with the width of printed ridge, and the exciting wave port dimensions.

microstrip line and the E-SIGW line is supporting propagation in different environments, the propagating waves are seeing different effective permittivities. Accordingly, the E-SIGW line width for 50Ω characteristic impedance has to be extracted from the full wave analysis in order to be matched with 50Ω microstrip line. This analysis can be done in two different ways. First, the E-SIGW line can be excited with a couple of wave ports provided by the simulator; and by trying different widths of the line, the line width for 50Ω characteristic impedance can be obtained. However, for this analysis, the wave ports exciting the E-SIGW line have to be carefully considered to capture all fringing fields around the line. In Fig. 5-22, the E-SIGW excitation with wave port and its characteristic impedance for different widths of the line is plotted. It is observed that the optimum dimension of the wave port width to collect whole fringing fields and to get the correct characteristic impedance is to cover at least one period (p) from the lateral sides of the line in the transverse direction and to cover the whole gap region of the unit cells in the longitudinal

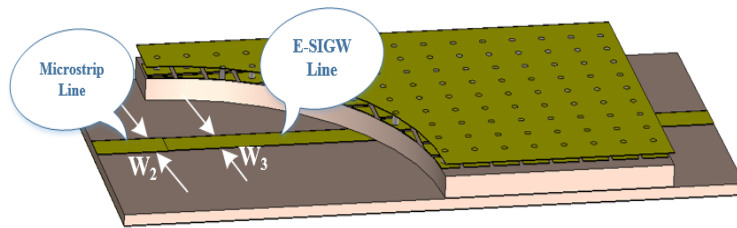


Fig. 5-23. Back-to-back transition from microstrip line to E-SIGW line.

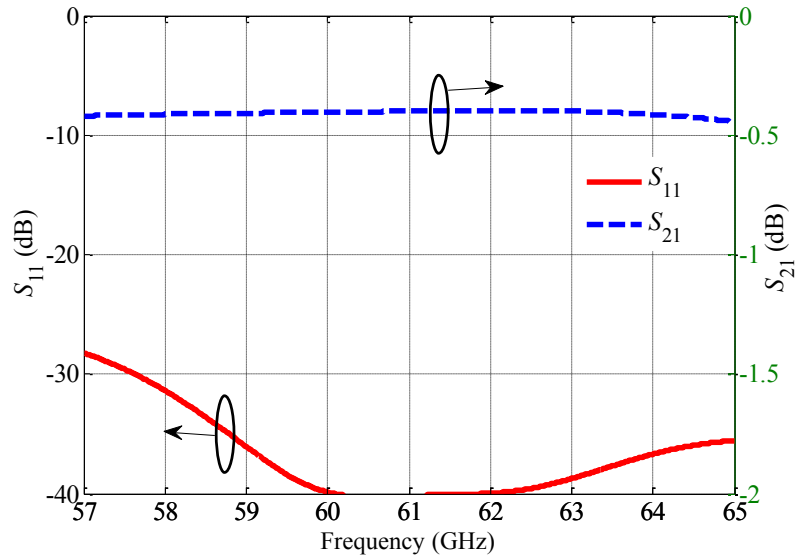


Fig. 5-24. Reflection and transmission coefficient responses of the back-to-back transition from microstrip line to E-SIGW line.

direction. The second method to find the impedance of the E-SIGW line is to connect it to a couple of the $50\ \Omega$ microstrip lines from both sides and repeat the full wave simulation for different widths of the line (W_3) in order to reach the best reflection and transmission coefficient responses. In Fig. 5-23, a back-to-back transition from microstrip line to E-SIGW line is shown. The E-SIGW configuration in Fig. 5-22 is rotated in Fig. 5-23 to have a better illustration of the microstrip to E-SIGW line transition. One of the advantages of this transition is that both microstrip and E-SIWG lines are printed on the same thin-grounded substrate, and the microstrip line can easily connect to the E-SIGW structure by extending the upper layer. Since the microstrip line excitation is well defined in the simulators, the E-SIGW can also be correctly excited in this method. However, each simulation run takes more time than the first method because of the microstrip line simulation, open free space has to be considered and calculated in the model. The reflection and transmission coefficient responses of the back-to-back transition from microstrip line to E-SIGW line are plotted in Fig. 5-24 by adjusting both line widths for $50\ \Omega$ characteristic impedance.

5.3.3 Horn Design

The integrated H -plane horn antenna introduced here can be designed through conventional H -plane horn formulation given in [73] to reach an optimum directivity of the antenna. However, the

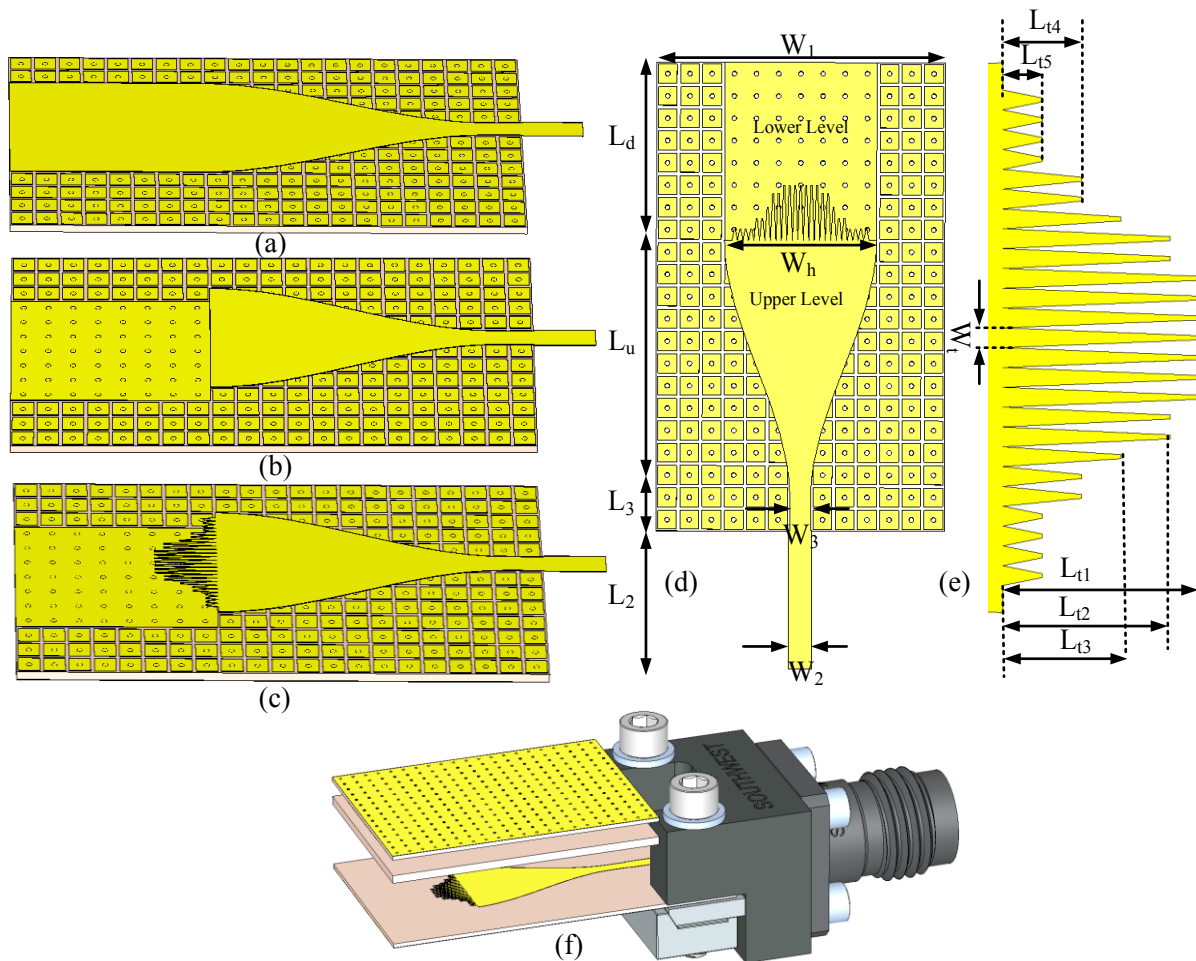


Fig. 5-25. (a) Single level horn (b) Double level horn (c) Double level horn with transition (d) geometry and design parameters of proposed double level horn (e) Magnified transition between the layers (f) 3D View of the stacked layers of the horn with the end launch connector.

boundary condition at the radiating aperture of this horn would be different than that of conventional H -plane horn antennas, because instead of having metallic walls of the rectangular waveguide horn or metallic vias of the SIW horn to confine the horn aperture, periodic cells around the horn open end would define lateral borders of the radiating aperture. Accordingly, the PEC boundary condition of the traditional horns would be evolved to the PMC-like boundary condition of the lateral walls.

After adjusting the right impedance of the E-SIGW to be correctly excited with the microstrip line, the horn tapering can be printed in continuation of the 50Ω E-SIGW line on the same

substrate. Instead of the rectangular waveguide or SIW to feed the H -plane horn with TE_{10} mode, the E-SIGW line with the quasi-TEM mode is feeding the H -plane horn. One significant difference between this type of horn and the others is that the printed tapering of the horn can be profiled easily and accurately to correct the aperture phase. As shown in Fig. 5-25a, immediately after SIGW line the horn tapering starts and continues until reaching the desired aperture width. Eventually, the microstrip line, E-SIGW line, and the horn profile are all printed on the lower side of the thin upper substrate.

One of the advantages of the RGW structures is their capability of supporting wave propagation on the different ridge heights in the same periodic structure, which has not been considered so far. In the horn given in Fig. 5-25(a), the horn printed profile is continued till the aperture at the same level of the E-SIGW line, which ends up with a thin radiating aperture of the horn with the same thickness of the feed line. However, in the proposed horn of Fig. 5-25 (b), we take advantage of the ridge height flexibility in the gap region between the upper conductor and the periodic structure to transfer the guiding medium of the horn to a different level. Accordingly, after the horn profiled tapering, the rest of the horn is separated and shifted to the same level of the periodic structure. Therefore, the H -plane horn aperture can have a different thickness than its feeding part. As such, the horn is fed by planar transmission line on a thin substrate and finally ends up with the thicker radiating aperture by transferring propagation medium from the E-SIGW level to the thicker level. The profiled tapering of the horn can be printed accurately on the upper substrate with thinner thickness to deliver the phase corrected waves to the thicker layer of the horn till the aperture

The second H -wall (lower level) of the horn is printed on the same level of the periodic structure to reach a maximum distance from the upper conductor. However, it could be placed on any other level between the periodic structure and the upper ground plane. Unlike conventional substrate integrated horns in which the aperture is confined with the substrate thickness of the feed line, the present design provides the radiating aperture three times thicker than the planar feed line. Therefore, the aperture thickness of the integrated H -plane horn is not limited to the feed substrate thickness, which is one of the strongest benefits of E-SIGW horn over the conventional SIW horns.

Since the second level of the horn is printed among the periodic patches of the unit cells, it is preferred to be continued straight with the same width provided by upper level and without any

tapering in order not to disturb the periodicity of the unit cells. Under the lower conductor of the horn, plated vias are continued to prevent any parallel plate mode with the lower ground plane.

The double level horn in Fig. 5-25(b) shows much better performance than single level horn in terms of impedance bandwidth. But, to widen the bandwidth and improve the coupling among the horn levels, applying a transition between the layers of the horn could be helpful. A simple tapered transition added to the end of the upper layer could be the easiest solution. However, as the lower conductor of the horn starts immediately after the upper ending, adding a solid piece of the conductor to the upper end, as a transition, covers a considerable part of the lower conductor. Overlapping two pieces of solid conductors inside the horn medium provides a parallel plate cavity region, which causes standing waves under the transition. To overcome this issue, instead of solid transition, a dentate transition with small tapering sections is applied to the end of the upper level as shown in Fig. 5-25(c). Moreover, using dentate transition with small tapering sections results in a shorter length of the whole transition comparing with the solid transition. In Fig. 5-25(d), the design parameters of the E-SIGW double level horn are given, and Fig. 5-25(e) shows the

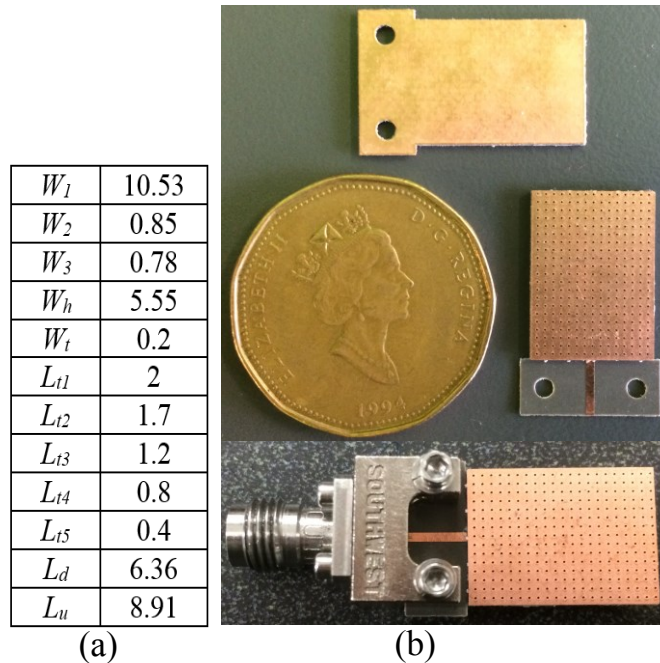


Fig. 5-26. (a) Table of the antenna parameters (unit: mm) (b) The fabricated prototype fed by the end-launch connector.

magnified transition in which fine-tuning of the lengths of different sections provide the antenna with a wider impedance bandwidth.

The whole antenna structure includes three substrate layers. The lower layer is an RT6002 with a thickness of 10 mils that carries the patch-via an array of periodic structure and the lower conductor of the horn. The middle 20-mil-thick RT5880, which is a conductor-less dielectric slab and can be called a spacer between the horn levels. The upper 10-mil thick RT5880 substrate layer with the solid ground plane that contains the printed horn tapering with the transition, which is extended to support the microstrip feed line. The 3D view of the horn with the feeding connector is shown in Fig. 5-25(f). The substrate layers on the periodic structure could be chosen from different types, which obviously would change the bandgap region. However, for this application, it is necessary to choose both upper substrates with close dielectric constants to have almost similar propagation constant in both layers. All the dimensions of the structure are given in table inserted in Fig. 5-26.

5.3.4 Antenna Results and Modifications

The E-SIGW horn antenna and its periodic structure and unit cell are designed and simulated using CST Microwave Studio software. The antenna is fed by 1.85 mm end launch connector, which excites 50 Ω microstrip line on the thin upper substrate layer, but the antenna ends up with three times thicker aperture, as shown in Fig. 5-25. A prototype of the antenna is fabricated using multilayer PCB technology. The layers are firstly processed and stacked together on the final stage. The fabricated prototypes of the proposed double level integrated H -plane horn with connector is shown in Fig. 5-26(b). The antenna is designed to operate in the millimeter wave frequency band around 60 GHz. But it can be simply modified for the higher or lower frequency bands. The main challenge is to adjust the band gap of periodic structure at the desired frequency band of the horn.

In Fig. 5-27, the simulated and measured reflection coefficient results of the E-SIGW double level H -plane horn are compared with the single level horn in Fig. 5-25(a) and the double level horn without a transition in Fig. 5-25(b). As seen from this comparison, adding the second level to the horn improves the antenna matching response, and the transition between the double level horn layers widens the impedance bandwidth of the antenna considerably. At the design stage, the

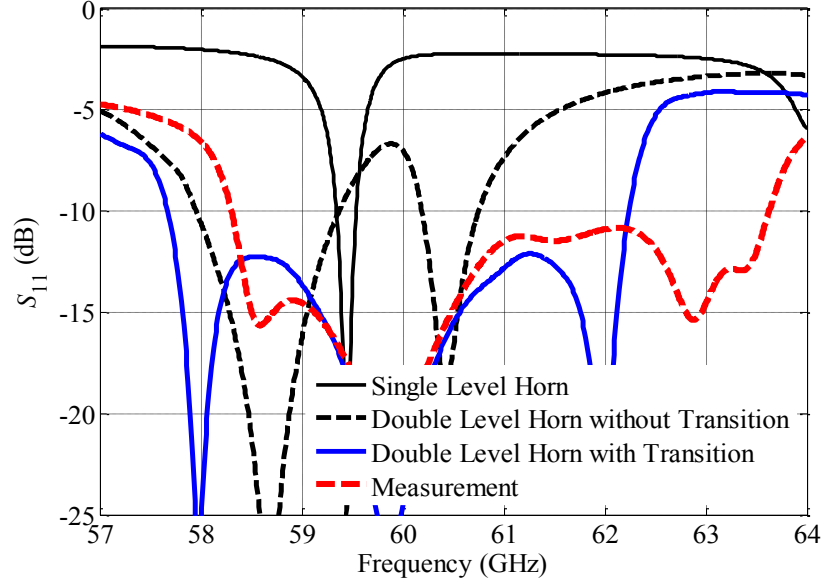


Fig. 5-27. Simulated and measured reflection coefficient responses of the E-SIGW horns.

parameters of the antenna are adjusted to set the operating frequency of the horn around the unlicensed industrial-scientific-medical (ISM) band from 57 to 64 GHz. The fabricated prototype shows an almost 1 GHz shift in the reflection coefficient response, which still operates within the required band. This discrepancy could be because of fabrication tolerances; besides, the layers of the fabricated horn are stacked and adhered together by glue that has an almost 5-micrometer thickness with the dielectric constant around three. The effect of this glue is not included in the simulated model, which could be the other cause of this frequency shift. Both simulated and measured reflection coefficients show almost 8% of bandwidth around the center frequency.

The electric field distribution at different levels of the horn is shown in Fig. 5-28 at 60 GHz. The double level functioning of the horn interior and the limiting feature of the periodic structure around the horn boundary is easily apparent from this illustration of the electric fields inside. After the serrated tapered transition from upper (thin) to lower level, the wave propagation that is delivered to the thicker horn layer is prohibited from leaking under the first layer conductor by the continued periodic structure under the upper (thin) layer. As seen from the field propagation, the minimum amount of the fields is accumulated under the transition because of its dentate geometry. At the beginning of the periodic structure where the microstrip line is connected to the E-SIGW

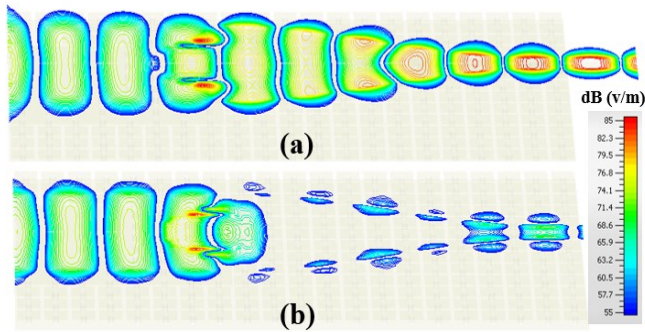


Fig. 5-28. Electric field distribution inside the horn at 60 GHz, (a) At upper thin layer (middle of h_1), (b) At lower layer (middle of h_2).

line, the fringing fields that continued from the microstrip line are somehow strong on the first rows of the periodic structure and decay as they move forward.

As mentioned, the microstrip feed line is excited by an end launch connector, to connect the antenna to the standard connectors of the measurement equipment. As the connector is used to measure the antenna performance, the microstrip line can be extended to reach the connector feed point. However, in real applications, the antenna will be integrated with the RF circuits, which could be directly connected to E-SIGW line. The size of this connector is comparable to the antenna size at the operating frequencies. Therefore, it could have some effects on the antenna radiation pattern. The radiation patterns and the antenna gain are measured in a compact range anechoic chamber, as shown in Fig. 5-29, produced by MI Technologies. In the measurement setup

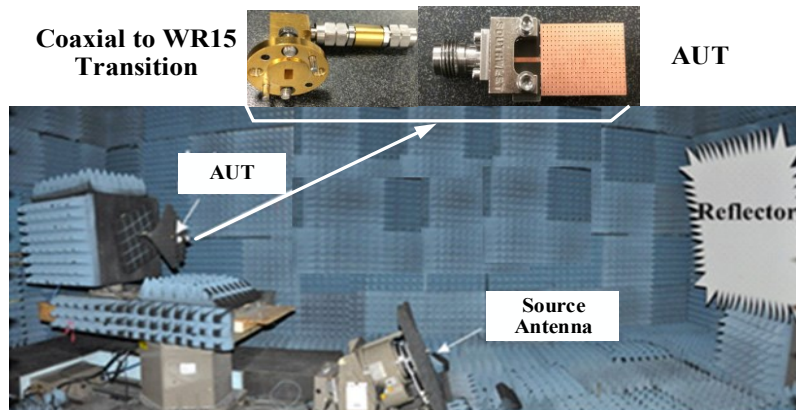


Fig. 5-29. Radiation pattern and gain measurement setup. The end launch connector of the antenna is covered with high frequency absorbing material.

of this anechoic chamber, a horn antenna is located at the focal point of a reflector, which illuminates the antenna under test with plane waves by reflecting the spherical waves from the transmitting horn. The measured and simulated radiation patterns of the horn are given in Fig. 5-30 at three frequencies within the common band of the simulated and fabricated antenna. The geometry of the horn is not symmetric in the E -plane. Therefore, a degree of tilt in the E -plane is expected, which is common in substrate integrated H -plane horns, especially when the planar

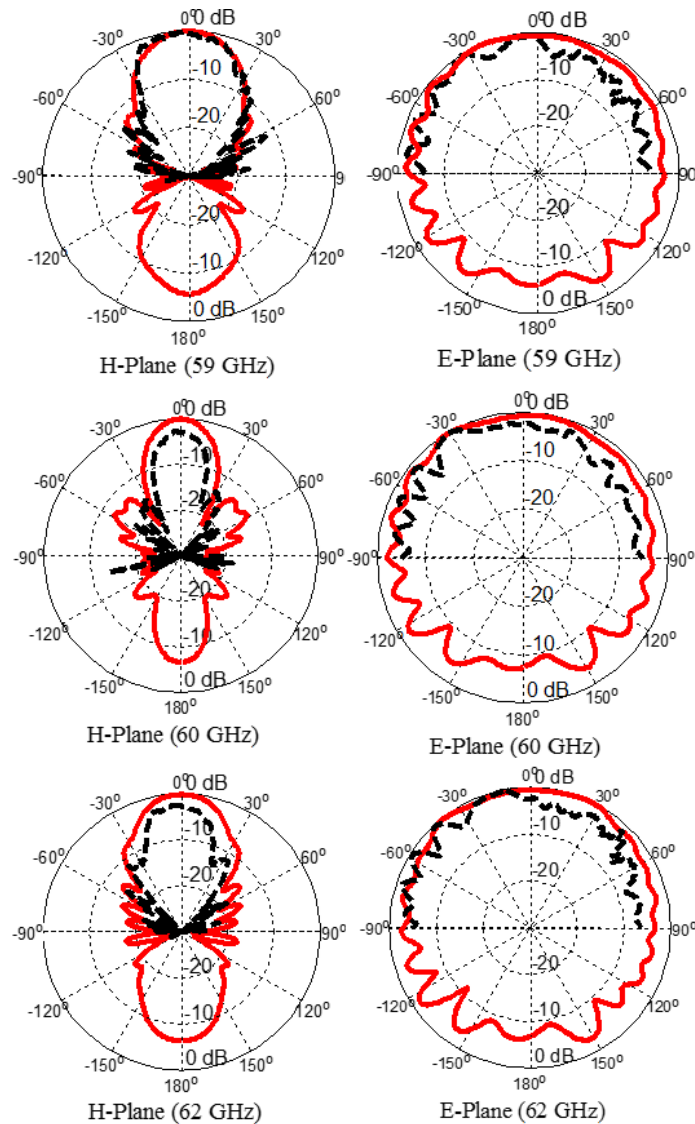


Fig. 5-30. Simulated (red lines) and measured (with covered connector, dashed black lines) radiation patterns of the E-SIGW horn.

transmission line feeds them. In the simulation, the antenna is excited by a wave port connected to the microstrip line and the radiation patterns are extracted.

The outer conductors of the horn are supporting waves strongly to travel to backward direction. That is because these conductors behave as hard surface for the aperture wave polarization. As the volume of the feeding conductor is substantial at the antenna operating frequency, it causes high reflection of back traveled waves on the outer surface, which affects the symmetry of the E -plane main beam unexpectedly. This asymmetry is observed in the first hand measurements. To be sure of the cause, the end launch connector is also introduced in the full-wave simulation, and the antenna radiation patterns are realized by the full-wave simulation when the antenna structure is

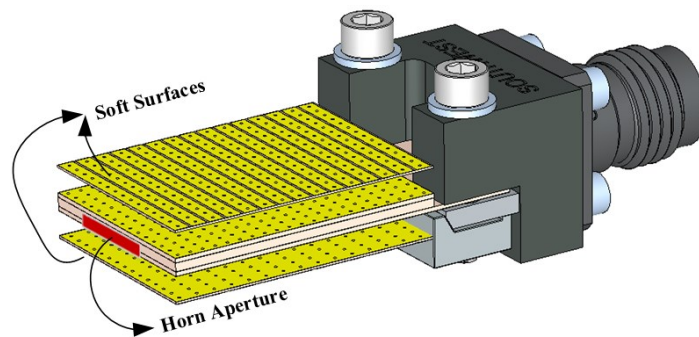


Fig. 5-31. Connector fed E-SIGW horn covered by a couple of strip-via soft surfaces.

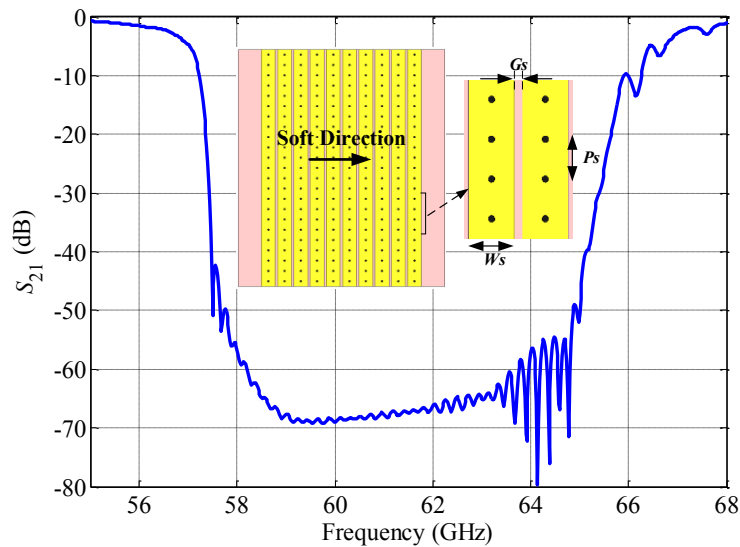


Fig. 5-32. Geometry and transmission coefficient of the designed strip-via soft surface for the antenna frequency band ($W_s = 0.7$, $G_s = 0.15$, $P_s = 0.8$ mm).

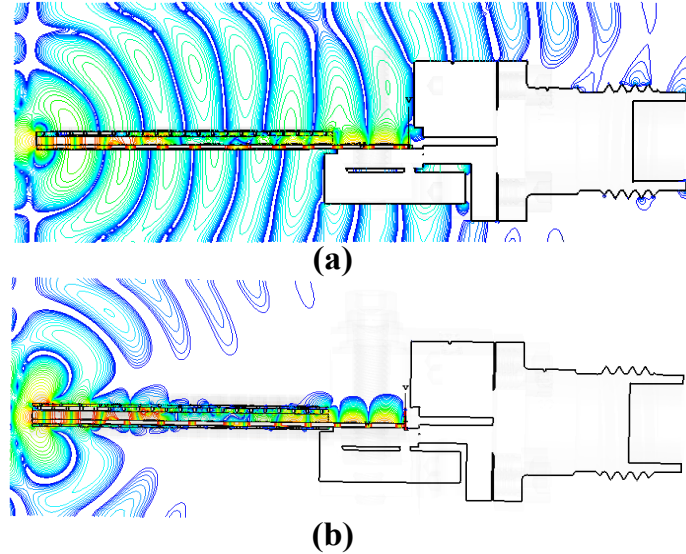


Fig. 5-33. Electric field distribution around the connector fed E-SIGW horn at 60 GHz (a) Without soft surfaces (b) With soft surfaces.

simulated in the presence of the end connector. Sure enough, what was observed in the measurements is repeated in the simulation. Therefore, in order to minimize the connector effect on the antenna radiation pattern, the connector is covered competently with thin and broadband high frequency absorber in the measurement process, as shown in Fig. 5-29.

Some possible ways to reduce the effect of the bulky connector or the transitions is to elongate the microstrip line between the connector and the E-SIGW line or to extend the E-SIGW line between the microstrip line and the horn. By these ways, the metal connector would be away from the radiating aperture and have smaller interaction. The other method is to reduce the waves propagating towards the connector and any back transitions. This can be performed by changing the outer surface from hard to soft as described in the previous section. As seen from the simulated radiation patterns in Fig. 5-30 the horn has high back radiation, which is caused by the surface waves supported by the outer conductors as explained above. These back directed waves also interact with the feeding connector and disturb the horn radiation pattern. Applying the soft surfaces around the horn aperture suppresses the back radiating waves. A couple of strip-via soft surfaces, which are designed to have stopband covering the horn operating frequency are employed, as shown in Fig. 5-31. The design procedure of the strip-via soft surface for any desired

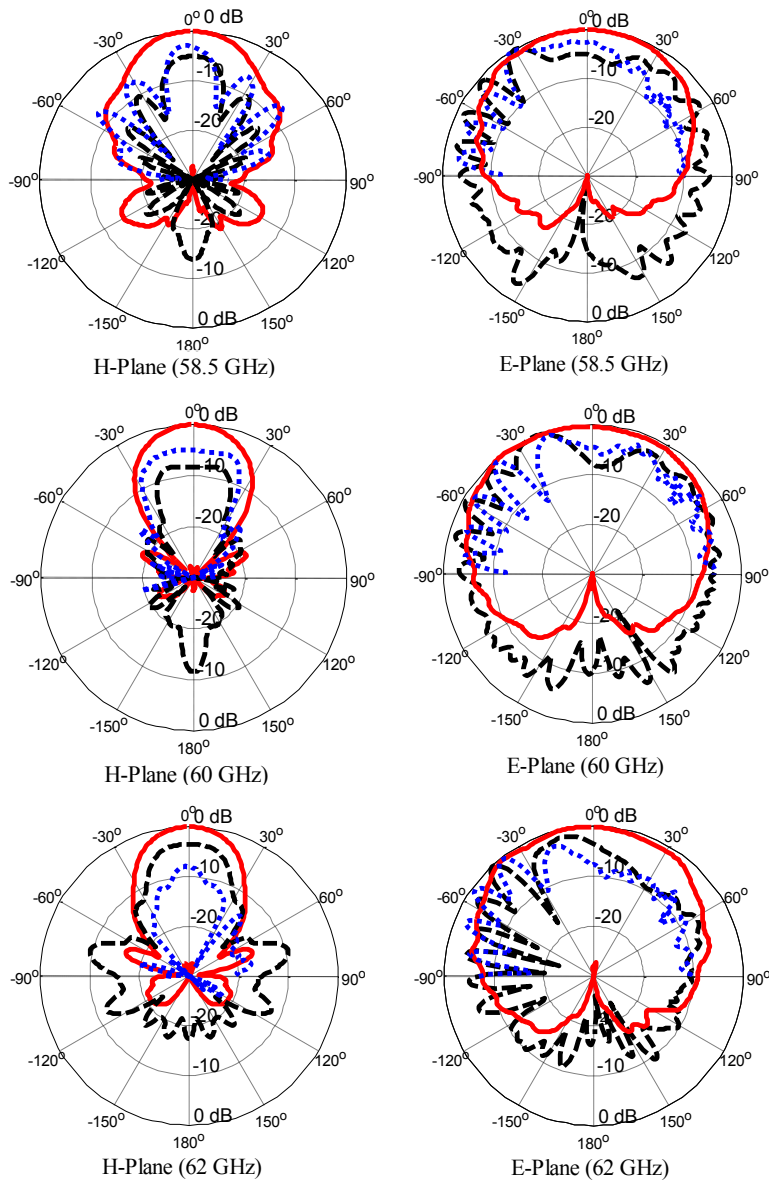


Fig. 5-34. Connector fed E-SIGW horn with soft surfaces (red solid lines, simulation) and without soft surfaces (black dashed lines, simulation; blue dotted line, measurement).

frequency band is explained before in this chapter. In Fig. 5-32, the geometry of this strip-via soft surface designed for the frequency around 60 GHz and its stop bandwidth when it is excited in the soft direction are shown. The surface parameters including the strip width (W_s), the gap between the adjacent strips (G_s), and the metallic via positioning (P_s) are designed based on the stop band

frequency and the substrate parameters (thickness and dielectric constant), which is the 5-mil-thick RT6002 laminate.

In Fig. 5-33, the electric field distribution around the horn equipped with a couple of soft surfaces is compared with the same horn without these surfaces in the presence of the feeding connector. As seen from this comparison, the strip-via surface around the horn stops the waves propagating in the backward direction and eliminates the strong interaction with the connector. As a result, the antenna forward radiation pattern is not disturbed. In Fig. 5-34, the simulated and measured radiation patterns of the proposed E-SIGW H -plane horn, which is fed by end launch connector, are compared when it is sandwiched between a couple of soft surfaces. As seen from the dashed black line (simulation) and dotted blue line (measurement) radiation patterns, the presence of the bulky connector destroys the horn radiation pattern symmetry in the E -plane when it is compared with the antenna pattern without connector (red line patterns in Fig. 5-30). It also causes the H -plane pattern to have higher sidelobe levels. The simulated radiation patterns of the horn fed by the connector and equipped with the soft surfaces are also plotted with a solid red line in Fig. 5-34. The STOP region [65] provided by the strip-via soft surfaces around the horn separates the aperture area of the horn from the back circuitries and enables the antenna radiation

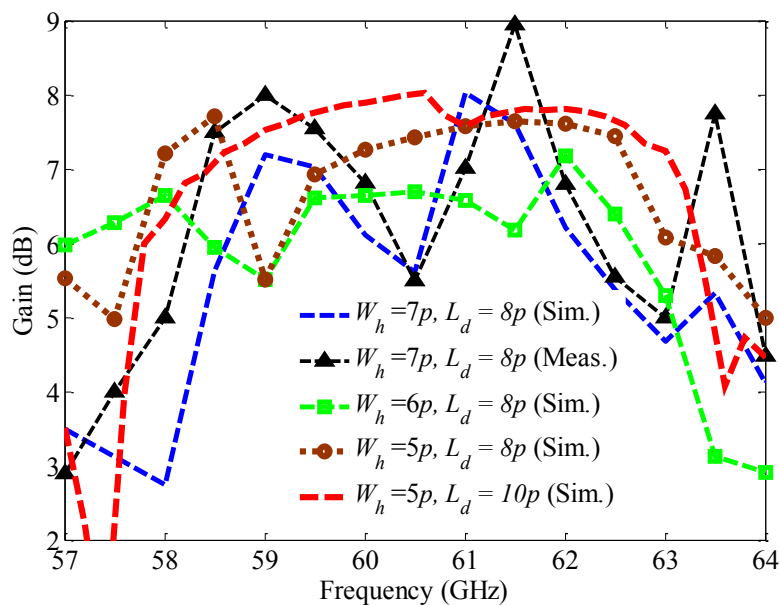


Fig. 5-35. Measured and simulated gain performance of the horn ($p = 0.87$ mm, periodicity of the unit cell).

pattern to be only derived from the radiating aperture. Therefore, the symmetry of the antenna pattern especially in the E -plane is not disturbed even in the presence of the bulky connector and the horn demonstrates almost symmetric radiation patterns. In addition, it reduces the edge diffraction around the aperture and eliminates all the ripples of the radiation patterns in the E - and H -plane as well as reduced the back radiation.

In Fig. 5-35, the simulated peak gain of the horn at the operating frequency band is compared for different values of W_h and L_d including the measured gain of the first design. The measured gain of the fabricated prototype is almost in agreement with its simulated gain, which is indicated with the dashed blue line. However, this design has a gain drop because of its aperture phase error around 60 GHz. By modifying the horn design with these two parameters, the phase error is corrected, and a stable gain performance is achieved over the bandwidth. The gain of the corrected design is plotted in red dashed line.

5.3.5 Millimeter-Wave Contactless Multi-Layer Air-Filled H -plane SIW Horn

In Chapter 3, a new configuration of air-filled SIW was introduced, which enables the waveguide layers to be stacked on top of each other without a need to the layer electrical connections. This was achieved by changing the boundary condition around the air-filled medium on the intermediate substrate from a PEC to an AMC. Thus, a stop band region was created between the AMC surface and the covering PEC lids of the air-filled waveguide. The PEC-AMC parallel plate stop band region around the guiding medium suppress any leakage of the waves from any possible tiny air gap that might exist if the layers are not electrically connected. Such a case is advantageous at millimeter wave frequencies where assuring electrical contact is not possible or would be very expensive.

The proposed technique can be used to design multilayer integrated H -plane horn at the millimeter frequencies. As mentioned before, in the conventional SIW horn antennas the thickness of the aperture is limited to the thickness of the planar feed line, which is not supposed to exceed certain values to assure no radiation from the feed line. As a result, only a limited impedance bandwidth is possible due to the thin substrate. In the previous section, an innovative design of the integrated horn based on elevated substrate integrated gap waveguide (E-SIGW) configuration has

been introduced, which allowed the horn to be three times thicker than its planar feed line. For this configuration, the horn layers and the periodic structure were stacked and fixed firmly with epoxy glue in the fabrication process. Here, by taking advantage of the proposed contactless air-filled SIW technology, a new design of the integrated H -plane horn is introduced, which enables the traditional SIW horn to be air-filled and implemented by stacking several layers.

The geometry of the proposed configuration of the horn based on contactless air-filled SIW is shown in Fig. 5-36. In this design, the SIW horn is composed of five separated layers. As the design is based on contactless air-filled SIW, the horn layers can be mounted on top of each other without any necessary electrical contacts. In other words, unlike the previously mentioned multi-layer integrated horns, the layers of this horn can be fabricated and processed separately and connected with regular screws without worry about leaking waves between the layers. The middle layer is a thin substrate suitable for the planar feed line operating at high frequency. For this horn,

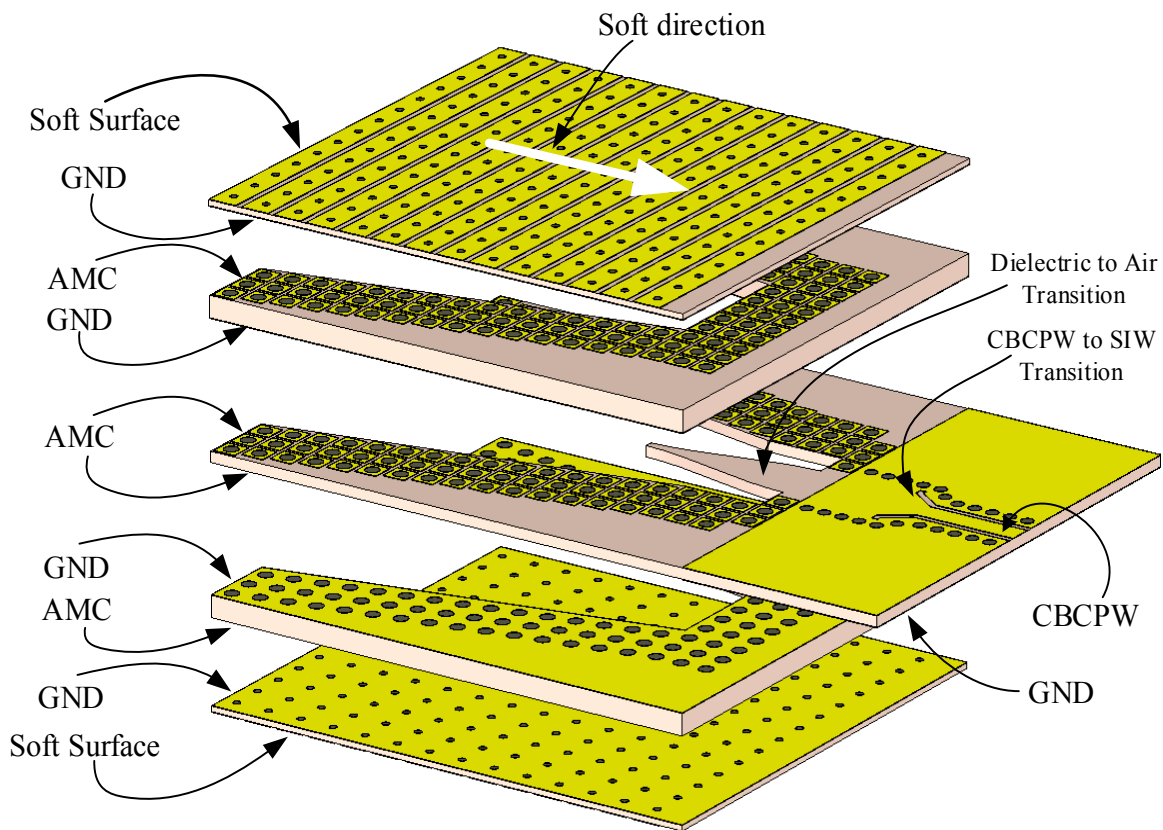


Fig. 5-36. Geometry of the proposed air-filled contactless SIW horn.

the thin middle layer is extended to support CBCPW line and its transition to SIW. Around the air-filled cut of the middle layer, the periodic structure of the contactless air-filled SIW including double patch unit cell, as described in Chapter 3, are utilized. This periodic structure prepares AMC surfaces on both sides of the middle layer. Based on the substrate thickness and frequency of operation the cell design can be modified to have a stop band in the desired frequency band. The modified unit cell of the middle layer of the contactless SIW is shown in Fig. 5-37 with its dispersion diagram by considering a possible gap of 15 micrometers with the PEC lids.

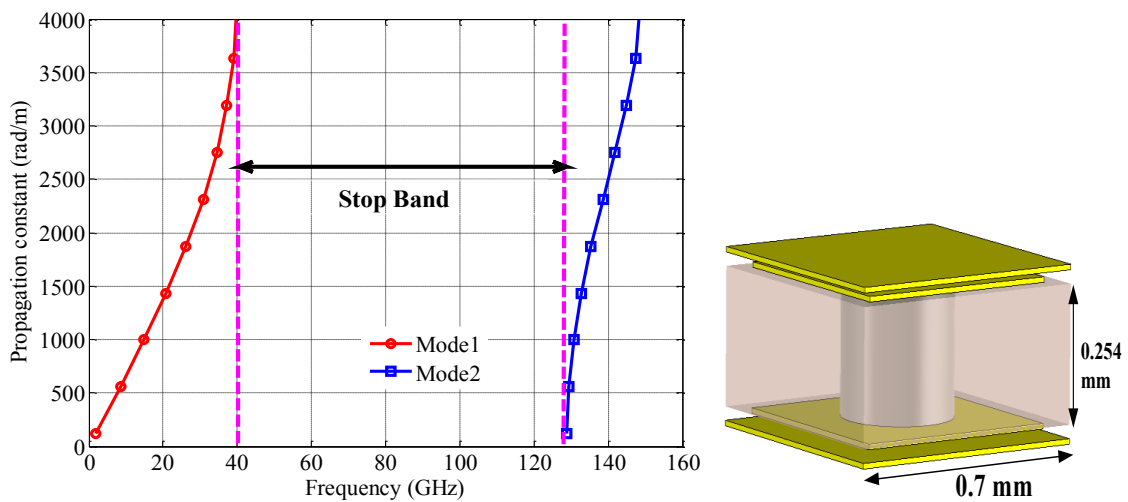


Fig. 5-37. Contactless SIW horn unit cell for middle thin layer with dispersion diagram.

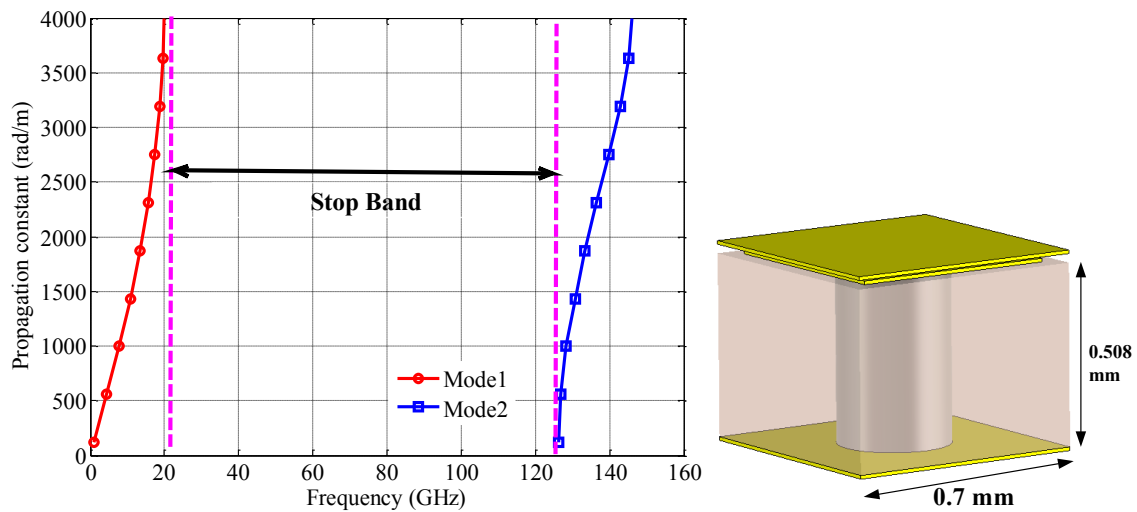


Fig. 5-38. Contactless SIW horn unit cell for around thick layers with dispersion diagram.

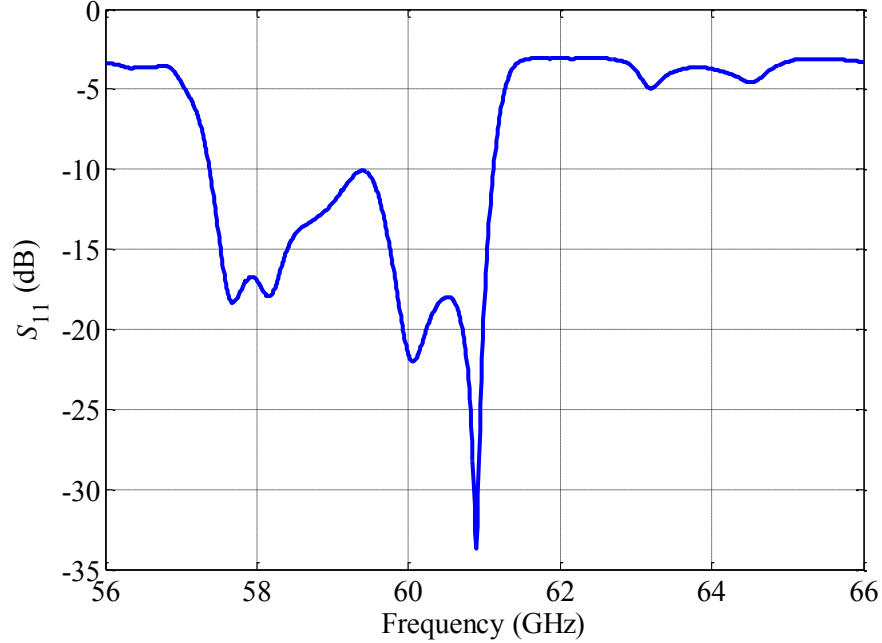


Fig. 5-39. Simulated reflection coefficient of the multi-layer contactless air-filled SIW horn with 15 μm gap between the layers.

To increase the radiating horn aperture, two thicker air-filled layers are added to sandwich the main thin layer. These two layers are equipped with a grounded periodic structure around the air-filled region, which realize a single side AMC slab. The unit cell geometry and the dispersion diagram indicating the stop bandwidth of the periodic structure of this cell are shown in Fig. 5-38. The complete ground of the thick layers would make PEC-AMC parallel plate when they are meeting the middle layer of the double side AMC surfaces. Therefore, any leaking waves would be suppressed from the gaps between the layers and they can be placed easily on top each other with any rudimentary connection.

Two other covering lids are also needed to cover all the three air-filled layers of the horn to close the horn medium. The outer AMC surfaces of the thick air-filled layers would provide stop band region for the leaking waves when PEC lids cover them. For simplicity in the PCB based circuits, two regular grounded substrates can be used to hold the covering PEC lids on the top and bottom of the horn. By taking advantage of these two unused substrate layers, a couple of strip-via soft surfaces are applied on the upper and lower covering layers to suppress back traveling waves

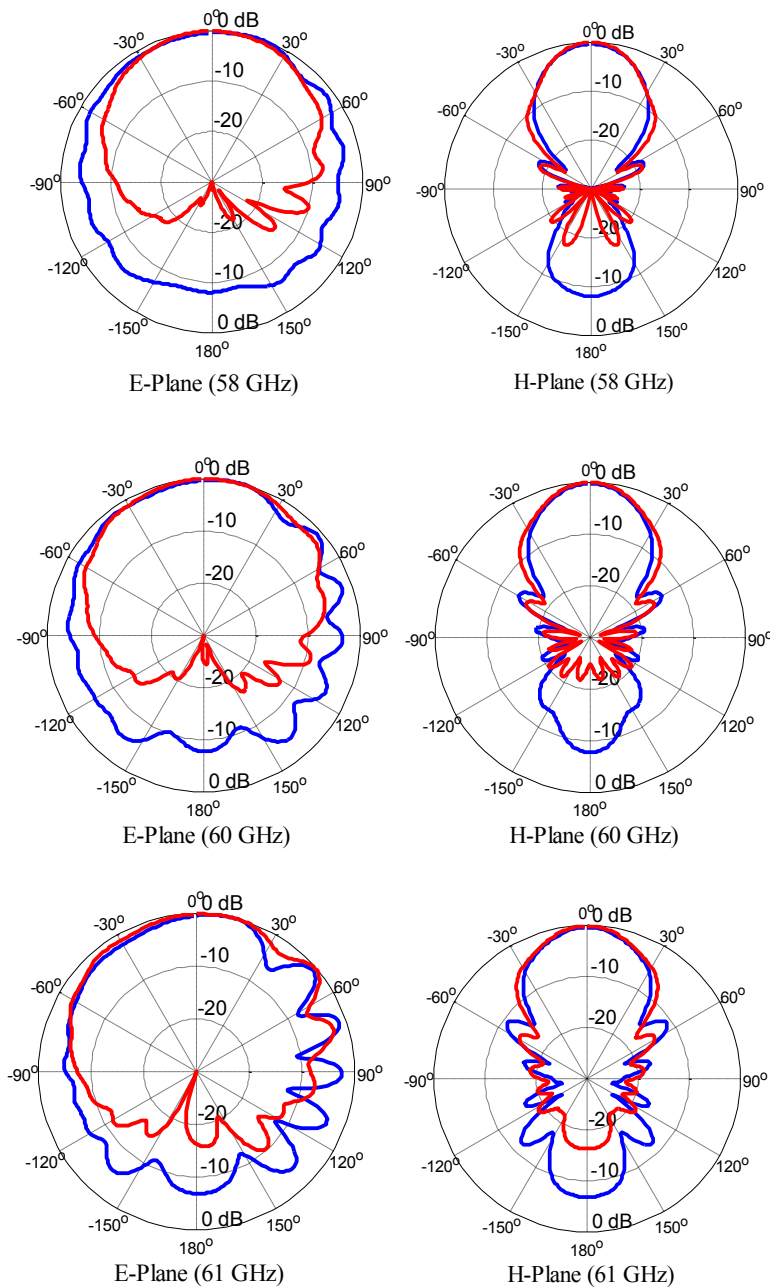


Fig. 5-40. Simulated radiation patterns of the contactless air-filled SIW horn with soft surfaces (red line) and without soft surfaces (blue line).

from the aperture. The tapered dielectric to air transition at the end of dielectric filled SIW in the middle layer is utilized to smooth the transition and widen the antenna impedance bandwidth. The simulated reflection coefficient response of the designed horn is given in Fig. 5-38. The thick radiating aperture and the extended dielectric to the air transition at the horn throat are utilized to

improve the antenna matching bandwidth. The antenna simulation is performed considering 15 μm gap between the layers, which is the estimated possible gap between the stacked substrate layers, as measured in Chapter 3. The simulated radiation patterns of this horn at three frequencies are plotted in Fig. 5-40 in E - and H -planes of the horn with and without soft outer surfaces. The strip-via soft surfaces around the horn aperture reduce the antenna back radiation considerably by suppressing the back propagating waves and isolate the antenna aperture from back circuitries.

5.4 Conclusion

In the first section, the substrate integrated H -plane horn antenna implemented on the high dielectric constant material with parallel transitions has been introduced. The H -plane horn aperture has been loaded with a couple of parallel transitions through a long transverse slot on both sides of the antenna aperture. It has been shown that the depth of the transitions determines the matching frequency band resulting from adding transitions. The proposed transitions for the substrate integrated H -plane horn do not increase the antenna length, unlike previously introduced transitions for this antenna. Since the open parallel transitions are functioning as chokes around the horn aperture, they have considerably reduced the antenna back radiations.

Because the conventionally integrated horn aperture is surrounded by the metallic walls, its aperture ends up with a completely tapered electric field distribution that limits the aperture efficiency. In other words, the H -walls are supporting the dominant mode; but the E -walls are suppressing this mode. The only parameter that could improve the efficiency of the integrated horn antenna is the aperture width since the height is fixed to the substrate thickness. However, widening the aperture does not considerably affect the efficiency when the horn length is kept the same so that for a particular geometry, the antenna efficiency cannot exceed a certain value. Applying hard boundary condition to the horn E -walls have corrected the tapered nature of the conventional aperture by increasing the transverse wall reactance. The hard horn has been realized by an air-filled integrated horn with a thickness of the high dielectric constant substrate on the E -walls. In addition, instead of the straight horn tapering, the hard E -walls have been profiled to correct the aperture phase of the horn. As a result, almost uniform amplitude and phase distributions of the horn aperture have been achieved with a considerably improved aperture

efficiency. To suppress the backscattered fields from the aperture, a couple of soft surfaces with the stop band at the antenna operating bandwidth have been designed to cover the horn H -walls, in order to change their boundary condition from hard to soft for the aperture waves. The soft surface layers considerably suppressed the high back radiation of the integrated horn, particularly in the center frequency of the soft surface stop band. Meanwhile, the depleted horn substrate has been covered by the solid ground plane of the soft surfaces. Furthermore, the regular substrate-air discontinuity of the integrated H -plane horn has been moved to the horn throat where the well-designed tapered transition has provided the antenna with the matching bandwidth.

A new configuration of the H -plane horn antenna at the millimeter-wave frequencies has also been introduced that enables the integrated horn to be fed with thin feed line while having a thick radiating aperture. By taking advantage of multi-layer PCB technology, the E-SIGW with the three-layer unit cells in its periodic structure has been designed and excited by a thin microstrip line. The advantage of using E-SIGW for the H -plane horn design is to reach to a possibility of having a multi-level configuration of the horn interior. Having multi-level configuration for the H -plane horns is most helpful at the millimeter-wave frequencies since it enables the integrated horn antenna to be fed by a thin feed line and finally, ends up with a thick aperture. In the presented design, the H -plane horn antenna has been excited by a 10-mil-thick feed line and reached for the three-time thicker aperture. The E-SIGW configuration also has enabled the H -plane horn antenna at millimeter-wave frequencies to eliminate the need for the SIW configuration, which has more limitations in feeding with planar lines at higher frequencies; besides forces the antenna to have the same aperture thickness as the feed line. In the proposed horn, tapered transitions between the layers have been applied to improve the coupling of the traveling waves between the horn layers that provide the substrate integrated H -plane with wider matching bandwidth, without any necessity for the extra transition to appease the indigenous dielectric-air discontinuity at the radiating aperture. The measured reflection coefficient response of the antenna has agreed with the simulation in the large area of the bandwidth. As the horn aperture surrounded by outer hard surface (conductor surface), the back propagating waves have caused strong interaction with the bulky connector that destroyed the symmetry of the E -plane main beam. By replacing the hard surface with a soft surface that is realized by transverse strips grounded by conducting vias, the

antenna radiating aperture has been isolated from the feeding circuitries. Therefore, the antenna far field patterns have been only affected by the main horn radiating aperture and have not been interrupted by the feeding components. Besides, a considerable reduction has been achieved in the antenna back radiations since the aperture waves have been prevented from traveling backward. Isolating the radiating aperture from the other parts of the antenna or the feeding circuits is more advantageous at the millimeter wave frequencies because the volume of the feeding components is more comparable with the wavelength, which disturbs the antenna performance.

Finally, based on contactless air-filled SIW proposed in Chapter 3, a multilayer configuration of integrated H -plane horn has been presented. The given configuration has enabled the antenna layers to be stacked on top of each other without a need for electrical contacts at the millimeter wave frequencies. The contactless multi-layer configuration has helped the antenna to be fed by the thin transmission line while having a thick radiating aperture. The planar strip-via soft surface added to the outer antenna surface stops the back propagating waves that cause a reduction in the back lobe level.

Chapter 6

CONCLUSION AND FUTURE WORKS

6.1 Conclusions

The thesis presents innovative approaches to improve the efficiencies of the integrated waveguides and antennas at high frequencies. The metamaterial-based gap waveguide technology as an air-filled guiding medium is providing solutions to the problems of the conventional transmission lines at millimeter wave frequencies. However, it has some drawbacks. In Chapter 2, the new configuration of ridge gap waveguide (RGW) has been introduced. This configuration has enabled the RGW to support the TEM mode of the propagation instead of quasi-TEM of the single texture conventional type. Therefore, it was referred to as a TEM-RGW. The TEM propagation has been realized by modifying the symmetry of the RGW transmission medium, which has made the RGW line to behave very close to the ideal parallel plate waveguide. As a result, the characteristic impedance has been easily extracted from the parallel-plate impedance relation. The proposed TEM-RGW has shown a lower insertion loss and higher isolation in comparison with the conventional gap waveguide.

The substrate integrated waveguide (SIW) as a low-cost and compact structure is an alternative solution for many systems. However, due to its intrinsic dielectric filled geometry, it suffers from the dielectric loss problem at millimeter wave frequencies. The air-filled SIW has been recommended to tackle this issue. However, the top and bottom conducting walls have to be in contact with the via side walls. For thick substrate, constraints on the via diameters might make it difficult to be realized. Thus, in Chapter 3, a new layout of the air-filled SIW has been presented to solve this problem. The double sided AMC slab has been firstly realized around the air-filled propagating medium in the given configuration of the air-filled SIW. The AMC surfaces around the air-filled guiding medium provide PEC-AMC parallel plate region when the PEC lids are covering the waveguide. The proposed approach encapsulates the integrated air-filled propagating

medium that is very advantageous at millimeter wave frequencies because it considerably reduces the cost of layers connection.

To propose an efficient and reliable feed line for the contactless air-filled SIW, the partially air-filled configuration of the conductor-backed coplanar waveguide (CBCPW) has been recommended in Chapter 4. This new air-filled planar transmission line, which has the signal line available for the end launch excitation, enables the contactless air-filled SIW to be fed directly by an air-filled transmission line. As this configuration of the CBCPW is novel in the classification of the planar coplanar waveguides, a quasi-static analysis of the proposed line based on conformal mapping has been utilized to reach an approximate design expression of the characteristic impedance for the different thickness of the layers.

The substrate integrated H -plane horn antenna is one the simplest and widely used product of the SIW technology. This antenna as a member of the traditional waveguide horn antennas has lots of potentials to be integrated with the RF circuits. However, it has encountered with various inherent problems. In Chapter 5, four new designs of this antenna have been introduced in order to improve the performance of this antenna to be more efficient and applicable at high frequencies. These improvements include widening the matching bandwidth, making the aperture distribution uniform, suppressing back radiations, decreasing feed line radiation, and introducing contactless multi-layer configurations.

6.2 Future works

As mentioned, the proposed configuration of TEM-RGW represents better performance in terms of insertion loss, isolation, and characteristic impedance variations compared to the conventional RGW configuration. Therefore, a variety of microwave components, which have been already designed with conventional RWG, can be redesigned with TEM-RGW with better performances. In addition, the high isolation of the TEM-RGW lines allows the adjacent lines to be closely located with minimum interaction so that a compact and low loss feed network for an antenna array can be easily designed with this technology.

Numerous low loss high-frequency components can also be designed with the proposed contactless air-filled SIW. As the problem of the layers contact has been solved at millimeter frequencies by the proposed solution, different multi-layer configurations of the microwave components can be easily implemented. In addition, since many other non-reciprocal devices such as phase shifters and duplexers can also be designed with this technology, a highly efficient and low-cost full link operating at millimeter wave frequencies can be implemented through the contactless air-filled SIW.

REFERENCES

- [1] M. Tsuji, H. Shigesawa, and A.A. Oliner, "Simultaneous Propagation of bound and leaky dominant modes on printed-circuit lines," *IEEE Trans. Microw. Theory and Tech.*, vol. 43, no. 12, pp. 3007-3019, Dec. 1995.
- [2] F. Mesa, A. A. Oliner, D. R. Jackson, and M. J. Freire, "The influence of a top cover on the leakage from microstrip line," *Microwave Theory and Techniques, IEEE Transactions on*, vol. 48, pp. 2240-2248, 2000.
- [3] W. E. McKinzie and N. Alexopoulos, "Leakage losses for the dominant mode of conductor-backed coplanar waveguide," *Microwave and Guided Wave Letters, IEEE*, vol. 2, pp. 65-66, 1992.
- [4] E. Levine, G. Malamud, S. Shtrikman, and D. Treves, "A study of microstrip array antennas with the feed network," *Antennas and Propagation, IEEE Transactions on*, vol. 37, pp. 426-434, 1989.
- [5] G. Six, G. Prigent, E. Rius, G. Dambrine, and H. Happy, "Fabrication and characterization of low-loss TFMS on silicon substrate up to 220 GHz," *Microwave Theory and Techniques, IEEE Transactions on*, vol. 53, pp. 301-305, 2005.
- [6] K. Nishikawa, S. Sugitani, K. Inoue, T. Ishii, K. Kamogawa, B. Piernas, *et al.*, "Low-loss passive components on BCB-based 3D MMIC technology," in *Microwave Symposium Digest, 2001 IEEE MTT-S International*, 2001, pp. 1881-1884 vol.3.
- [7] D. Deslandes and W. Ke, "Integrated microstrip and rectangular waveguide in planar form," *Microwave and Wireless Components Letters, IEEE*, vol. 11, pp. 68-70, 2001.
- [8] X. Feng and W. Ke, "Guided-wave and leakage characteristics of substrate integrated waveguide," *Microwave Theory and Techniques, IEEE Transactions on*, vol. 53, pp. 66-73, 2005.
- [9] W. Ke, "Towards system-on-substrate approach for future millimeter-wave and photonic wireless applications," *Microwave Conference, 2006. APMC 2006. Asia-Pacific*, 2006, pp. 1895-1900.
- [10] M. F. Shafique and I. D. Robertson, "Laser prototyping of multilayer LTCC microwave components for system-in-package applications," *Microwaves, Antennas & Propagation, IET*, vol. 5, pp. 864-869, 2011.
- [11] S. Tze-Min, C. Chi-Feng, T.-Y. Huang, and R.-B. Wu, "Design of Vertically Stacked Waveguide Filters in LTCC," *Microwave Theory and Techniques, IEEE Transactions on*, vol. 55, pp. 1771-1779, 2007.
- [12] P. S. Kildal, E. Alfonso, A. Valero-Nogueira, and E. Rajo-Iglesias, "Local Metamaterial-Based Waveguides in Gaps Between Parallel Metal Plates," *Antennas and Wireless Propagation Letters, IEEE*, vol. 8, pp. 84-87, 2009.

- [13] P. S. Kildal and M. N. M. Kehn, "The ridge gap waveguide as a wideband rectangular hard waveguide," in *Antennas and Propagation (EuCAP), 2010 Proceedings of the Fourth European Conference on*, 2010, pp. 1-4.
- [14] P. S. Kildal, "Three metamaterial-based gap waveguides between parallel metal plates for mm/submm waves," in *Antennas and Propagation, 2009. EuCAP 2009. 3rd European Conference on*, 2009, pp. 28-32.
- [15] P. S. Kildal, "Artificially soft and hard surfaces in electromagnetics," *Antennas and Propagation, IEEE Transactions on*, vol. 38, pp. 1537-1544, 1990.
- [16] A. Valero-Nogueira, E. Alfonso, J. I. Herranz, and P. S. Kildal, "Experimental Demonstration of Local Quasi-TEM Gap Modes in Single-Hard-Wall Waveguides," *Microwave and Wireless Components Letters, IEEE*, vol. 19, pp. 536-538, 2009.
- [17] P. S. Kildal, A. U. Zaman, E. Rajo-Iglesias, E. Alfonso, and A. Valero-Nogueira, "Design and experimental verification of ridge gap waveguide in bed of nails for parallel-plate mode suppression," *Microwaves, Antennas & Propagation, IET*, vol. 5, pp. 262-270, 2011.
- [18] A. U. Zaman, P. S. Kildal, M. Ferndahl, and A. Kishk, "Validation of ridge gap waveguide performance using in-house TRL calibration kit," in *Antennas and Propagation (EuCAP), 2010 Proceedings of the Fourth European Conference on*, 2010, pp. 1-4.
- [19] A. Valero-Nogueira, M. Baquero, J. I. Herranz, J. Domenech, E. Alfonso, and A. Vila, "Gap Waveguides Using a Suspended Strip on a Bed of Nails," *Antennas and Wireless Propagation Letters, IEEE*, vol. 10, pp. 1006-1009, 2011.
- [20] E. Rajo-Iglesias and P. S. Kildal, "Groove gap waveguide: A rectangular waveguide between contactless metal plates enabled by parallel-plate cut-off," in *Antennas and Propagation (EuCAP), 2010 Proceedings of the Fourth European Conference on*, 2010, pp. 1-4.
- [21] Bernardo-Clemente, "Groove Gap Waveguides: A contactless solution for multilayer slotted-waveguide array antenna assembly," in *2016 10th European Conference on Antennas and Propagation (EuCAP)*, 2016, pp. 1-4.
- [22] A. U. Zaman and P. S. Kildal, "Wide-Band Slot Antenna Arrays with Single-Layer Corporate-Feed Network in Ridge Gap Waveguide Technology," *Antennas and Propagation, IEEE Transactions on*, vol. 62, pp. 2992-3001, 2014.
- [23] A. U. Zaman and P. S. Kildal, "Slot antenna in ridge gap waveguide technology," in *Antennas and Propagation (EuCAP), 2012 6th European Conference on*, 2012, pp. 3243-3244.
- [24] A. Farahbakhsh, D. Zarifi, A. U. Zaman, and P. S. Kildal, "Corporate distribution networks for slot array antenna based on groove gap waveguide technology," in *2016 10th European Conference on Antennas and Propagation (EuCAP)*, 2016, pp. 1-3.

- [25] A. J. Sáez, A. Valero-Nogueira, J. I. Herranz, and B. Bernardo, "Single-Layer Cavity-Backed Slot Array Fed by Groove Gap Waveguide," *IEEE Antennas and Wireless Propagation Letters*, vol. 15, pp. 1402–1405, 2016.
- [26] A. J. Sáez, A. Valero-Nogueira, J. I. Herranz, and V. M. Rodrigo, "Ring resonances in groove gap waveguides with application to slot array antennas," in *2015 IEEE International Symposium on Antennas and Propagation USNC/URSI National Radio Science Meeting*, 2015, pp. 260–261.
- [27] J. I. H. Herruzo, A. Valero-Nogueira, S. M. Giner, and A. V. Jiménez, "Untilted Narrow-Wall Slots Excited by Parasitic Dipoles in Groove Gap Waveguide Technology," *IEEE Transactions on Antennas and Propagation*, vol. 63, no. 11, pp. 4759–4765, Nov. 2015.
- [28] S. M. Giner, A. Valero-Nogueira, J. I. H. Herruzo, and M. B. Escudero, "Excitation of untitled narrow-wall slot in groove gap waveguide by using a parasitic dipole," in *2013 7th European Conference on Antennas and Propagation (EuCAP)*, 2013, pp. 3082–3085.
- [29] E. Pucci, E. Rajo-Iglesias, and P. S. Kildal, "New Microstrip Gap Waveguide on Mushroom-Type EBG for Packaging of Microwave Components," *Microwave and Wireless Components Letters, IEEE*, vol. 22, pp. 129–131, 2012.
- [30] H. Raza, J. Yang, P. S. Kildal, and E. Alfonso Alos, "Microstrip-Ridge Gap Waveguide: Study of Losses, Bends, and Transition to WR-15," *Microwave Theory and Techniques, IEEE Transactions on*, vol. 62, pp. 1943–1952, 2014.
- [31] M. S. Sorkherizi and A. A. Kishk, "Fully Printed Gap Waveguide With Facilitated Design Properties," *IEEE Microwave and Wireless Components Letters*, vol. 26, no. 9, pp. 657–659, Sep. 2016.
- [32] M. S. Sorkherizi and A. A. Kishk, "Transition from microstrip to printed ridge gap waveguide for millimeter-wave application," in *2015 IEEE International Symposium on Antennas and Propagation USNC/URSI National Radio Science Meeting*, 2015, pp. 1588–1589.
- [33] D. Deslandes and K. Wu, "Single-substrate integration technique of planar circuits and waveguide filters," *IEEE Trans. Micro. Theory Techn.*, vol. 51, no. 2, pp. 593–596, Feb. 2003.
- [34] T. Djerfandi and K. Wu, "Super-compact substrate integrated waveguide cruciform directional coupler," *IEEE Microw. and Wireless Compon. Let.*, vol. 17, no. 11, pp. 757–759, Nov. 2007.
- [35] A. Doghri, A. Ghiotto, T. Djerafi, and K. Wu, "Compact and low cost substrate integrated waveguide cavity and bandpass filter using surface mount shorting stubs," in *Microwave Symposium Digest (MTT), 2012 IEEE MTT-S International*, 2012, pp. 1–3.
- [36] K. Kim and S. Lim, "Miniaturized Circular Polarized TE_n-Mode Substrate-Integrated-Waveguide Antenna," *IEEE Antennas and Wireless Propagation Letters*, vol. 13, pp. 658–661, 2014.

- [37] D. Deslandes and K. Wu, "Design consideration and performance analysis of substrate integrated waveguide components," in *Microwave Conference, 2002. 32nd European*, 2002, pp. 1–4.
- [38] M. Pasian, M. Bozzi, and L. Perregrini, "Radiation Losses in Substrate Integrated Waveguides: a Semi-Analytical Approach for a Quantitative Determination" in *IEEE MTT-S Int. Micro. Symp. Dig.*, Seattle, WA, June 2013, pp 1-3
- [39] M. Casaletti, G. Valerio, R. Sauleau, and M. Albani, "Rigorous losses evaluation in the numerical analysis of SIW structures," in *Antennas and Propagation (EuCAP), 2015 9th European Conference on*, 2015, pp. 1–2.
- [40] N. Ranjkesh and M. Shahabadi, "Reduction of dielectric losses in substrate integrated waveguide," *Electron. Let.*, vol. 42, no. 21, pp. 1230–1231, Oct. 2006.
- [41] A. Belenguer, H. Esteban, and V. E. Boria, "Novel empty substrate integrated waveguide for high-performance microwave integrated circuits," *IEEE Trans. Micro. Theory Techn.*, vol. 62, no. 4, pp. 832–839, Apr. 2014.
- [42] F. Parment, A. Ghiotto T. Vuong, J. Duchamp, and K. Wu, "Air-Filled Substrate Integrated Waveguide for Low-Loss and High Power-Handling Millimeter-Wave Substrate Integrated Circuits" *IEEE Trans. Micro. Theory Techn.*, vol. 63, no. 4, pp. 1228–1238, April 2015.
- [43] F. Parment, A. Ghiotto, T. P. Vuong, J. M. Duchamp, and K. Wu, "Double Dielectric Slab-Loaded Air-Filled SIW Phase Shifters for High-Performance Millimeter-Wave Integration," *IEEE Transactions on Microwave Theory and Techniques*, vol. 64, no. 9, pp. 2833–2842, Sep. 2016.
- [44] A. Ghiotto, F. Parment, T. P. Vuong, and K. Wu, "Multilayer-substrate integration technique of air-filled waveguide circuits," *2016 IEEE MTT-S International Conference on Numerical Electromagnetic and Multiphysics Modeling and Optimization (NEMO)*, 2016, pp. 1–3.
- [45] F. Parment, A. Ghiotto T. Vuong, J. Duchamp, and K. Wu, "Air-Filled Substrate Integrated Waveguide for Low-Loss and High Power-Handling Millimeter-Wave Substrate Integrated Circuits" *IEEE Trans. Microw. Theory Techn.*, vol. 63, no. 4, pp. 1228–1238, April 2015.
- [46] K. M. Ho, C. T. Chan, C. M. Soukoulis, R. Biswas, and M. Sigalas, "Photonic band gaps in three dimensions: New layer-by-layer periodic structures," *Solid State Communications*, vol. 89, no. 5, pp. 413–416, Feb. 1994.
- [47] R. C. Johnson and H. Jasik, *Antenna Engineering Handbook*, 2nd Revised edition. New York; London: McGraw-Hill Inc., US, 1984.
- [48] Z. L. Li and K. Wu, "A new approach to integrated horn antenna," in *Proc. Int. Symp. on Antenna Technology and Applied Electromagnetics*, Jul. 2004, pp. 535–538

- [49] M. Wong, A. R. Sebak, and T. A. Denidni, "A broadside substrate integrated horn antenna," *IEEE Antennas and Propagation Society International Symposium, 2008. AP-S 2008*, 2008, pp. 1–4.
- [50] H. Y. Tsao, D. H. Yang, J. C. Cheng, J. S. Fu, and W. P. Lin, "W-band SIW *H*-plane horn antenna development," *High Speed Intelligent Communication Forum (HSIC), 2012 4th International*, 2012, pp. 1–3.
- [51] K. Iigusa, K. Li, K. Sato, and H. Harada, "Gain Enhancement of *H*-Plane Sectoral Post-Wall Horn Antenna by Connecting Tapered Slots for Millimeter-Wave Communication," *IEEE Transactions on Antennas and Propagation*, vol. 60, no. 12, pp. 5548–5556, Dec. 2012.
- [52] K. Iigusa, J. Gao, K. Li, K. Sato, and H. Harada, "Improving gain of *H*-plane sectoral post-wall horn antenna for millimeter-wave communication by connecting tapered slots," in *Microwave Conference, 2009. APMC 2009. Asia Pacific*, 2009, pp. 1942–1945.
- [53] H. Wang, D. G. Fang, B. Zhang, and W. Q. Che, "Dielectric Loaded Substrate Integrated Waveguide (SIW) -Plane Horn Antennas," *IEEE Transactions on Antennas and Propagation*, vol. 58, no. 3, pp. 640–647, Mar. 2010.
- [54] M. Yousefbeiiki, A. A. Domenech, J. R. Mosig, and C. A. Fernandes, "Ku-band dielectric-loaded SIW horn for vertically-polarized multi-sector antennas," in *2012 6th European Conference on Antennas and Propagation (EUCAP)*, 2012, pp. 2367–2371.
- [55] Y. Cai, Z.-P. Qian, Y.-S. Zhang, J. Jin, and W.-Q. Cao, "Bandwidth Enhancement of SIW Horn Antenna Loaded With Air-Via Perforated Dielectric Slab," *IEEE Antennas and Wireless Propagation Letters*, vol. 13, pp. 571–574, 2014.
- [56] M. Esquiús-Morote, B. Fuchs, J. F. Zürcher, and J. R. Mosig, "A Printed Transition for Matching Improvement of SIW Horn Antennas," *IEEE Transactions on Antennas and Propagation*, vol. 61, no. 4, pp. 1923–1930, Apr. 2013.
- [57] M. E. Morote, B. Fuchs, and J. R. Mosig, "Printed transition for SIW horn antennas; Analytical model," in *2012 6th European Conference on Antennas and Propagation (EUCAP)*, 2012, pp. 1–4.
- [58] M. Esquiús-Morote, B. Fuchs, and J. R. Mosig, "A new type of printed Ku-band SIW horn antenna with enhanced performances," in *2012 International Symposium on Antennas and Propagation (ISAP)*, 2012, pp. 223–226.
- [59] M. Esquiús-Morote, B. Fuchs, J. F. Zürcher, and J. R. Mosig, "Novel Thin and Compact *H*-Plane SIW Horn Antenna," *IEEE Transactions on Antennas and Propagation*, vol. 61, no. 6, pp. 2911–2920, Jun. 2013.
- [60] L. Wang, X. Yin, S. Li, H. Zhao, L. Liu, and M. Zhang, "Phase Corrected Substrate Integrated Waveguide *H*-Plane Horn Antenna With Embedded Metal-Via Arrays," *IEEE Transactions on Antennas and Propagation*, vol. 62, no. 4, pp. 1854–1861, Apr. 2014.

- [61] A. R. Mallahzadeh and S. Esfandiarpour, "Wideband H -Plane Horn Antenna Based on Ridge Substrate Integrated Waveguide (RSIW)," *IEEE Antennas and Wireless Propagation Letters*, vol. 11, pp. 85–88, 2012.
- [62] A. F. Horn, J. W. Reynolds, and J. C. Rautio, "Conductor profile effects on the propagation constant of microstrip transmission lines," in *2010 IEEE MTT-S International Microwave Symposium*, 2010, pp. 868–871.
- [63] John Coonrod, "Insertion Loss Comparisons of Common High Frequency PCB Constructions," presented at the IPC APEX EXPO.
- [64] "Copper Foils for High Frequency Materials," from <https://www.rogerscorp.com>.
- [65] P. S. Kildal, and A. Kishk, "Em Modeling of Surfaces with Stop or Go Characteristics – Artificial Magnetic Conductors and Soft and Hard Surfaces," *ACES Journal*, vol. 18, no. 1, March 2003.
- [66] U. L. Rohde and D. P. Newkirk, *RF/Microwave Circuit Design for Wireless Applications*. New York, NY, USA: Wiley, 2000.
- [67] R. Gilmore and L. Besser, *Practical RF Circuit Design for Modern Wireless Systems*. Norwood, MA, USA: Artech House, 2003.
- [68] N. I. Dib, L. Katehi, *Theoretical characterization of coplanar waveguide transmission lines and discontinuities*, Radiation Lab, University of Michigan, 1992.
- [69] W. Heinrich, F. Schnieder, and T. Tischler, "Dispersion and radiation characteristics of conductor-backed CPW with finite ground width," in *Microwave Symposium Digest. 2000 IEEE MTT-S International, 2000*, vol. 3, pp. 1663–1666 vol.3.
- [70] C. Veyres and V. F. Hanna, "Extension of the application of conformal mapping techniques to coplanar lines with finite dimensions," *International Journal of Electronics*, vol. 48, no. 1, pp. 47–56, Jan. 1980.
- [71] K. C. Gupta, R. Garg, I. J. Bahl, and P. Bhartia, *Microstrip Lines and Slotlines*, 2nd ed. Artech House, Inc., 1996.
- [72] W. Hilberg, "From Approximations to Exact Relations for Characteristic Impedances," *IEEE Transactions on Microwave Theory and Techniques*, vol. 17, no. 5, pp. 259–265, May 1969.
- [73] Constantine A. Balanis, "*Antenna Theory: Analysis and Design*," John Wiley & Son
- [74] J. E. Rayas-Sanchez and V. Gutierrez-Ayala, "A general EM-based design procedure for single-layer substrate integrated waveguide interconnects with microstrip transitions," in *Microwave Symposium Digest, 2008 IEEE MTT-S International, 2008*, pp. 983–986.
- [75] K. Sakakibara, J. Hirokawa, M. Ando, and N. Goto, "A linearly-polarized slotted waveguide array using reflection-canceling slot pairs," *IEICE Trans. Commun.*, vol. E-77-B, no. 4, 1994.
- [76] Asem Al-Zoubi, Ahmed Kishk, and Allen Glisson, "A Linear Rectangular Dielectric Resonator Antenna Array Fed by Dielectric Image Guide with Low cross polarization,"

- IEEE Transactions on Antennas and Propagations*, Vol. 58, no. 4, pp. 697 - 705, March 2010.
- [77] P. S. Kildal, "Definition of artificially soft and hard surfaces for electromagnetic waves," *Electronics Letters*, vol. 24, no. 3, pp. 168–170, Feb. 1988.
- [78] E. Lier, "A dielectric hybrid mode antenna feed: A simple alternative to the corrugated horn," *IEEE Transactions on Antennas and Propagation*, vol. 34, no. 1, pp. 21–29, Jan. 1986.
- [79] P. S. Kildal, E. Lier, and J. A. Aas, "Artificially soft and hard surfaces in electromagnetics and their application," in *Antennas and Propagation Society International Symposium, 1988. AP-S. Digest*, 1988, pp. 832–835 vol.2.
- [80] E. Lier and P.-S. Kildal, "Soft and hard horn antennas," *IEEE Transactions on Antennas and Propagation*, vol. 36, no. 8, pp. 1152–1157, Aug. 1988.
- [81] B. Thomas, "Design of corrugated conical horns," *IEEE Transactions on Antennas and Propagation*, vol. 26, no. 2, pp. 367–372, Mar. 1978.
- [82] E. Lier and P-S. Kildal, "A novel type of high-gain horn antennas," in *Proc. ZCAP Conf.*, York, England, March 30-April 2, 1987, pp. 43 1-433
- [83] E. Lier, "Analysis of soft and hard strip-loaded horns using a circular cylindrical model," *IEEE Transactions on Antennas and Propagation*, vol. 38, no. 6, pp. 783–793, Jun. 1990.
- [84] S. P. Skobelev and P. S. Kildal, "Analysis of a hard strip-loaded conical horn by the method of generalized scattering matrices," *IEEE Transactions on Antennas and Propagation*, vol. 51, no. 10, pp. 2918–2925, Oct. 2003.
- [85] P. S. Kildal, "Gaussian beam model for aperture-controlled and flare angle-controlled corrugated horn antennas," *Antennas and Propagation IEE Proceedings H - Microwaves*, vol. 135, no. 4, pp. 237–240, Aug. 1988.
- [86] E. Lier and A. Kishk, "A new class of dielectric-loaded hybrid-mode horn antennas with selective gain: design and analysis by single mode model and method of moments," *IEEE Transactions on Antennas and Propagation*, vol. 53, no. 1, pp. 125–138, Jan. 2005.
- [87] E. Lier, "Review of Soft and Hard Horn Antennas, Including Metamaterial-Based Hybrid-Mode Horns," *IEEE Antennas and Propagation Magazine*, vol. 52, no. 2, pp. 31–39, Apr. 2010.
- [88] Li, G. DeJean, M. M. Tentzeris, J. Papapolymerou, and J. Laskar, "Radiation-pattern improvement of patch antennas on a large-size substrate using a compact soft-surface structure and its realization on LTCC multilayer technology," *IEEE Transactions on Antennas and Propagation*, vol. 53, no. 1, pp. 200–208, Jan. 2005.
- [89] Z. Ying and P. S. Kildal, "Improvements of dipole, helix, spiral, microstrip patch and aperture antennas with ground planes by using corrugated soft surfaces," *Antennas and Propagation IEE Proceedings - Microwaves*, vol. 143, no. 3, pp. 244–248, Jun. 1996.

- [90] E. Rajo-Iglesias, Ó. Quevedo-Teruel, and L. Inclin-Sanchez, “Planar Soft Surfaces and Their Application to Mutual Coupling Reduction,” *IEEE Transactions on Antennas and Propagation*, vol. 57, no. 12, pp. 3852–3859, Dec. 2009.
- [91] R. Chair, A. A. Kishk, and K. F. Lee, “Experimental investigation for wideband perforated dielectric resonator antenna,” *Electronics Letters*, vol. 42, no. 3, pp. 137–139, Feb. 2006.
- [92] L. Brillouin, *Wave Propagation in Periodic Structures: Electric Filters and Crystal Lattices*. Courier Corporation, 2003.